AN OBSERVATIONAL INVESTIGATION OF TRANSITORY TURBULENCE IN THE ATMOSPHERIC BOUNDARY LAYER

by

Derek D. Jensen

A dissertation submitted to the faculty of
The University of Utah
in partial fulfillment of the requirements for the degree of

Doctor of Philosophy

Department of Mechanical Engineering

The University of Utah

December 2016

The University of Utah Graduate School

STATEMENT OF DISSERTATION APPROVAL

The dissertation of **Derek D. Jensen**

has been approved by the following supervisory committee members:

Eric R. Pardyjak	, Chair	**3 Oct. 2016** Date Approved
Daniel F. Nadeau	, Member	**3 Oct. 2016** Date Approved
James R. Stoll II	, Member	**3 Oct. 2016** Date Approved
Marc Calaf	, Member	**3 Oct. 2016** Date Approved
Sebastian Wilhelm Hoch	, Member	**3 Oct. 2016** Date Approved

and by **Timothy A. Ameel** , Chair/Dean of

the Department/College/School of **Mechanical Engineering**

and by David B. Kieda, Dean of The Graduate School.

ABSTRACT

Within the atmospheric boundary layer (ABL), atmospheric fluid flow is in a constant state of transition in both time and space. Under calm conditions through the mid-daytime hours and over quasi-uniform terrain, the temporal and spatial evolution of the atmosphere is gradual. The structure and governing equations are well understood, allowing for numerical models to accurately forecast the evolution of the ABL. Under nocturnal conditions, the atmospheric processes are more complicated, yet numerical models still perform reasonably well. When changes in the state of the atmosphere occur abruptly, whether in time or space, the fidelity of most numerical weather models diminishes appreciably. This occurs because many of the simplifying assumptions intrinsic in most numerical models are no longer valid. The objective of this dissertation is to use observational data collected within such transitions to gain more insight into the mechanisms responsible for the evolution of the rapidly evolving ABL.

First, near-surface turbulence data are used to study countergradient heat fluxes that occur through the evening transition. The countergradient heat flux may be produced by the sign change of the sensible heat flux preceding the sign change of the local temperature gradient and vice versa. The phenomenon is studied by considering the budget equations of both temperature and sensible heat flux. The behaviour of the countergradient heat flux is governed by the surface and subsurface characteristics. The duration of the countergradient flux may be prognosed by considering a ratio of terms in the heat flux budget equation evaluated during the mid- to late afternoon.

Next, data collected over an arid shallow slope (2–4°) are used to study the structure and onset of katabatic flow through the evening transition. The katabatic onset, jet velocity and jet height all show a large degree of interdiurnal variability. The slope-aligned budgets of momentum and potential temperature are used to define

time scales that describe the evolution of the katabatic flow. A simple katabatic model utilizing surface energy budget modeling is developed and used to model the interdiurnal katabatic variance. Finally, uni- and multivariate statistical analysis are used to diagnose the influence of specific external variables. Valley wind speed, turbulence structure, soil moisture and shadow front speed are all found to influence the katabatic dynamics to varying degrees.

Finally, the morning and evening transitions over coastal, tropical terrain are investigated using data collected during a multiyear, wind-resource assessment. The wind distribution is found to be bimodal and governed by synoptic scales, with onshore and offshore flow regimes. The diurnal sea/land breeze is observed to be present, but its influence is secondary to the large-scale forcing. When the flow is directed onshore, the inland wind speed deficit is significant and the wind speed falls off at ≈ 5 % km^{-1}. For the onshore flow regime, the site nearest the coast observes nearly constant temperature and nearly uniform mechanical generation of turbulence. The mechanical generation of turbulence is found to be the dominant term in the budget of turbulence kinetic energy and is able to sustain high levels of turbulence kinetic energy throughout the diurnal cycle. Finally, multiresolution flux decomposition is used to study turbulence evolution over different time scales.

For Kristen, Mom, Dad and The Arctic Phantom

CONTENTS

LIST OF FIGURES

LIST OF TABLES

AUTHOR LIST

The following authors contributed to Chapter 2: Daniel F. Nadeau, Sebastian W. Hoch and Eric R. Pardyjak.

The following authors contributed to Chapter 3: Daniel F. Nadeau, Sebastian W. Hoch and Eric R. Pardyjak.

The following authors contributed to Chapter 4: Daniel F. Nadeau, Timothy A. Price, Jacob Kingston and Eric R. Pardyjak.

ACKNOWLEDGMENTS

I would like to sincerely thank my academic advisor, Eric Pardyjak. Your tireless work ethic, curiosity, concern for others and sincerity have been an example to me. You have been an amazing mentor and I have thoroughly enjoyed our academic and not-so academic discussions. I would also like to thank my co-advisor, Daniel Nadeau. It has been an absolute pleasure working with you for the last several years. Your attention to detail and sincere concern for my well-being helped me to become a much more capable researcher. Your and Eric's brilliance and friendship were invaluable assets throughout my PhD. I would also like to thank my other committee members, Rob Stoll, Sebastian Hoch and Marc Calaf.

No field project is performed alone. Starting with MATERHORN, Michael Carston, Paul Broderick and Dragan Zajic all went above and beyond to make the project a success. Thank you to Daniel Alexander, my close friend and colleague, for helping me to write my first ever CRBasic program. Tim Price and I likely score on the all-time list for most towers installed and instrumented as a PhD duo. During the Belize project, our eyes in the field, Hank Bauman was always willing to head out to the towers, Facebook Messenger in-hand, ready to diagnose why those darn towers weren't communicating. Meanwhile, Patrick Flores was back at the Paradise Shrimp Farm office tracking down our latest shipment of parts. Each of their efforts contributed to making this dissertation possible.

Next, I would like to thank the amazing people that I have had the pleasure of interacting with over the past five years. I have enjoyed learning and spending time with all of my colleagues in the University of Utah Environmental Fluid Dynamics Laboratory. Whether we were having a discussion in Building 60, skiing, mountain biking or playing ping pong, I learned a tremendous amount from all of you and had a great time doing it. I am grateful to my family for their support throughout my

PhD. Dad, thank you for making so many sacrifices over the years to make sure your kids had access to the best education. Mom, thank you for always being ready to pick up the phone and go to battle for me to make sure I wasn't being mistreated. Carl, thank you for blazing the academic trail in the Jensen family and for all of your advice over the years. Kristen, thank you for putting up with me and my never-ending cycle of procrastination followed by panic. Your love, advice and constant support have made my PhD possible.

Finally, I would like to thank the Office of Naval Research and Jacob Kingston of Washakie Renewable Energy for their generous funding.

CHAPTER 1

INTRODUCTION

Turbulent length scales in the atmosphere span six orders of magnitude, from the smallest dissipative scales, $\mathcal{O}$(mm), to length scales on the order of kilometers. While, due to computational limitations, most weather and climate models are run at resolutions coarser than 1 km, it is the small-scale, near-surface generation and decay of turbulence that is responsible for the transport of heat, momentum and scalars to and from the atmosphere. In order to bridge the scale gap, weather and climate models utilize turbulence parameterizations to model the influence of the unresolved scales. Though much progress has been made, such turbulence parameterizations incorporate limiting assumptions that are frequently invalid, particularly with regard to temporally and spatially transitory turbulence. The focus of this dissertation is to use observational data collected during periods where such parameterizations are expected to perform poorly. The objective is to contribute to our understanding of the atmosphere in such conditions and to provide a basis for more robust turbulence parameterizations under transitory conditions.

1.1 The Atmospheric Boundary Layer

The atmospheric boundary layer (ABL) is defined as the lowest portion of the troposphere that is directly influenced by the Earth's surface on times scales of 1 hour or less. The idealized, diurnal evolution of the ABL over land is illustrated in Fig. 1.1. During convective daytime conditions over land, the depth of the ABL may extend up to several km, while under calm nocturnal conditions, the ABL may be as shallow as several tens of m (Stull, 1988). Within the ABL, the surface layer (SL) extends from a height of approximately three times higher than the local roughness elements up to $\approx$ 10 % of the ABL height. Within the SL, shear production of turbulence is

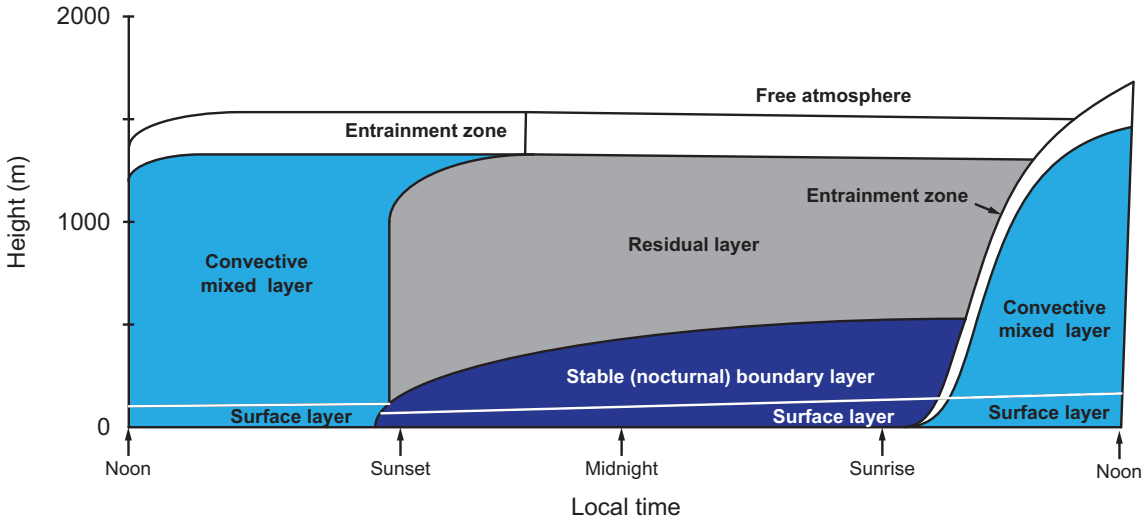

Figure 1.1: Schematic of the atmospheric boundary layer adapted from Stull (1988) by D.F. Nadeau.

more important than buoyant production, the wind speed and temperature profiles are logarithmic, and fluxes are invariant with height (Stull, 1988).

The definition of the SL is highly idealized and rarely holds in reality. Nonetheless, most near-surface turbulent parameterizations utilized in weather and climate models are only valid within a well-defined SL. Furthermore, it is requisite that the turbulent statistics be horizontally homogeneous (insensitive to horizontal translations) and stationary (insensitive to temporal translations). In reality, the above conditions are rarely met (e.g. Cheng et al., 2005; Katul et al., 2004; Nadeau et al., 2011; Figueroa Espinoza and Salles, 2014). The Earth's surface, particularly in urban and coastal regions, is strongly heterogeneous with abrupt transitions in roughness elements and in the surface energy balance. Sloping and undulating terrain further complicate the structure of the ABL and SL, where horizontal temperature gradients lead to local circulations (Whiteman, 2000; Mahrt et al., 2001; Zardi and Whiteman, 2013). With the exception of the peak daylight hours under clear skies and no synoptic forcing, the structure of the ABL and SL is inherently transitory in nature.

During the morning and evening transitions, the turbulence is nonstationary, the SL is poorly defined, mixing eddies are small and develop/decay anisotropically, and heterogeneity effects become more important than under daytime conditions. Downslope flows transition to upslope and vice-versa. The mechanisms driving the flow become much smaller and more diverse, making accurate and simple parameterizations of the turbulence difficult to develop (e.g. Grant, 1997; Sorbjan, 1997; Acevedo and Fitzjarrald, 2001, 2003; Lothon and Lenschow, 2011; Nadeau et al., 2011; Lothon et al., 2014). The case of fluid advecting across abruptly changing surface conditions, such as the sea-land and rural-urban transitions or abrupt changes in land cover, is similar. The fluid properties become strongly stratified as the new surface is felt first at lower layers and then propagates upwards at variable rates, depending on properties such as atmospheric stability, roughness features of the two surface types and variable surface energy balances (Garratt, 1990; Bou-Zeid, 2004; Savelyev and Taylor, 2005; Chamorro and Porté-Agel, 2009). The implications of abrupt changes in land cover is of sufficient complexity and importance that the National Research Council has listed it as one of the grand challenges in the environmental sciences (EARTH, 2001).

1.2 Monin-Obukhov Similarity Theory

Of particular interest to numerical weather and climate models is the transport of heat, momentum and moisture between the ABL and the Earth's surface. The most common method for obtaining the turbulent exchanges (fluxes) in the diabatic atmosphere from mean variables is Monin-Obukhov similarity theory (MOST, Monin and Obukhov, 1954; Beljaars and Holtslag, 1991).

Within the SL, the vertical fluxes of heat, momentum and moisture are typically assumed to be proportional to their local negative gradient by the simple relation

$$\overline{w'\chi'} = -K_\chi \frac{\partial \overline{\chi}}{\partial z}, \tag{1.1}$$

where χ is the variable of interest, w is the vertical velocity, K_χ is the exchange coefficient for χ, the overbar indicates time averaging, the prime indicates turbulent perturbations from the mean ($\chi' = \chi - \overline{\chi}$) and z is the vertical coordinate. The kinematic flux of χ, $\overline{w'\chi'}$, is costly to directly measure and unavailable in most models; however, $\partial\overline{\chi}/\partial z$ is relatively easy to measure and a model variable. MOST provides a framework where K_χ can be calculated, thus allowing for an estimation of the turbulent flux.

The basis for MOST is dimensional analysis. The hypothesis states that for *stationary*, *homogeneous* flow, within a well-defined surface layer where fluxes do not vary with height by more than 10% and rotational forces are negligible, the fluid dynamics are a function of only four independent variables: the height above the surface z; friction velocity $u_* = \overline{u'w'}^{0.5}$, where u is the horizontal wind speed; kinematic sensible heat flux $\overline{w'T'}$, where T is the air temperature; and the buoyancy variable $g/\overline{T}$, where g is the gravitational acceleration.

Following the Buckingham Pi theorem for dimensional analysis, only one dimensionless number can be obtained, which is typically taken as the nondimensional length scale

$$\zeta = \frac{z}{L}, \tag{1.2}$$

where L is the Obukhov length defined as

$$L = \frac{-u_*^3 T}{\kappa g \overline{w'T'}} \tag{1.3}$$

and $\kappa \approx 0.4$ is the von Kármán constant. The exchange coefficient K_χ is computed from the non-dimensional gradient of χ by the relation:

$$K_\chi = \kappa z \chi_* / \phi_\chi(\zeta), \tag{1.4}$$

where $\chi_* = \overline{w'\chi'}/u_*$ is the scaling variable for χ and ϕ_χ is the non-dimensional gradient of χ which is typically determined empirically (e.g. Businger et al., 1971; Foken, 2006) and a function of only ζ. The non-dimensional gradient of χ can then be integrated to estimate the vertical profile of χ,

$$\frac{\chi - \chi_0}{\chi_*} = \frac{1}{\kappa}\Big[\ln\Big(\frac{z}{z_{0,\chi}}\Big) - \psi_\chi\Big(\frac{z}{L}\Big)\Big], \tag{1.5}$$

where ψ_χ is the vertical integral of ϕ_χ, χ_0 is the value of χ evaluated at $z_{0,\chi}$ and $z_{0,\chi}$ is the roughness length specific to the variable. For wind speed, $u_0 = 0$ and $z_{0,u}$ is on the order of $0.15h_0$, where h_0 is the mean height of the surrounding roughness elements.

Despite the limiting assumptions, MOST has been shown to hold over a variety of conditions. For moderately unstable conditions over flat homogeneous terrain, MOST has been shown to accurately estimate fluxes within the SL (Dyer and Hicks, 1970; Businger et al., 1971; Dyer, 1974; Högström, 1996; Foken, 2006). Under nocturnal conditions, the application of MOST is more nuanced. Effects due to increased advection, weak and intermittent turbulence and strong stability limit its application. Nonetheless, researchers have shown many instances where the application of MOST is still valid for moderately stable conditions (Monin and Yaglom, 1971; Nieuwstadt, 1984; Mahrt et al., 1998; Mahrt, 1999). Additionally, some aspects of MOST have also been useful for scaling over sloping, rough terrain (Franceschi et al., 2009; Nadeau et al., 2013), above the SL (Mahrt, 1999; Nieuwstadt, 1984), over urban terrain (Wood et al., 2010) and for some transitory conditions (Cheng et al., 2005). However, for the nonidealized conditions, modifications are typically necessary and it is difficult to accurately predict fluxes and vertical structures.

1.3 Dissertation Organization and Scientific Questions

The overarching goal of this dissertation is to identify transitory periods in the ABL where existing turbulence parameterizations and numerical models are expected to perform poorly, and then use observational data to improve our understanding of

transitory turbulence through such periods. Ch. 2–4 examine different aspects of transitory turbulence in the ABL. In Ch. 2 and 3, flow over complex terrain and the evening transition is examined. In Ch. 4, both the morning and evening transition are studied using data collected over coastal, complex terrain. Figure 1.2 illustrates each of the studies. The study objectives and structure as follows.

First, In Ch. 2, countergradient heat fluxes that occur during the evening transition are examined. Data collected over broadly different sites during the Mountain Terrain Atmospheric Modeling and Observations Program (MATERHORN, Fernando et al., 2015) are used to study the phenomenon. The objective of the work is, first, to determine the frequency and duration of the countergradient heat flux, including site and height dependence; second, identify the mechanisms responsible for the countergradient flux; and finally, predict the countergradient duration. The study first examines the performance of MOST through the evening transition and then quantifies the countergradient behaviour as a function of height at both experimental sites. The budgets of potential temperature and sensible heat flux are examined to determine the mechanisms responsible for the phenomenon and finally, a ratio of budget terms evaluated through the afternoon is found to accurately prognose the countergradient duration. The study has been published in *Boundary-Layer Meteorology* with the citation: Jensen, D. D., D. F. Nadeau, S.W. Hoch, and E. R. Pardyjak, 2016: Observations of near-surface heat-flux and temperature profiles through the early evening transition over contrasting surfaces. *Boundary-Layer Meteorol.*, **159**, 567587.

Ch. 3 examines the influence of external variables on the development and structure of katabatic flow through the evening transition. Again, data collected during the field portion of the MATERHORN program are used. The experimental site is a highly instrumented shallow, east-facing slope including a transect of five turbulence towers. The objective is to understand both the mean timing and structure of the katabatic flow as well as to understand the dependence of the interdiurnal variance observed in the flow on external, meteorological variables. The dependence is examined with both mechanisitic and statistical models. The benefits of each approach are discussed. The study has been accepted to *Quarterly Journal of the*

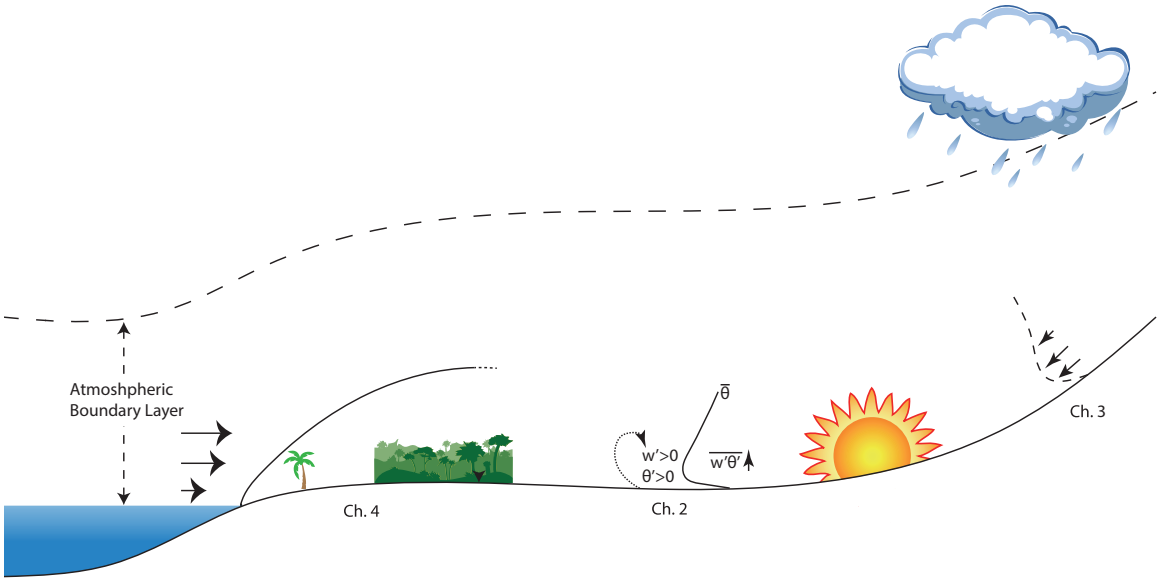

Figure 1.2: Schematic of the studies in Ch. 2–4. Ch. 2 examines near-surface countergradient heat fluxes during the evening transition, Ch. 3 examines the influence of external variables on katabatic flow dynamics (note the rain cloud indicates external influences such as soil moisture, cloud cover, etc.), Ch. 4 examines the morning and evening transition periods over coastal, tropical terrain.

Royal Meteorological Society pending minor revisions, under the title: *The evolution and sensitivity of katabatic flow dynamics to external influences through the evening transition.*

In Ch. 4, the morning and evening transitions are studied over a coastal, tropical shrimp farm in Belize, Central America. Instrumentation consists of three tall masts ($\geq$ 50 m) that create an approximate inland transect spanning from the coast to approximately 4 km inland. The data were collected as part of a wind resource analysis, and data collection lasted for more than two years. The study capitalizes on the strengths of the dataset by examining the morning and evening transitions from a climatological perspective. First, the climatology and prevailing wind regimes of the region are discussed followed by a detailed treatment of the morning and evening transition periods. Both composite time series of turbulence variables and multiresolution flux decomposition are used to examine the erosion of the stable boundary later through the morning transition and the decay of turbulence through the evening transition. The study will be submitted to *Journal of Applied Meteorology and Climatology*

Finally, Ch. 5 discusses the main findings of the work and identifies future work, and a discussion of the selection of appropriate flux averaging times is found in the appendix.

1.4 References

Acevedo, O. C. and D. R. Fitzjarrald, 2001: The early evening surface-layer transition: Temporal and spatial variability. *J. Atmos. Sci.*, **58**, 2650–2667.

Acevedo, O. C. and D. R. Fitzjarrald, 2003: In the core of the night – Effects of intermittent mixing on a horizontally heterogeneous surface. *Boundary-Layer Meteorol.*, **106**, 1–33.

Beljaars, A. C. M. and A. A. M. Holtslag, 1991: Flux parameterization over land surfaces for atmospheric models. *J. Appl. Meteorol.*, **30**, 327–341.

Bou-Zeid, E., 2004: Large-eddy simulation of neutral atmospheric boundary layer flow over heterogeneous surfaces: Blending height and effective surface roughness. *Water Resour. Res.*, **40 (2)**, 1–18.

Businger, J. A., J. C. Wyngaard, Y. Izumi, and E. F. Bradley, 1971: Flux-profile relationships in the atmospheric surface layer. *J. Atmos. Sci.*, **28**, 181–189.

Chamorro, L. P. and F. Porté-Agel, 2009: Velocity and surface shear stress distributions behind a rough-to-smooth surface transition: A simple new model. *Boundary-Layer Meteorol.*, **130**, 29–41.

Cheng, Y., M. B. Parlange, and W. Brutsaert, 2005: Pathology of Monin-Obukhov similarity in the stable boundary layer. *J. Geophys. Res.*, **110**, 1–10.

Dyer, A. J., 1974: A review of flux-profile relationships. *Boundary-Layer Meteorol.*, **7**, 363–372.

Dyer, A. J. and B. B. Hicks, 1970: Flux-gradient relationships in the constant flux layer. *Q. J. R. Meteorol. Soc.*, **96**, 715–721.

EARTH, G. C. I., 2001: Grand challenges in earth and environmental sciences: Science, stewardship, and service for the twenty-first century. *GSA today*, 41.

Fernando, H., et al., 2015: The materhorn: Unraveling the intricacies of mountain weather. *Bulletin of the American Meteorological Society*, **96 (11)**, 1945–1967.

Figueroa Espinoza, B. and P. Salles, 2014: Local MoninObukhov similarity in heterogeneous terrain. *Atmos. Sci. Lett.*, **306**, 299–306.

Foken, T., 2006: 50 Years of the Monin-Obukhov Similarity Theory. *Boundary-Layer Meteorol.*, **119**, 431–447.

Franceschi, M. D., D. Zardi, M. Tagliazucca, and F. Tampieri, 2009: Analysis of second-order moments in surface layer turbulence in an Alpine valley. *Q. J. R. Meteorol. Soc.*, **1765**, 1750–1765.

Garratt, J. R., 1990: The internal boundary layer - A review. *Boundary-Layer Meteorol.*, **50**, 171–203.

Grant, A. L. M., 1997: An observational study of the evening transition boundary-layer. *Q. J. R. Meteorol. Soc.*, **123**, 657–677.

Högström, U., 1996: Review of some basic characteristics of the atmospheric surface layer. *Boundary-Layer Meteorol.*, **78**, 215–246.

Katul, G., D. Cava, D. Poggi, J. Albertson, and L. Mahrt, 2004: Stationarity, homogeneity, and ergodicity in canopy turbulence. *Handbook of micrometeorology*, Springer, 161–180.

Lothon, M. and D. H. Lenschow, 2011: Studying the afternoon transition of the planetary boundary layer. *Eos, Trans. Am. Geophys. Union*, **91**, 253–254.

Lothon, M., et al., 2014: The BLLAST field experiment: Boundary-Layer Late Afternoon and Sunset Turbulence. *Atmos. Chem. Phys.*, **14**, 10 931–10 960.

Mahrt, L., 1999: Stratified atmospheric boundary layers. *Boundary-Layer Meteorol.*, **90**, 375–396.

Mahrt, L., J. Sun, W. Blumen, T. Delany, and S. Oncley, 1998: Nocturnal boundary-layer regimes. *Boundary-Layer Meteorol.*, **88**, 255–278.

Mahrt, L., D. Vickers, and R. Nakamura, 2001: Shallow drainage flows. *Boundary-Layer Meteorol.*, **101**, 243–260.

Monin, A. S. and A. M. Obukhov, 1954: Basic laws of turbulent mixing in the surface layer of the atmosphere. *Contrib. Geophys. Inst. Acad. Sci.*, **24**, 163–187.

Monin, A. S. and A. Yaglom, 1971: *Statistical Fluid Mechanics - vol 1: Mechanics of Turbulence*. The MIT Press, 769 pp.

Nadeau, D. F., E. R. Pardyjak, C. W. Higgins, H. J. S. Fernando, and M. B. Parlange, 2011: A simple model for the afternoon and early evening decay of convective turbulence over different land surfaces. *Boundary-Layer Meteorol.*, **141**, 301–324.

Nadeau, D. F., E. R. Pardyjak, C. W. Higgins, and M. B. Parlange, 2013: Similarity scaling over a steep alpine slope. *Boundary-Layer Meteorol.*, **147**, 401–419.

Nieuwstadt, F. T. M., 1984: The turbulent structure of the stable, nocturnal boundary layer. *J. Atmos. Sci.*, **41**, 2202–2216.

Savelyev, S. a. and P. a. Taylor, 2005: Internal boundary layers: I. Height formulae for neutral and diabatic flows. *Boundary-Layer Meteorol.*, **115**, 1–25.

Sorbjan, Z., 1997: Decay of convective turbulence revisited. *Boundary-Layer Meteorol.*, **82**, 503–517.

Stull, R., 1988: *An Introduction to Boundary Layer Meteorology*. Springer Science, 666 pp.

Whiteman, C. D., 2000: *Mountain Meteorology: Fundamentals and Applications*. 1st ed., Oxford University Press, Oxford, 355 pp.

Wood, C. R., et al., 2010: Turbulent Flow at 190 m Height Above London During 2006-2008: A Climatology and the Applicability of Similarity Theory. *Boundary-Layer Meteorol.*, **137**, 77–96.

Zardi, D. and C. D. Whiteman, 2013: Diurnal mountain wind systems. *Mountain weather research and forecasting: recent progress and current challenges*, Springer Science and Business Media, 219–260.

CHAPTER 2

OBSERVATIONS OF NEAR-SURFACE HEAT-FLUX AND TEMPERATURE PROFILES THROUGH THE EARLY EVENING TRANSITION OVER CONTRASTING SURFACES

Jensen, Derek D., Daniel F. Nadeau, Sebastian W. Hoch, and Eric R. Pardyjak. "Observations of near-surface heat-flux and temperature profiles through the early evening transition over contrasting surfaces." *Boundary-Layer Meteorology* 159, no. 3 (2016): 567-587. With kind permission of Springer

2.1 Introduction

For idealized, fair-weather daytime conditions, a well-mixed convective layer exists above the unstable surface layer. Under nocturnal conditions, a stable boundary layer, characterized by weak and possibly intermittent turbulence and strong stratification, develops near the surface (Stull, 1988). While the structure of the daytime and nocturnal boundary layers are fairly well understood, less is known about the transition from daytime to nocturnal conditions. Adopting the terminology of Nadeau et al. (2011), this transition is broken into two portions. The afternoon transition begins when the surface sensible heat flux begins to decrease from its midday maximum followed by the evening transition when the surface sensible heat flux becomes negative. The early evening transition (EET) is the 1 to 2 h period before and after the heat-flux reversal. Many researchers have noted that a greater understanding of the EET is important for model development and better forecasts for wind energy production, convective storm initiation, and pollutant dispersion (e.g. Cole and Fernando, 1998;

Sorbjan, 1997; Acevedo and Fitzjarrald, 2003; Edwards et al., 2006; Angevine, 2007; Lothon and Lenschow, 2011; Nadeau et al., 2011; Lothon et al., 2014).

During the EET, the flow is inherently unsteady. Turbulence is non-stationary, fluxes are small and the driving forces evolve on short time scales. Furthermore, during this transition period, a well-defined surface layer and mixed layer do not exist (Grant, 1997). Turbulent mixing decreases while horizontal heterogeneity and differential cooling become increasingly important. Also, the traditional daytime scaling laws for the convective boundary layer (Deardorff, 1970) and surface layer (Monin and Obukhov, 1954) are no longer well-defined. Finally, after the surface sensible heat flux has reversed in sign, entrainment fluxes continue to feed energy into the boundary layer for some time (Nieuwstadt and Brost, 1986; Sorbjan, 1997; Grimsdell and Angevine, 2002; Pino et al., 2006). These factors combined with a relative lack of observations make a thorough analysis of the EET difficult.

Until recently, the EET was rarely studied. Starting with the work of Nieuwstadt and Brost (1986), a number of large-eddy simulation studies have been conducted on the decay of the convective boundary layer. Over the years, the studies have increased in complexity and allowed for more realistic forcing time scales and boundary conditions (e.g. Sorbjan, 1997; Acevedo and Fitzjarrald, 2001; Brown et al., 2002; Edwards et al., 2006; Kumar et al., 2006, 2010; Pino et al., 2006; Goulart et al., 2010; Rizza et al., 2013; Taylor et al., 2014). Additionally, a number of laboratory experiments have been conducted to study transitional stability (Comte-Bellot and Corrsin, 1971; Cole and Fernando, 1998; Kang et al., 2003). To a lesser extent, observations are used to study the decay of convective turbulence. Acevedo and Fitzjarrald (2001) utilized a dense sensor network to study temporal and spatial variability in mean variables through the EET, Nadeau et al. (2011) used field data to successfully model the decay of turbulent kinetic energy in a convective surface layer over contrasting surface types. The Boundary Layer Late Afternoon and Sunset Turbulence (BLLAST) campaign was specifically designed to experimentally study the EET (Lothon et al., 2014). Perhaps the only field study to specifically study near-surface, countergradient behaviour during the EET is the BLLAST study conducted by Blay-Carreras et al. (2014). Their work found a persistent time lag between the time of the buoyancy

flux reversal and local gradient reversal. Typical lag times persisted between 30 and 80 min. They concluded that the phenomenon might be site-dependent and that further studies were necessary. In light of this and the fact that nearly all numerical weather models assume that surface fluxes are directed down-gradient (Mahrt, 1999), this topic merits further study.

Here, we extend the work of Blay-Carreras et al. (2014) by contrasting two experimental sites that strongly differ from the one used in their study. First, the Playa site is located on a large alkaline playa with no vegetation, shallow water table and high subsurface soil moisture. Second, the Sagebrush site is located in a desert steppe area with limited soil moisture. We use turbulence data collected in the atmospheric surface layer to study the evolution of near-surface heat-flux and temperature-gradient profiles through the EET. The goal is to provide additional clarity regarding the evolution of near-surface heat flux and temperature gradients through the EET.

2.2 Methods

Data for the analysis were collected during the Mountain Terrain Atmospheric Modeling and Observations Program. The principal objective of MATERHORN is to improve weather predictability in regions of complex terrain. The experimental portion of the program consisted of two field campaigns that took place at the United States Army Facility, Dugway Proving Ground in Utah's West Desert, USA. The first field campaign ran from 26 September – 7 November 2012 and focused on quiescent (thermally-driven) conditions with minimal synoptic forcing. The second campaign ran from 1 May – 6 June 2013 with an emphasis on synoptically-forced weather. Through both campaigns, continuous observations of the near-surface wind speed and temperature profiles and the surface energy balance were made. During 24-h intensive observation periods (IOPs), additional instrumentation such as tethered and free-flying balloons, aircraft, lidar, hot-wire anemometers, and infrared cameras were deployed. Both campaigns consisted of ten IOPs. Full details and objectives of the MATERHORN program are found in Fernando et al. (2015).

2.2.1 Experimental Sites

For the current study, we consider two highly instrumented sites, with their mean soil and surface characteristics reported in Table 2.1. First, the Playa site is located on a large desert playa (part of the dry remnants of the ancient Lake Bonneville) with no vegetation and an elevation of 1296 m above sea level (40°8'5.9" N, 113°27'7.8" W). The playa surface and soil characteristics are nearly homogeneous following rain events with a gradual increase in spatial heterogeneity until another rain event occurs. At depths beyond 60 mm, the playa soil is nearly always saturated. Due to high soil salinity at the Playa site, the volumetric water content (VWC) measurements were made by hand. The autumn measurements were conducted only three times at a single location, while the spring measurements were conducted each IOP at 20 locations. Thus, a meaningful comparison between the autumn and spring VWC values is impossible. Based on the surface albedo (a), thermal conductivity (k) and volumetric heat capacity of the soil, defined as $C = \rho c$ where ρ is density and c is specific heat capacity, it is evident that the mean soil moisture at the Playa was higher during the autumn campaign than the spring. Under quiescent, convective conditions, the surface wind speed and direction are influenced by weak pressure gradients aloft. During nighttime, a nocturnal southerly flow with a jet-like structure develops frequently.

The Sagebrush site is located approximately 25 km to the east of the Playa site (40°7'16.9" N, 113°7'44.7" W) at an elevation of 1316 m above sea level. The two sites are separated by Granite Peak, a small mountain with a maximum elevation of 850 m above the valley floor (Fig. 2.1). The vegetation is predominately Greasewood (Emrick and Hill, 1999) approximately 1 m in height. The VWC is much lower at the Sagebrush site, allowing for a smaller heat capacity and thermal inertia (TI). Contrary to the Playa site, the mean soil moisture at Sagebrush is higher during the spring campaign. Additionally, the leaf area index (LAI) increases and subsequently decreases the mean surface albedo. Under quiescent daytime conditions surface wind speed and direction are influenced by weak pressure gradients aloft. During the night, the development of a south-easterly drainage flow frequently influences the Sagebrush site.

Table 2.1: Soil and surface characteristics at the Playa and Sagebrush sites. VWC is the volumetric water content, a is the surface albedo, k is the measured 50 mm thermal conductivity of the soil, C is the 50 mm volumetric heat capacity computed from $C = k/\alpha$ where α is the measured thermal diffusivity of the soil, $TI \equiv \sqrt{kC}$ is the 50 mm thermal inertia of the soil, LAI is the leaf area index estimated from NASA's MODIS tool, and z_0 is the surface roughness.

	Site	VWC	a	k (W m^{-1} K^{-1})	C (MJ K^{-1} m^{-3})	TI (J m^{-2} K^{-1} s$^{-1/2}$)	LAI	z_0 (mm)
Autumn	Playa	0.30	0.31	0.90	2.2	1400	0	0.61
	Sagebrush	0.09	0.27	0.49	1.3	800	0.17	93
Spring	Playa	0.38	0.33	0.77	2.1	1270	0	0.11
	Sagebrush	0.13	0.24	0.72	1.7	1100	0.24	140

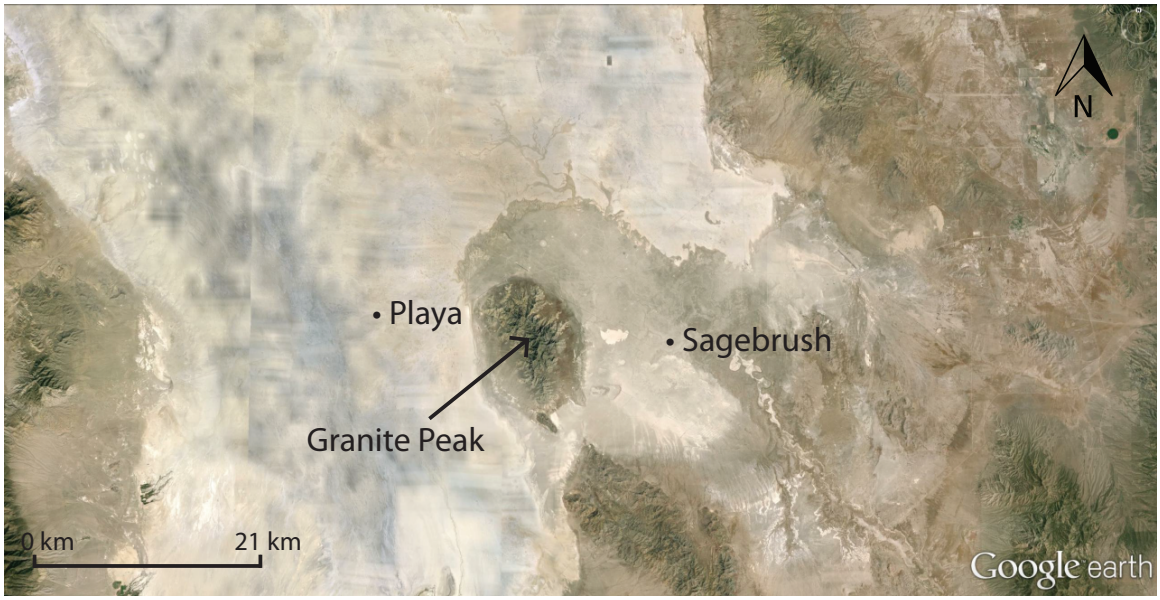

Figure 2.1: Map of the two experimental sites in Utah's West Desert (Google Earth, 2013).

The aerodynamic roughness length (z_0) was estimated for both sites by considering wind speed profiles under near-neutral conditions. A least squares, linear regression of the wind speed (U) as a function of $\ln(z)$ was computed for each 5-min period. Regressions with R^2 values below 0.99 were removed. Finally z_0 was estimated as the median value of z_0 from all profiles considered, and as expected, $z_{0,Playa} \leq z_{0,Sagebrush}$, with $z_{0,Sagebrush}$ increasing in the spring, due to increased vegetation.

2.2.2 Instrumentation

At both sites, sonic anemometers and type-E thermocouples were used to obtain turbulence data at multiple levels. The thermocouples used were 0.0127 mm in diameter with no radiation shield or active ventilation as the solar loading is expected to be negligible (Erell et al., 2005). The thermocouples were placed near the centre of the sonic anemometer path for a spatial separation on the order of several tens of mm. The Playa site had six measurement levels between 0.5 and 26 m, while the Sagebrush site had five measurement levels between 0.5 and 20 m. Due to occasional instrumentation problems at the 26-m Playa tower, and to create consistency between sites, we only examine the five measurement levels between 0.5 and 20 m. Fast response, open-path, infrared gas analyzers were positioned at a height of 10 m at Playa and Sagebrush, with a spatial distance of 60 mm from the sonic anemometer measurement volume, to determine the latent heat flux (H_L). Near both tower bases, high density arrays of type-E thermocouples, 0.0254 mm in diameter, were installed at heights between 10 mm and 3.2 m above the ground, with a higher number placed very near the surface. At Playa, 20 sensors were sampled at 20 Hz, and at Sagebrush 25 sensors were sampled at 1 Hz. The underlying surface temperature was also measured with an infrared radiometer installed at a height of approximately 0.25 m, with an assumed emissivity of 0.97 (Malek, 1997).

At both sites, approximately 50 m to the west of the main towers, soil property sensors were buried at a depth of 50 mm to directly measure the thermal conductivity and diffusivity (α) of the soil. Finally, near the soil sensors, the four components of the radiation balance were measured on a sawhorse-type structure at 2 m above the surface. Site and sensor information is given in Table 2.2 and Fig. 2.2.

Table 2.2: Instrumentation deployed at the Playa and Sagebrush sites. Accuracy given as reported by the manufacturer. Tower locations refer to Fig. 2.2. u, v, and w are the streamwise, spanwise and vertical velocity components, respectively; T_s is the sonic derived temperature; H_2O is the mass density of H_2O ; P is atmospheric pressure; T is air temperature; RH is relative humidity; T_0 is surface temperature; k is the soil thermal conductivity and α is the soil thermal diffusivity. The FW1 and SI-111 sensors were installed near the tower base at both sites. At Playa (Sagebrush), 20 (25) FW1s were installed at heights between 0.01 and 3.2 m and sampled at 20 (1) Hz, with the SI-111 positioned at 0.25 m above ground. The FW1 measurement heights are given in the caption of Fig. 2.9.

Instrument name	Variables measured	Accuracy	Sampling frequency (Hz)	Manufacturer	Tower Locations
CSAT3	u, v	±0.08 m s^{-1}	20	Campbell Sci.	A, B, C, D,
	w	±0.04 m s^{-1}			E, F, J
	T_s	n/a			
EC150	H_2O	n/a	20	Campbell Sci.	D, J
	P	±15 hPa			
RMY8100	u, v, w	±0.05 m s^{-1}	20	R.M. Young	G, H, I, K
	T_s	± 2°C			
FW05	T	±0.07°C	20	Campbell Sci.	All
HMP45	T	±0.25°C	1	Vaisala	All
	RH	± 2%			
FW1	T	±0.07°C	20, 1	Campbell Sci.	n/a
SI-111	T_0	±0.2°C	1	Apogee Inst.	n/a
TP01	k	±5%	1/600	Hukseflux	n/a
	α	±20%			

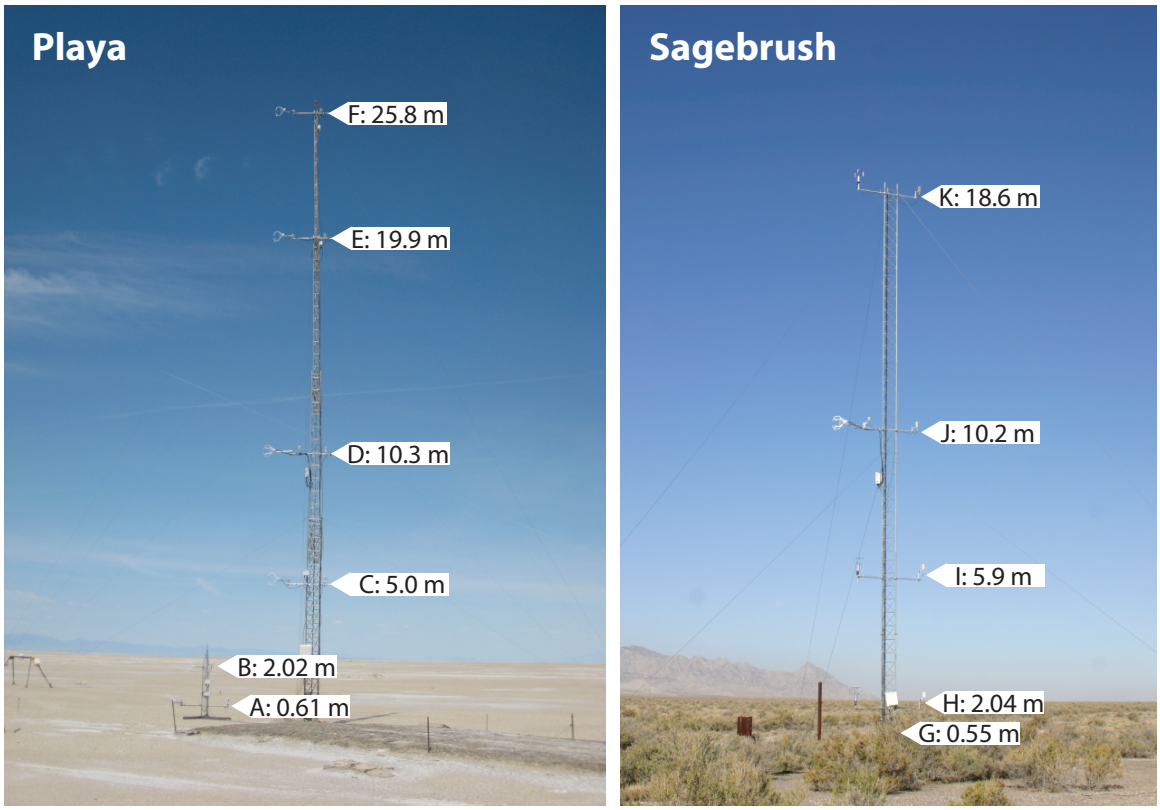

Figure 2.2: Photographs looking north-west toward the Playa tower (left) and Sagebrush tower (right) with instrument heights imposed on the image. The northern portion of Granite Peak is visible behind the Sagebrush tower. Height labels refer to Table 2.2. For simplicity, tower heights are referred to as 0.5, 2, 5, 10, 20, and 26 m throughout this study. The 0.5 and 2 m Playa instrumentation is mounted on a smaller tower to the west of the main tower to minimize flow distortion. At both sites, the radiation balance and soil property measurements were made approximately 50 m to the west of the main tower.

2.2.3 Data Analysis

Data analysis used the Utah Turbulence in Environmental Studies processing and analysis code (UTESpac). Despiking and quality control were performed following Vickers and Mahrt (1997), planar fitting was applied following Wilczak et al. (2001) and density corrections were applied to the latent heat flux following Webb et al. (1980). Based on Blay-Carreras et al. (2014) and ogive tests (Aubinet et al., 2012), 5-min averaging periods and linear detrending were chosen chosen as the best combination to isolate the turbulent motions from the rapidly evolving mean state through the EET. Finally, due to small spatial separations in the eddy-covariance systems, no spectral corrections were applied (Aubinet et al., 2012).

Heat fluxes and potential temperatures were computed from the fine-wire thermocouples, with all vertical gradients computed using finite difference techniques. A forward difference is used for the lowest level (Error $O(dz)$), a backward difference for the highest level (Error $O(dz)$), and a three-point difference (Error $O(dz^2)$), utilizing the analytical derivative of a Lagrangian interpolating polynomial, for the middle levels (Chapra and Canale, 2010). All temporal gradients were computed using central differencing (Error $O(dt^2)$).

2.2.4 Transition Analysis

In order to study flux and gradient time evolution through the EET, a relative time τ is defined as $\tau = t - t_{Rn=0}$ where t is time and $t_{Rn=0}$ is the first time period where the net radiation has become negative. The relative time of the sensible heat flux sign change (H) is given by τ_{flux}, and the relative time of the potential temperature gradient ($\partial\overline{\theta}/\partial z$) sign change is given by τ_{grad}. The identification method of τ_{grad} and τ_{flux} differ one from the other: τ_{grad} is defined as the timestep following the last period where the gradient was negative. This is because the gradients at 5 m and above are small with slightly positive and negative values before stabilization occurs. Once the stabilization has occurred, the gradients typically become persistently positive. In contrast, τ_{flux} is identified by the first time period where the heat flux becomes negative. This is because the strongly positive fluxes transition into weakly negative fluxes with occasional positive values. The reversals were identified computationally

with careful examination to ensure that the reversal is accurately captured. The mean gradient and heat-flux behaviour is addressed in Sect. 2.3.3 and 2.3.4, respectively.

Next, we define a time lag, $t_{\text{lag}} = \tau_H - \tau_{\text{grad}}$ to quantify delays between the gradient and flux sign changes. Therefore, $t_{\text{lag}} > 0$ indicates that the gradient sign change precedes the flux sign change (Fig. 2.5a, quadrant I) and $t_{\text{lag}} < 0$ indicates the flux sign change precedes the gradient sign change (Fig. 2.5b, quadrant III), which is the behaviour observed by Blay-Carreras et al. (2014).

Finally, we filter the data to eliminate transitions with incomplete data availability, excessive cloud cover, mean wind speeds at 5 m > 10 m s^{-1}, and non–monotonically decreasing temperatures through the late afternoon transition. We do this to limit our study to idealized, quiescent days with little synoptic forcing in an effort to focus on microscale phenomena. We are left with eight transition periods at Playa and 13 at Sagebrush.

2.3 Results and Discussion

2.3.1 Surface Fluxes

Figure 2.3 shows the ensemble averaged net radiation (R_n), sensible heat flux (H), latent heat flux (H_L), potential temperature (θ), and wind speed for all days considered at both sites. The mean daytime R_n is appreciably higher at the Sagebrush site, consistent with the lower albedo, while the nighttime R_n magnitude is appreciably higher at the Playa site, consistent with the higher volumetric heat capacity and surface temperature. The formation and decay of sensible heat flux at Playa is much more gradual than that of Sagebrush. At the Sagebrush site, H reaches a maximum values of $\approx$ 135 W m^{-2} that persists for several hours and then rapidly decays as R_n decreases. At the Playa site, H briefly reaches a maximum value of approximately 85 W m^{-2} and almost immediately begins to slowly decay. At Playa, the positive heat flux persists for approximately 1 h after net-radiative sunset while the flux reversal at Sagebrush typically occurs around 30 min after net-radiative sunset. Similar to the heat flux, the 10-m potential temperature at Playa increases and decreases more gradually than at Sagebrush, with a smaller diurnal amplitude.

Given the arid nature of the region, the magnitude of H_L is quite small at

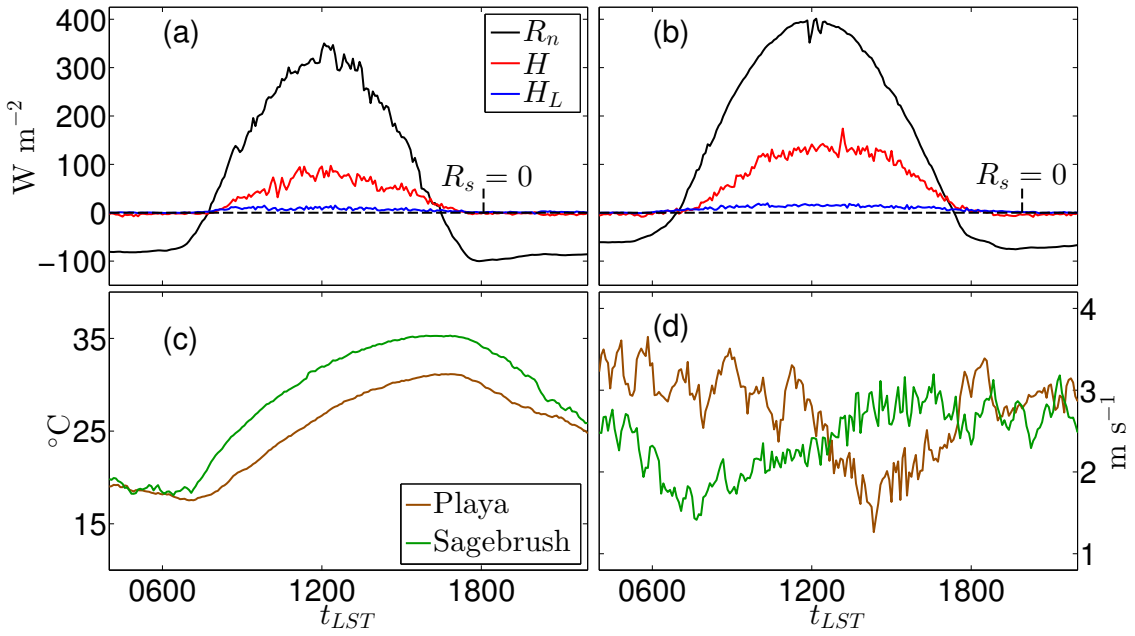

Figure 2.3: Time series of the mean, 10-m variables for all days considered at both sites. Panel (**a**) and (**b**) give the sensible (H) and latent (H_L) heat fluxes and net radiation (R_n) at the Playa and Sagebrush sites, respectively. R_s = 0 indicates local solar sunset. Panel (**c**) gives the mean potential temperature and panel (**d**) gives the mean wind speed.

both sites, H_L reaches a maximum of approximately 12 and 19 W m^{-2} at Playa and Sagebrush, respectively, which yields a mean daytime Bowen ratio, defined as $\beta \equiv H/H_L$, of approximately 7 at both sites. Given the much higher soil moisture at Playa, this result is likely due to two factors. First, the thin, smooth crust on the playa surface is effective at preventing moisture transport; second, plant transpiration likely plays an important important role in the moisture budget at the Sagebrush site. Finally, though the sites are geographically close to one another, the smooth surface at the Playa site allows for a slightly higher mean wind speed.

2.3.2 Monin-Obukhov Scaling and Countergradient behaviour

To better understand the scaling of fluxes and temperature profiles during the EET, the heat fluxes are displayed in the traditional Monin-Obukhov similarity theory (MOST) framework. Figure 2.4 shows the non-dimensional temperature gradient (ϕ_h) as a function of stability (ζ), where ϕ_h and ζ are defined as

$$\phi_h(\zeta) = \frac{\kappa z}{\theta_*}\frac{\partial\overline{\theta}}{\partial z}, \tag{2.1}$$

and

$$\zeta = \frac{z - d_0}{L}, \tag{2.2}$$

where $\kappa = 0.4$ is the von Kármán constant, $\overline{\theta}$ is the mean potential temperature of air in the surface layer, $\theta_* = -\overline{w'\theta'_0}/u_*$ is the scaling temperature, z is the height above the surface, d_0 is the displacement height, which is found to be zero at both sites, and L is the Obukhov length,

$$L = \frac{-u_*^3}{\kappa\frac{g}{\overline{\theta}}\overline{w'\theta'}}, \tag{2.3}$$

where u_* is the friction velocity, g is acceleration due to gravity and $\overline{w'\theta'}$ is the kinematic heat flux.

For unstable conditions ($-2.5 < \zeta \lesssim -0.2$), both sites scale quite well and ϕ_h is only slightly larger than the empirical formulation recommended by Dyer and Hicks (1970), indicated by the dashed black line. For stable conditions ($0.2 \lesssim \zeta < 1$), the scatter is

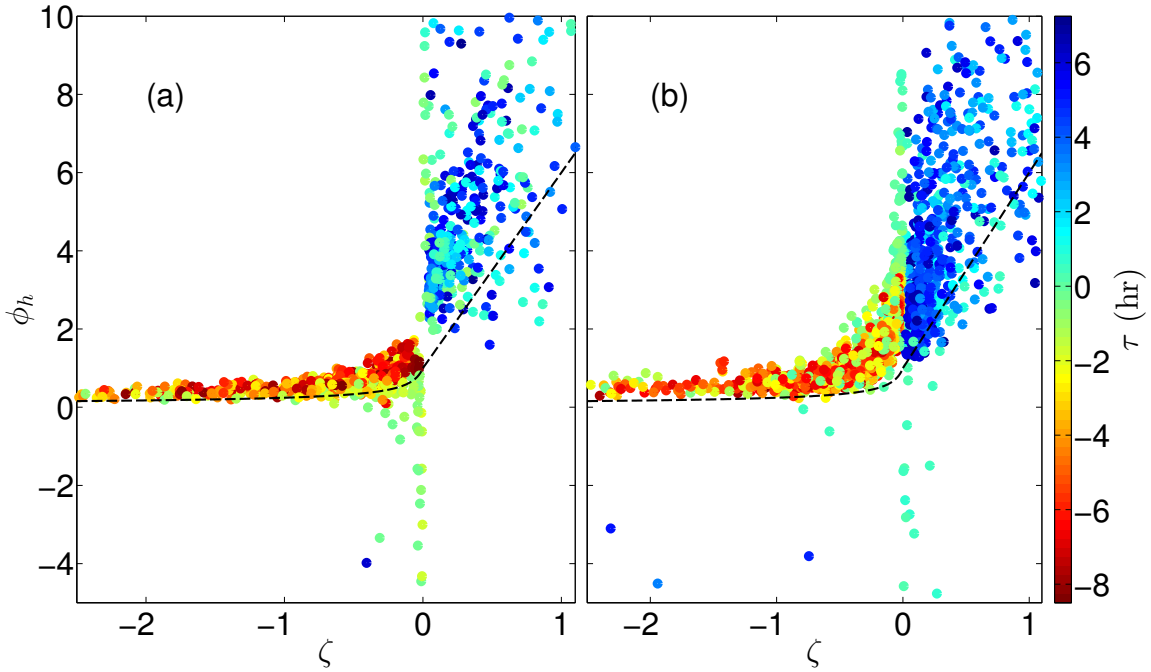

Figure 2.4: The non-dimensional temperature gradient (ϕ_h) as a function of stability (ζ) at 2 m for Playa **(a)** and Sagebrush **(b)**. The markers are experimental data from 8.5 hours before net-radiative sunset ($\tau = 0$) to 7 hours after. The dashed line is the empirical form of ϕ_h recommended by Dyer and Hicks (1970).

large at both sites. A trend is visible but it is less well defined and the slope is much steeper than the Dyer formulation, suggesting that an alternate formulation of ϕ_h may be more appropriate. Under near-neutral conditions ($-0.1 \lesssim \zeta \lesssim 0.1$), an asymptotic behaviour with large positive and negative values is observed. This behaviour is due to H being in the denominator of ϕ_h via θ_*. The negative values of ϕ_h indicate that the local heat flux is countergradient. Theoretically, this regime corresponds to the classical neutrally stratified surface layer where θ_* is no longer a relevant scaling variable. However, neutral scaling does not apply during this transition either. Non-local effects become important and the local temperature gradient is a poor indicator of the local heat flux.

To explore the countergradient phenomena, a quadrant analysis of the kinematic sensible heat flux ($\overline{w'\theta'}$) and potential temperature gradient ($\partial\overline{\theta}/\partial z$) at 2 m is used (Fig. 2.5). Physically, quadrant II corresponds to typical afternoon conditions where the heat flux is positive and $\partial\overline{\theta}/\partial z$ is negative. The data in quadrant II at Playa are relatively linear with a steep slope and minimal spread, indicating acceptable flux-gradient behaviour. At Sagebrush, the flux reduces substantially while the unstable temperature gradient remains relatively large, indicating that the turbulent diffusivity, defined as $K_h = \overline{w'\theta'}/(\partial\overline{\theta}/\partial z)$, is relatively small and non-linear. Quadrant IV corresponds to typical nighttime conditions where the heat flux is negative and the gradient is positive. At the Sagebrush site, a maximum negative heat flux occurs for $\partial\overline{\theta}/\partial z \approx 0.2$ K m^{-1} indicating a maximization of mixing efficiency as the surface layer stabilizes (Caughey et al., 1979). There is no clear evidence of this at the Playa site. Quadrants I and III correspond to countergradient heat fluxes. In quadrant I, H remains positive after the gradient has changed sign ($t_{\text{lag}} > 0$). This behaviour describes all countergradient periods at the Playa site. In quadrant III, the gradient remains negative after H has changed sign ($t_{\text{lag}} < 0$). This behaviour describes nearly all transitional, countergradient situations at the 2-m Sagebrush site (note that some quadrant I behaviour occurs at Sagebrush long after transition) and is consistent with the observations of Blay-Carreras et al. (2014).

Table 2.3 contains τ_{grad} , τ_{flux} and t_{lag} for all days considered at 2 m for the Playa and Sagebrush sites. τ_{grad} shows some similarity between sites with much higher

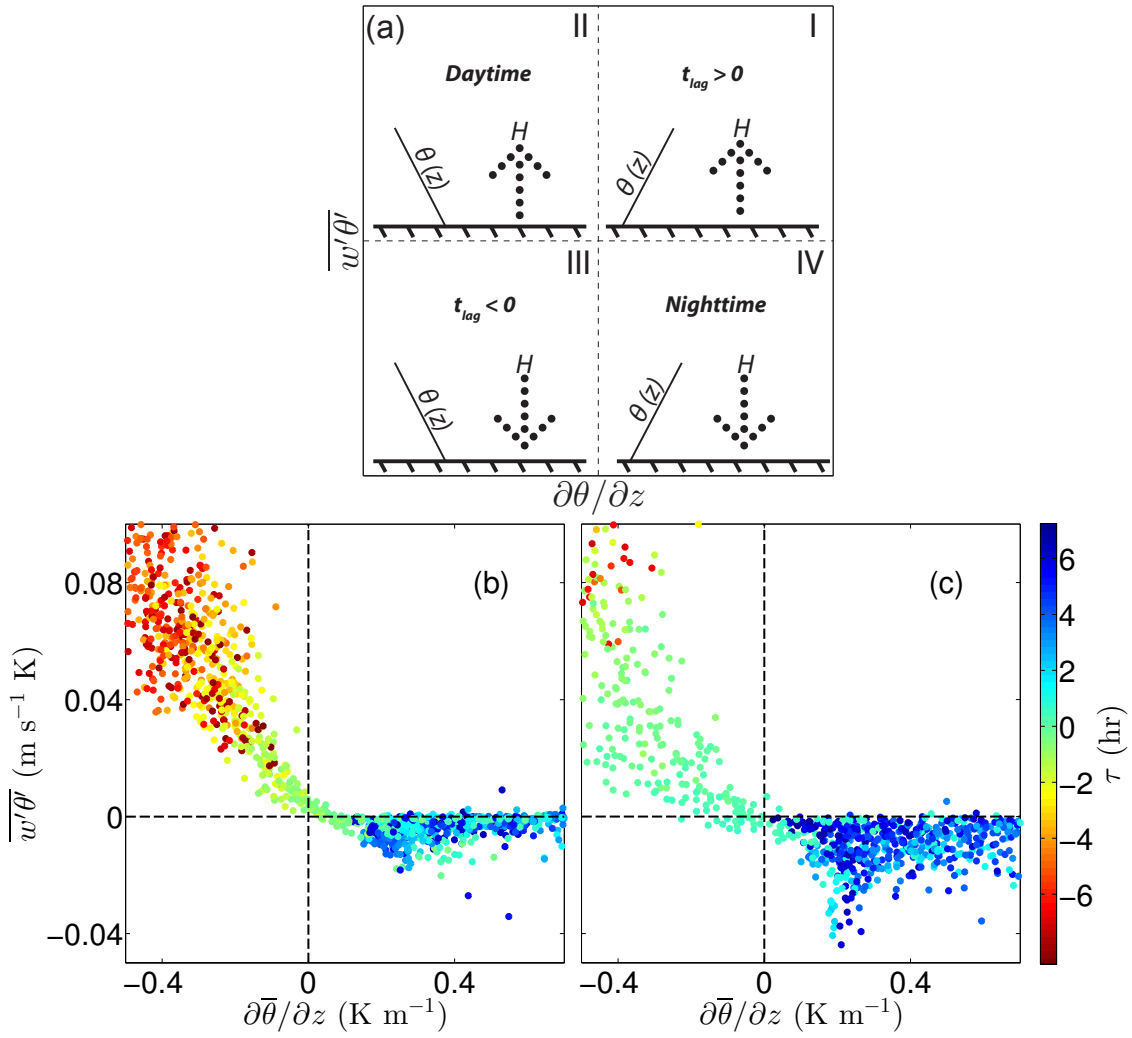

Figure 2.5: Quadrant analysis of the kinematic sensible heat flux and potential temperature gradient. **(a)** shows the qualitative behaviour of each quadrant. Quadrants II and IV correspond to daytime and nighttime conditions, respectively. Quadrants I and III correspond to countergradient heat fluxes. In quadrant I the gradient reversal precedes the flux reversal; in quadrant III the flux reversal precedes the gradient reversal. The 2-m Playa site **(b)** is dominated by $t_{\text{lag}} > 0$ while the 2-m Sagebrush site **(c)** is dominated by $t_{\text{lag}} < 0$. Data is coloured by τ.

Table 2.3: Countergradient timing variables for 2 m at Playa and Sagebrush. $t_{R_n=0}$ is the local net-radiative sunset in local standard time (LST), τ_{grad} is the time of the local temperature gradient reversal relative to $t_{R_n=0}$, τ_{flux} is the relative time of the heat-flux reversal, and t_{lag} is the countergradient duration computed by subtracting τ_{grad} from τ_{flux}.

Site	Date	$t_{R_n=0}$ (LST)	τ_{grad} (min)	τ_{flux} (min)	t_{lag} (min)
Playa	7 Oct. 2012	1640	45	65	20
	14 Oct. 2012	1650	35	40	5
	15 Oct. 2012	1650	10	20	10
	17 Oct. 2012	1630	60	70	10
	18 Oct. 2012	1630	55	70	15
	19 Oct. 2012	1635	10	20	10
	20 Oct. 2012	1640	–25	0	25
	21 Oct. 2012	1600	45	70	25
Sagebrush	28 Sept. 2012	1710	40	30	–10
	29 Sept. 2012	1715	20	15	–5
	1 Oct. 2012	1700	45	30	–15
	2 Oct. 2012	1710	25	20	–5
	3 Oct. 2012	1710	30	20	–10
	4 Oct. 2012	1710	30	25	–5
	6 Oct. 2012	1700	45	35	–10
	7 Oct. 2012	1700	45	40	–5
	8 Oct. 2012	1700	25	35	10
	9 Oct. 2012	1645	20	15	–5
	12 May 2013	1835	20	15	–5
	24 May 2013	1835	30	20	–10
	30 May 2013	1850	20	20	0

variability at Playa. τ_{flux} is typically smaller for Sagebrush with higher variability at Playa. $|t_{\text{lag}}|$ is typically between 5 and 20 minutes for both sites with negative values associated with Sagebrush (quadrant III from Fig. 2.5) and positive values associated with Playa (quadrant I). The large variability in τ_{grad} and τ_{flux} with the accompanying small variability in t_{lag} at Playa indicates that the countergradient behaviour is fairly consistent. That is, regardless of when transition occurs, if τ_{grad} is known, τ_{flux} may be inferred and vice versa. This is also the case at Sagebrush, but in addition, τ_{flux}, τ_{grad} and t_{lag} may be estimated from only $t_{Rn=0}$.

Box plots are used to illustrate τ_{grad}, τ_{flux} and t_{lag} for all heights across all days considered (Fig. 2.6 - 2.8). First considering τ_{grad}, the variability is smaller at Sagebrush, but the median time of gradient reversal is approximately constant between sites for a given height. Furthermore, gradient reversal is a top-down phenomena with a slope of $\frac{\partial \tau_{\text{grad}}}{\partial z} \approx -4$ min m^{-1} at both sites, indicating that within the context of this study, gradient reversal is top-down and site independent.

Next, τ_{flux} (Fig. 2.7) is considered. Again, the variability at Playa is quite large but invariant across all heights. When individual days are considered (not shown), the flux reversal occurs nearly simultaneously at all heights. Thus, the variability in Fig 2.7a is predominantly due to the relatively weak correlation between the net-radiative sunset and flux reversal. The median flux reversal at Playa typically occurs 30 - 40 minutes later than at Sagebrush. Unlike the gradient reversal, the flux reversal is strongly site-dependent but independent of height. This is counter to what Caughey and Kaimal (1977) reported, where they observed the flux to change sign from top to bottom over a larger height range than measured in the present experiment. Given this information, we hypothesize that $t_{\text{lag}}(z)$ may be approximated near the surface with only t_{lag} at a single reference height by

$$t_{\text{lag}}(z) \approx -\frac{\partial \tau_{\text{grad}}}{\partial z}(z - z_{\text{ref}}) - t_{\text{lag}}(z_{\text{ref}}). \tag{2.4}$$

Figure 2.8 shows $t_{\text{lag}}(z)$ with the solid line representing Eq. 2.4, calculated from τ_{grad} and τ_{flux} at 2 m. The uncertainty in t_{lag} grows with height at both sites, due to the weak temperature gradients aloft, but Eq. 2.4 generally captures the trend and

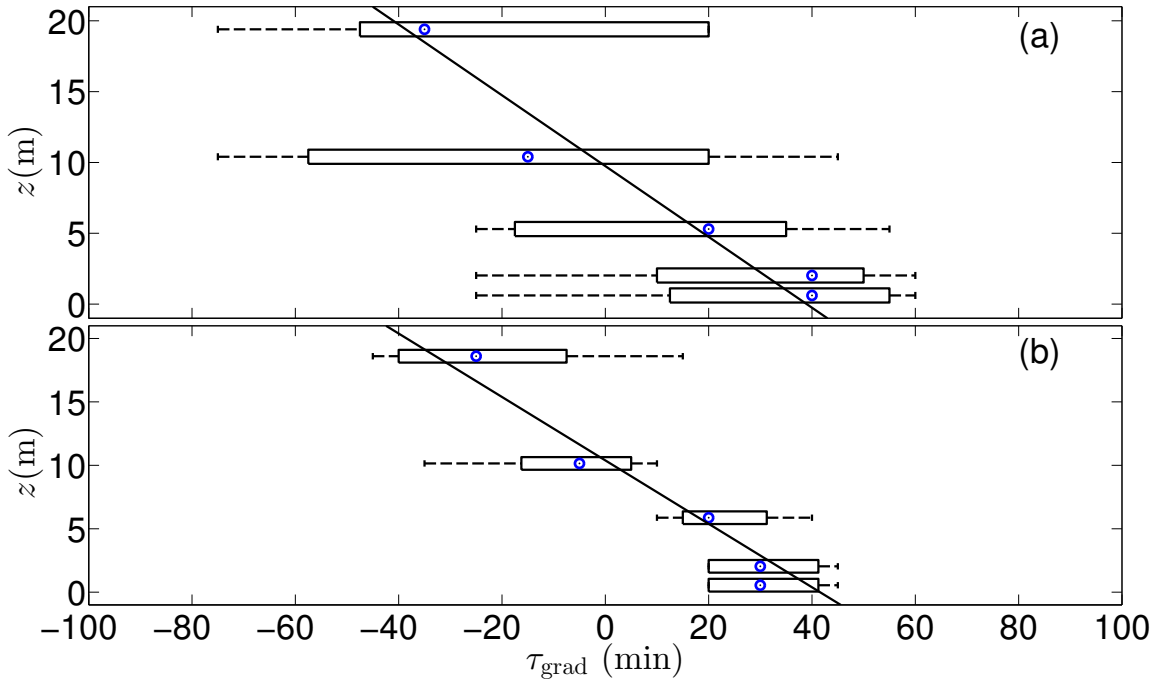

Figure 2.6: Box plots of gradient reversal time τ_{grad} for Playa **(a)** and Sagebrush **(b)**. The target within the box represents the median value, the left and right walls of the box represent the first and third quartiles and the whiskers represent data that fall within 1.5 times the interquartile range (IQR) of the nearest box wall. Any markers beyond the whiskers represent individual outliers. The solid line is a linear fit of the median values with a slope of $\frac{\partial \tau_{\text{grad}}}{\partial z} \approx -4$ min m^{-1}.

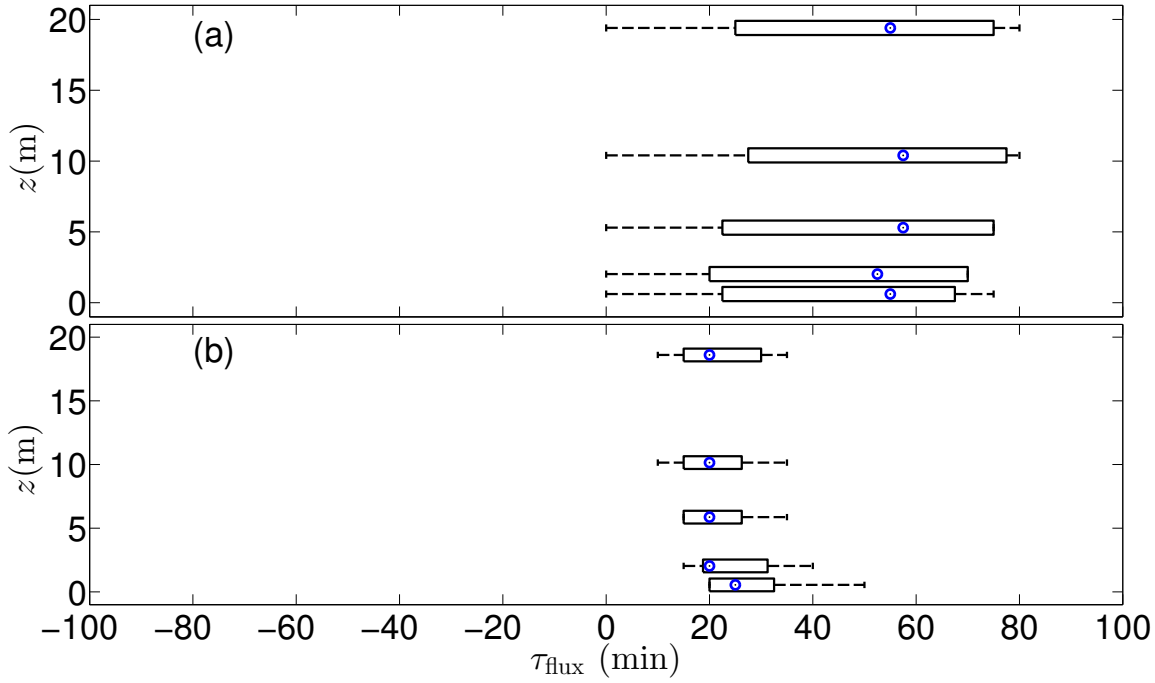

Figure 2.7: Box plots of the heat-flux reversal time τ_{flux} for Playa **(a)** and Sagebrush **(b)**. The target within the box represents the median value, the left and right walls of the box represent the first and third quartiles and the whiskers represent data that fall within 1.5 times the interquartile range (IQR) of the nearest box wall. Any markers beyond the whiskers represent individual outliers. The flux reversal occurs nearly simultaneously at both sites, with the Playa reversal occurring later than that of Sagebrush.

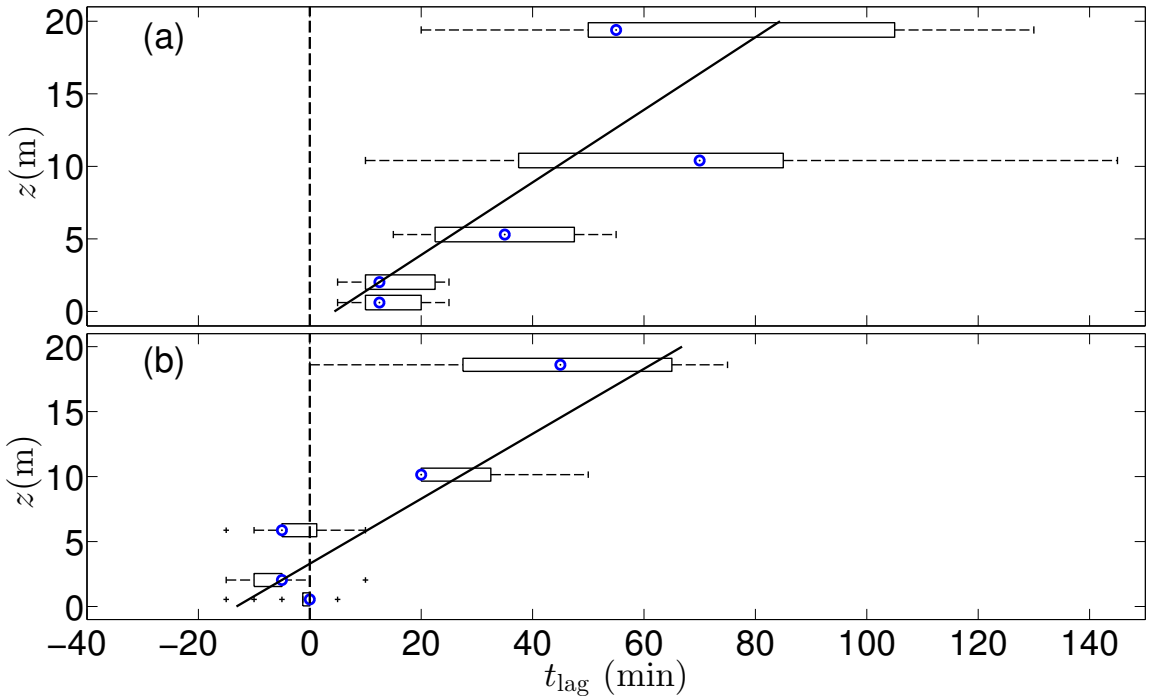

Figure 2.8: Box plots of t_{lag} for Playa **(a)** and Sagebrush **(b)**. The solid line is calculated from Eq. 2.4 with the 2-m values of τ_{flux} and τ_{grad}. The 0.5-m $|t_{\mathrm{lag}}|$ at Sagebrush is smaller than expected and is likely influenced by sheltering effects.

typically falls within the interquartile range (IQR) of the box plots (marked by the limits of the the box).

To illustrate and explain the countergradient behaviour, a schematic and observed potential temperature profiles are shown in Fig. 2.9. At Playa (**a**), the schematic illustrates the temperature structure just before the heat-flux reversal. There is a near-surface lifted temperature minimum (LTM) with an unstable layer very near the surface generating an upward heat flux that propagates through the weakly stable layer above, creating a countergradient flux in the shaded portion of the figure (see Blay-Carreras et al., 2015, and references therein for a discussion of LTM). The potential temperature profiles (**c**) at τ = 30 (cyan curve) and 45 (light-blue curve) min show the phenomenon. At Sagebrush, the schematic illustrates the temperature structure just after the heat-flux reversal. An LTM exists between 5 and 10 m; however, the LTM is local and the surface is significantly cooler than the air above. A weakly unstable 'residual' layer exists just above the surface and extends to the height of the local LTM (between 5 and 10 m). Cool air is mixed upward from the surface, creating a countergradient flux throughout the weakly unstable layer. The temperature profiles (**d**) at τ = 15 (green curve) and 30 (cyan curve) min show this behaviour. At Sagebrush, just before the heat-flux reversal (not shown in the schematic), the surface temperature is warmer than the surrounding air and the LTM between 5 and 10 m is the minimum temperature measured on the tower. The countergradient layer starts at the LTM height and extends to the top of the tower (similar to the Playa schematic described above). The temperature profile at τ = 0 (yellow curve) min shows this behaviour.

2.3.3 Temperature Gradient Evolution and Flux Divergence

To clarify the differing countergradient behaviours at the Playa and Sagebrush sites, the temperature gradient and heat-flux evolution are considered independently. First, the temperature gradient evolution is discussed followed by the heat-flux evolution in Sect. 2.3.4.

The mean temperature gradient evolution is shown for both sites in Fig. 2.10. As expected, the gradients are much stronger at Sagebrush both before and after

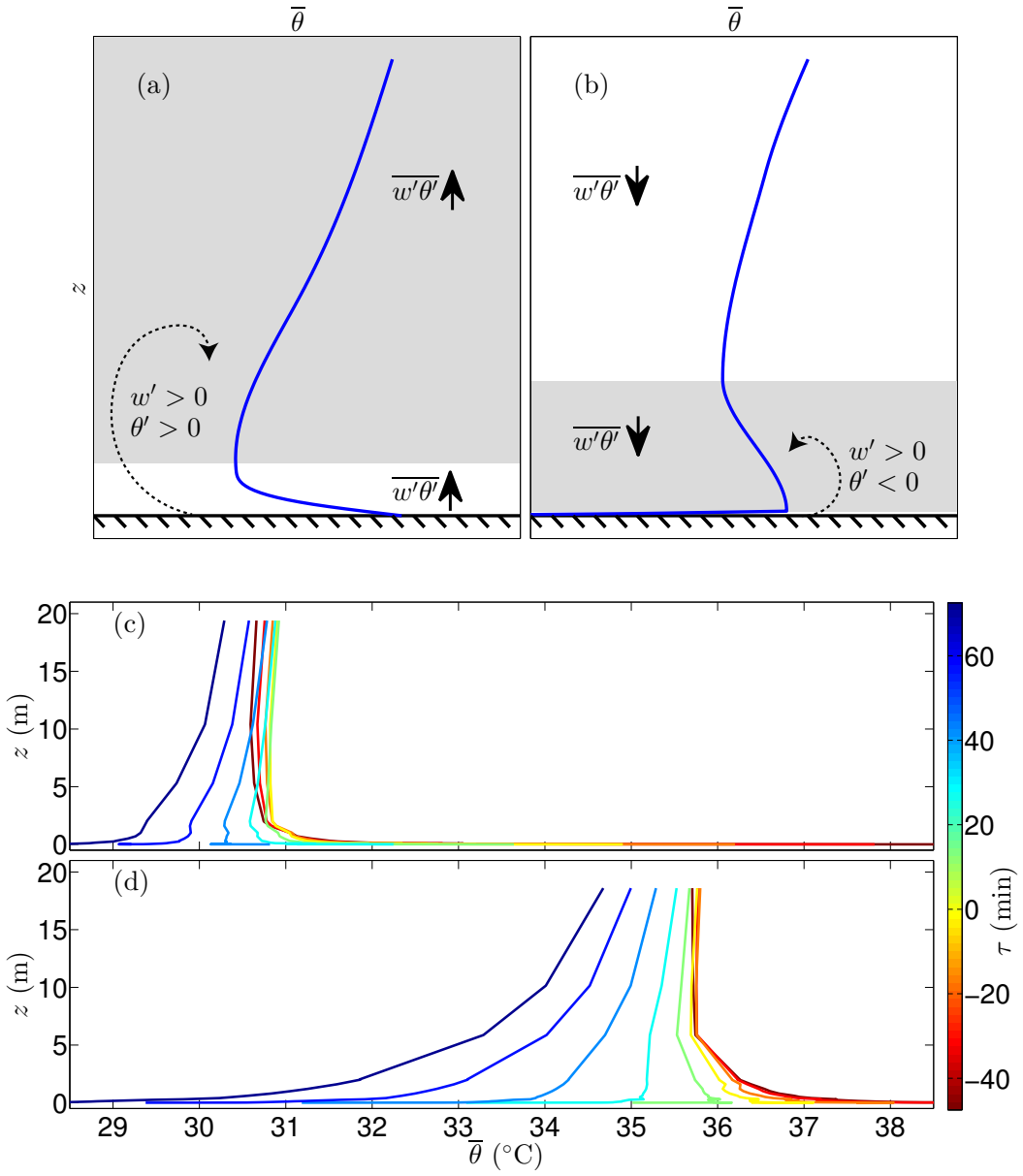

Figure 2.9: Schematic of the countergradient behaviour and observed potential temperature profiles at Playa (**a**,**c**) and Sagebrush (**b**,**d**). The shaded portions of the schematics indicate layers with countergradient heat fluxes. The observed temperature profiles include the radiative surface temperature, near-surface thermocouple arrays, and tower thermocouple datasets. Some levels in the thermocouple arrays displayed obvious instrumentation errors and were discarded. The profile observation heights at Playa are: 0, 0.01, 0.02, 0.035, 0.05, 0.075, 0.10, 0.15, 0.20, 0.25, 0.30, 0.50, 0.70, 1.0, 1.6, 2.0, 2.02, 5.3, 10.4, 19.4 m and at Sagebrush: 0, 0.01, 0.02, 0.035, 0.05, 0.075, 0.10, 0.125, 0.15, 0.20, 0.25, 0.30, 0.40, 0.50, 0.60, 0.80 1.0, 1.2, 1.6, 2.0, 2.04, 5.87, 10.15, 18.60 m. A 30-min running average was applied with profiles generated at 15-min intervals.

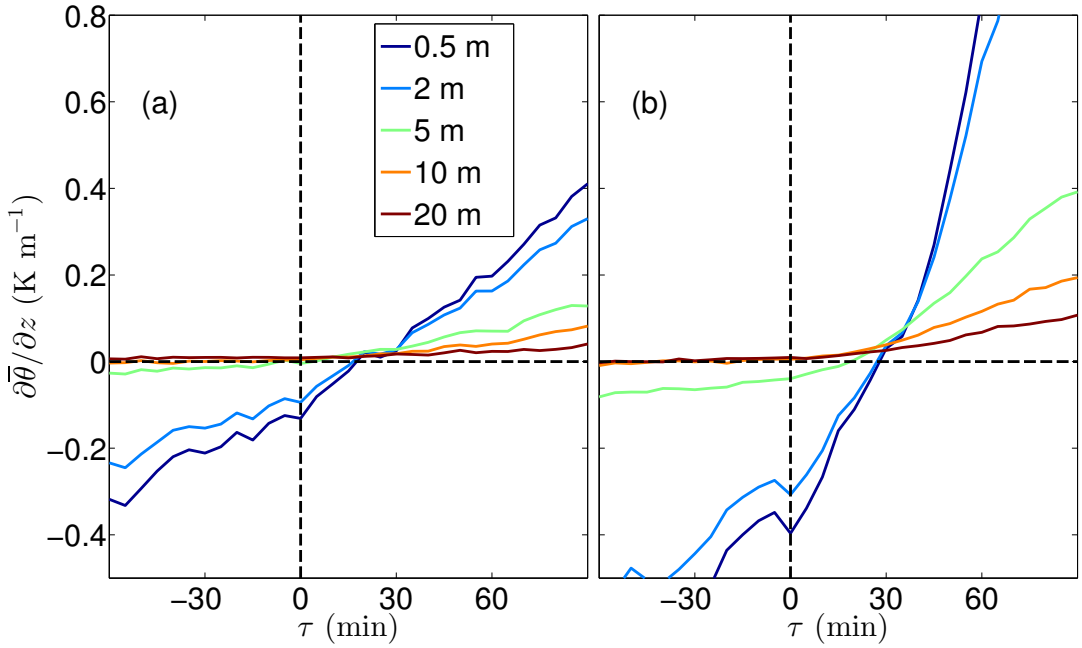

Figure 2.10: Time series of the mean potential temperature gradient for all heights at Playa (**a**) and Sagebrush (**b**). τ = 0 is the net-radiative sunset. The top-down gradient reversal times are $\overline{\tau_{\text{grad,Playa}}}(z = 0.5, 2, 5, 10, 20 \text{ m})$ = 15, 15, 0, –40, –195 min and $\overline{\tau_{\text{grad,Sagebrush}}}(z = 0.5, 2, 5, 10, 20 \text{ m})$ = 25, 25, 15, –20, –40 min.

net-radiative sunset. The gradients at 10 and 20 m at Sagebrush are quasi-neutral and slowly begin to stabilize slightly before $\tau = 0$. This is also the case at the Playa site, however at Playa, the 5-m gradient is also quasi-neutral before stabilization occurs. At both sites, the weak gradients aloft cross zero before the stronger, near-surface gradients at 0.5 and 2 m. Additionally, there is never a period where all of the gradients are near-neutral. In fact, at both sites there appears to be a brief period where all of the gradients are approximately equal and weakly stable. This abrupt transition through zero supports the modeling work of Jiménez et al. (2012) and observations of Acevedo and Fitzjarrald (2001) where the transition through neutral stratification happens abruptly.

The weak gradients aloft help to explain why the gradient reversal occurs from the top down. Temperature tendency profiles are shown in Fig. 2.11. Once again, the magnitude of the cooling at Sagebrush is much larger than that at Playa. At both sites the cooling is largest and initiated near the ground. The stabilization in the layer is proportional to the slope of the temperature tendency profile. Therefore, while stabilization is occurring most rapidly near the surface, the very weak gradients aloft are able to change sign with a very small amount of stabilization, resulting in the observed top-down behaviour.

To understand the mechanism of the cooling, the simplified temperature tendency equation is considered (e.g. Acevedo and Fitzjarrald, 2001):

$$\underbrace{\frac{\partial \overline{\theta}}{\partial t}}_{\text{I}} = \underbrace{-\frac{\partial \overline{w'\theta'}}{\partial z}}_{\text{II}} + \underbrace{ADV_\theta - \frac{\partial R_n}{\partial z}}_{\text{III}} \tag{2.5}$$

where term I is the rate of change in temperature, II is the sensible heat-flux divergence, and III, which is computed as the residual, is the sum of all advective effects (ADV_θ) and the radiative flux divergence ($\frac{\partial R_n}{\partial z}$). It is expected that early in the EET, temperature advection will be relatively small and gradually increase in importance as the size of the mixing eddies decreases and surface heterogeneities are amplified (Acevedo and Fitzjarrald, 2001, 2003).

The terms of Eq. 2.5 are shown for 5 m at both sites in Fig. 2.12. When terms II or III are greater than zero, they are warming the layer; when they are less than zero,

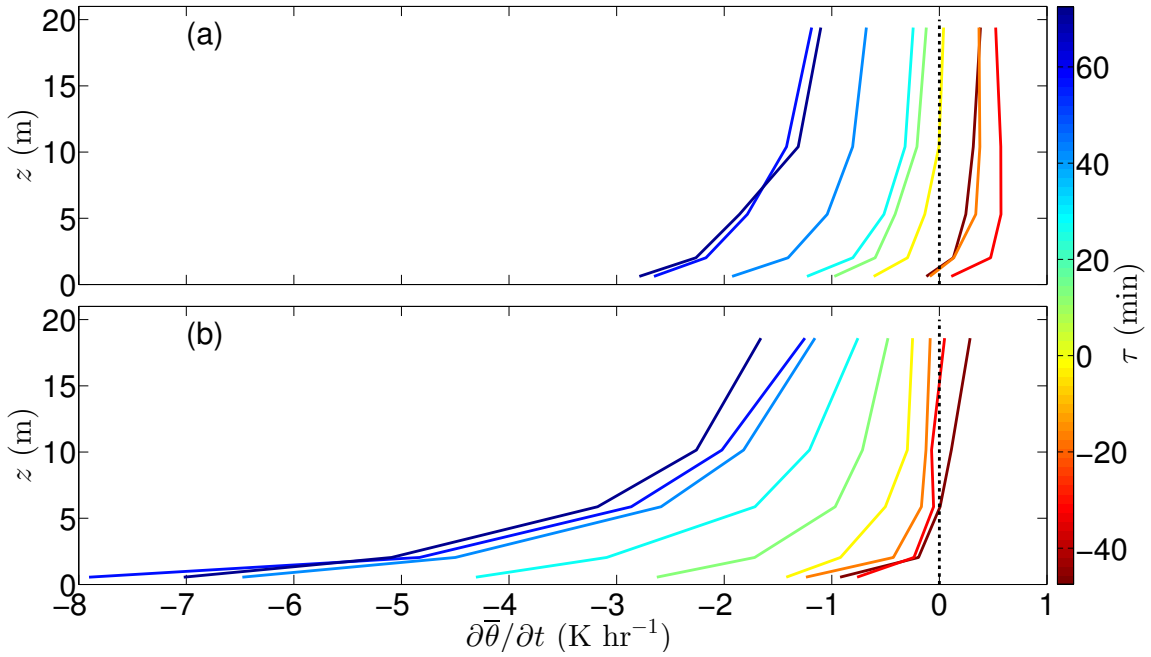

Figure 2.11: Profiles of $\partial\overline{\theta}/\partial t$ at Playa **(a)** and Sagebrush **(b)**. To the right of the dashed line, heating is occurring and to the left of the dashed line, cooling is. A 30-min running average was applied with profiles generated at 15-min intervals.

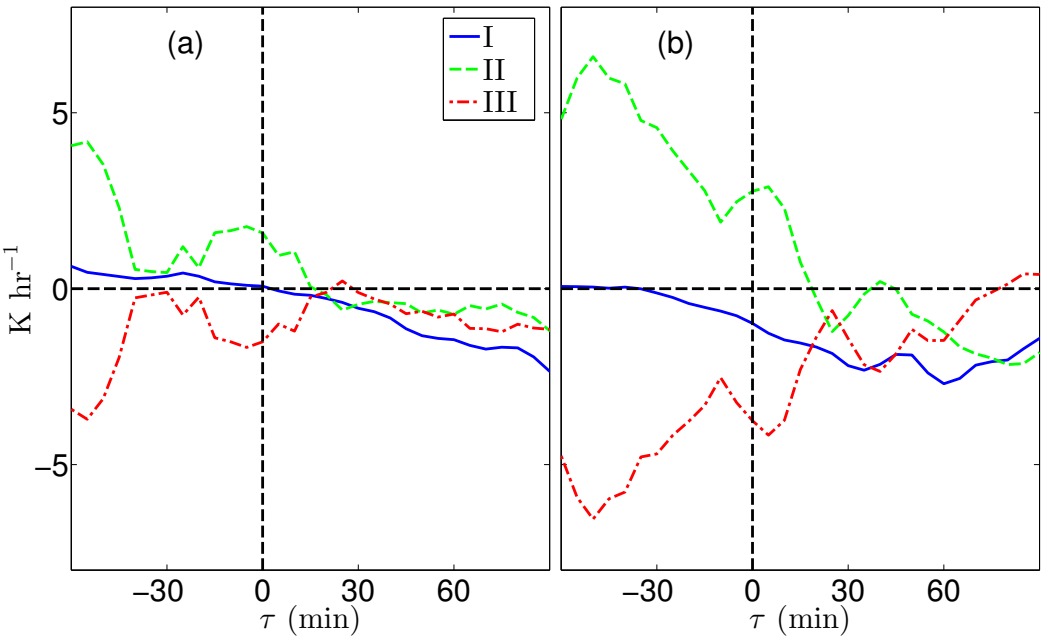

Figure 2.12: Terms of the simplified temperature tendency equation (Eq. 2.5) for 5 m at Playa (**a**) and Sagebrush (**b**). Term I is the local time change of temperature, term II is the sensible heat-flux divergence and term III is the cumulative effect of advection and radiative flux divergence. Term III is computed as a residual. A 25-min running average is used to smooth the ensembled data.

they are cooling the layer. At the Playa site, the heat-flux divergence begins to cool the layer at approximately the same time term I becomes negative. That is, there is a heat-flux convergence in the layer until the layer begins to cool (I< 0), at which point the convergence gradually shifts to a divergence. The maximum cooling rate is then in approximate agreement with the largest heat-flux divergence, consistent with the findings of Acevedo and Fitzjarrald (2001). However, the magnitude of term I quickly becomes larger than term II, indicating that radiative flux divergence, subsidence and advection may become important. Term I shows no clear minimum (or maximum cooling rate) over the time range shown. This is due to smoothing associated with the ensemble averaging over several days. When individual days are considered (not shown), the time series of T often shows an abrupt decrease in temperature followed by an inflection point, indicating the mechanical turbulence has decayed (Fitzjarrald and Lala, 1989).

At the Sagebrush site, the magnitudes of term I and II are much larger. This is due to the stronger heat fluxes and temperature gradients at Sagebrush. The air begins to cool (term I) significantly before the gradient of the heat flux (term II) changes sign, with much of the cooling occurring in the presence of a weak sensible heat-flux convergence. This is counter to the findings of Acevedo and Fitzjarrald (2001), where the maximum cooling rate was found to coincide with the maximum heat-flux divergence. Considering the relative homogeneity of both sites, and presumably weak advection, it appears that radiative flux divergence and possibly subsidence become important earlier in the EET than previously thought (Acevedo and Fitzjarrald, 2001) and should not be neglected in models. When other tower heights are considered (not shown), the observed behaviour is very similar to the 5-m level, however the relative magnitude of the terms decreases with height.

2.3.4 Heat-Flux Evolution

The mean sensible heat-flux evolution is shown in Fig. 2.13. At the Playa site, the decay is gradual with a small amount of variability and a slight heat-flux convergence for $\tau < 0$. The heat flux at all levels reverses direction at approximately the same time and a weak heat-flux divergence gradually develops through the evening transition.

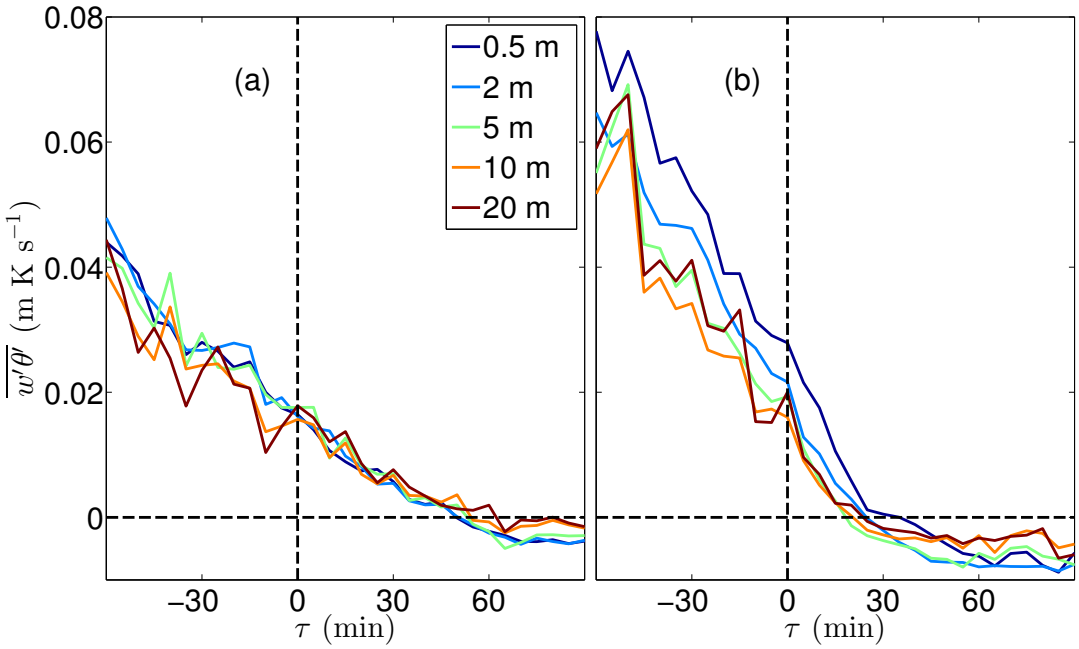

Figure 2.13: Time series of the ensemble sensible heat flux for all heights at Playa (**a**) and Sagebrush (**b**).

At the Sagebrush site, the decay is much more abrupt, with heat-flux convergence occurring until $\tau \approx 20$ min. The heat flux at levels above 0.5 m reverses direction at approximately the same time with the 0.5-m flux crossing 5–10 min later. This is likely due to sheltering from the surrounding vegetation. Later in the evening transition, the negative fluxes at Sagebrush become stronger than those observed at Playa with a sensible heat-flux divergence developing around $\tau = 45$ min.

Similar to the temperature gradient evolution, the heat-flux evolution is discussed in terms of its simplified tendency equation. Here we used the simplified budget for horizontally homogeneous terrain from Wyngaard et al. (1971):

$$\underbrace{\frac{\partial \overline{w'\theta'}}{\partial t}}_{\text{I}} = \underbrace{-\overline{w'^2}\frac{\partial \overline{\theta}}{\partial z}}_{\text{II}} \underbrace{-\frac{\partial(\overline{w'^2\theta'})}{\partial z}}_{\text{III}} \underbrace{+\frac{g}{\overline{\theta}}\overline{\theta'^2}}_{\text{IV}} \underbrace{-\frac{1}{\rho}\overline{\theta'\frac{\partial p'}{\partial z}}}_{\text{V}} \tag{2.6}$$

where term I is local storage, II is gradient production, III is the turbulent transport, IV is buoyant production and V is the pressure destruction. Subsidence, advection, and molecular dissipation are assumed to be small. Terms I – IV are computed directly and term V is computed as a residual. The mean terms at 5 m are shown in Fig. 2.14. Again, the relative magnitudes of the terms are much larger at the Sagebrush site. This is due to the larger temperature gradients and increased surface roughness at Sagebrush. For $\tau < 0$, the buoyant production term (IV) is more important than the gradient production (II) at the Playa site, while the opposite is true at the Sagebrush site. By definition, IV is always positive, meaning that IV will always delay the decay of the sensible heat flux. Term II has the opposite sign of the local gradient, meaning that II will force the heat flux to decay in consonance with the local gradient reversal. The turbulent transport (III) is relatively noisy but insignificant at both sites. Term V, which is computed as a residual, is quite large at the Sagebrush site and becomes a source of sensible heat flux later into the EET, indicating that advection is likely important during this process.

We hypothesize that the relative importance of terms II and IV leading up to the flux reversal plays a fundamental role in the observed countergradient behaviour. When buoyant production (IV) is substantially larger than gradient production (II), we expect that the decay will be delayed and the positive heat flux will persist in the

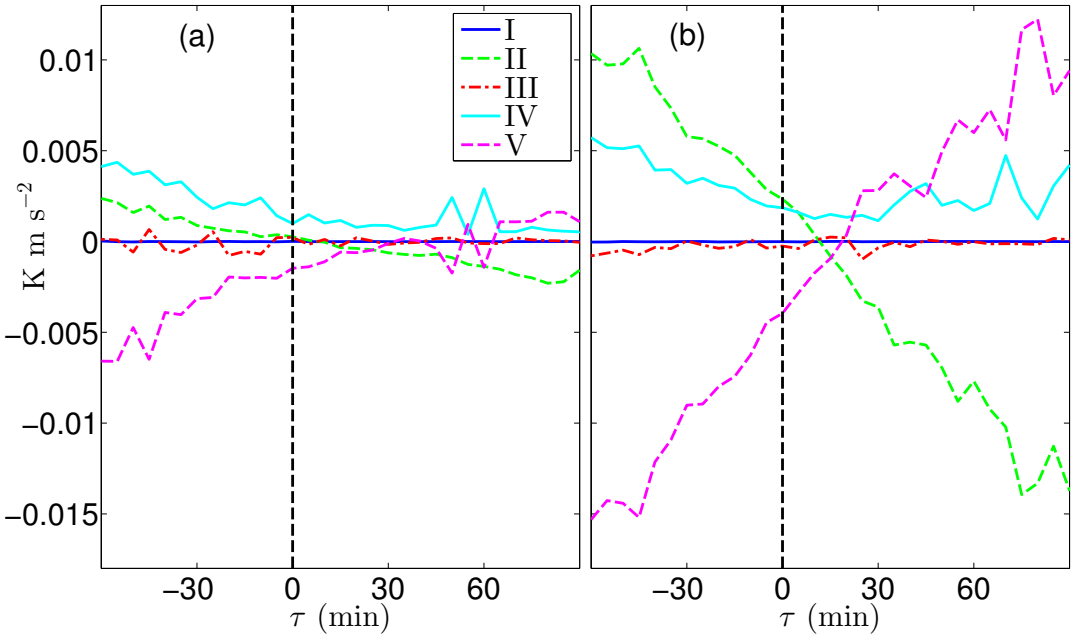

Figure 2.14: Terms in the heat-flux tendency equation (Eq. 2.6) at 5 m for the Playa (**a**) and Sagebrush (**b**) sites. Term I is local storage of sensible heat, II is gradient production, III is the turbulent transport, IV is buoyant production and V is the pressure destruction.

presence of a stable temperature gradient ($t_{\text{lag}} > 0$). Conversely, when term II is more important than term IV we expect the behaviour observed by Blay-Carreras et al. (2014). That is the heat flux reversal occurs in the presence of a weakly unstable temperature gradient ($t_{\text{lag}} < 0$). The reason for the flux reversal occurring before the gradient reversal is discussed above (see Fig. 2.9 and associated discussion).

To test this hypothesis, the ratio II/IV is plotted for all heights in Fig. 2.15. For a prolonged period before flux reversal occurs, there is a period at all locations where the ratio II/IV is approximately constant. This late-afternoon (LA) ratio ($\text{II/IV}|_{LA}$) determines the type and duration of the countergradient behaviour, where $\text{II/IV}|_{LA} \approx 1.6$ is evidently a critical value. For $\text{II/IV}|_{LA} > 1.6$, t_{lag} is less than zero (the behaviour observed by Blay-Carreras et al. (2014)). For $\text{II/IV}|_{LA} < 1.6$, t_{lag} is greater than zero. This general behaviour is illustrated in Fig. 2.16. The countergradient duration is proportional to the difference between the observed late-afternoon ratio and 1.6. That is, the further $\text{II/IV}|_{LA}$ deviates from 1.6, the larger $|t_{\text{lag}}|$ becomes. The two regimes display different slopes that are likely the result of different physical mechanisms that are still uncertain. Further, there is uncertainty for the $\text{II/IV}|_{LA} >$ 1.6 region where only two ensemble averaged data points exist in the present study. Further studies are needed to verify this result.

2.4 Conclusions

Data from the MATERHORN Program were used to study near-surface, sensible heat-flux and temperature-gradient profiles through the early evening transition (EET) over two contrasting sites. The main conclusions are:

- During the EET, there is typically a lag between the time of local temperature-gradient reversal and local heat-flux reversal, leading to a period of countergradient heat flux. The gradient reversal may precede the flux reversal ($t_{\text{lag}} > 0$) and vice-versa ($t_{\text{lag}} < 0$). The duration and type of countergradient behaviour is strongly height and site dependent.

- For both types of countergradient behaviour, the direction of the observed heat flux is dictated by the temperature difference between the surface and air above,

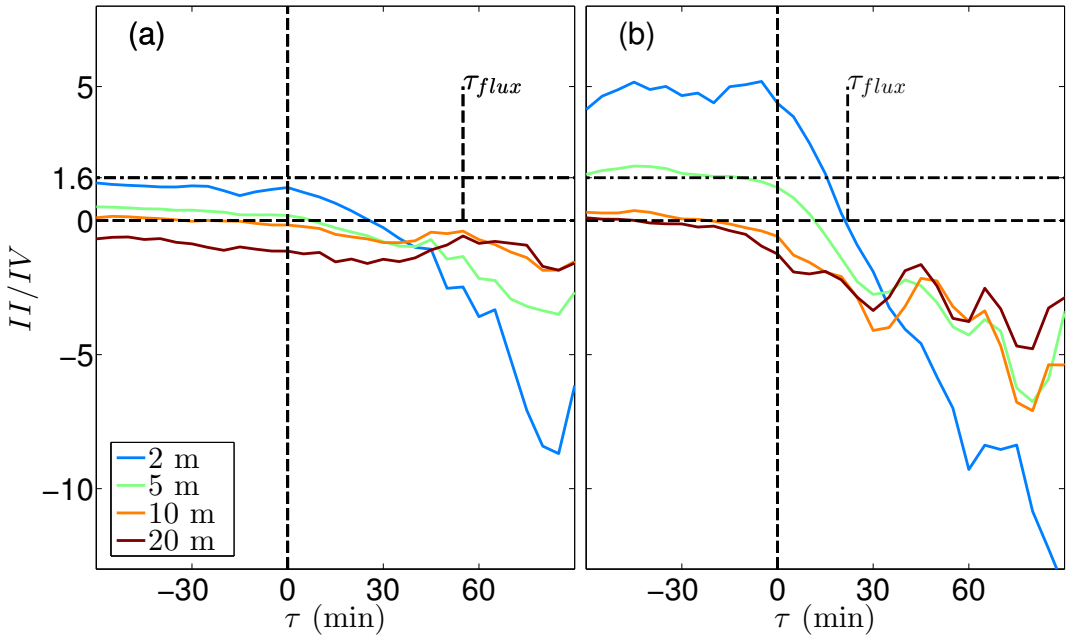

Figure 2.15: Time series of the ratios of gradient (II) to buoyant (IV) production from the heat-flux tendency equation (Eq. 2.6) for the Playa (**a**) and Sagebrush (**b**) sites. A 15-min running average is applied to smooth the data and the heat flux reversal is marked by τ_{flux} at both sites. The horizontal line at II/IV= 1.6 is a critical ratio. For late-afternoon (LA) ratios above this, the countergradient flux occurs when the flux reversal *precedes* the gradient reversal ($\tau_{\text{lag}} < 0$). For pre-transition ratios below 1.6, the countergradient flux occurs when the flux reversal *follows* the gradient reversal ($\tau_{\text{lag}} > 0$). The countergradient duration is proportional to the difference of the late-afternoon ratio and 1.6.

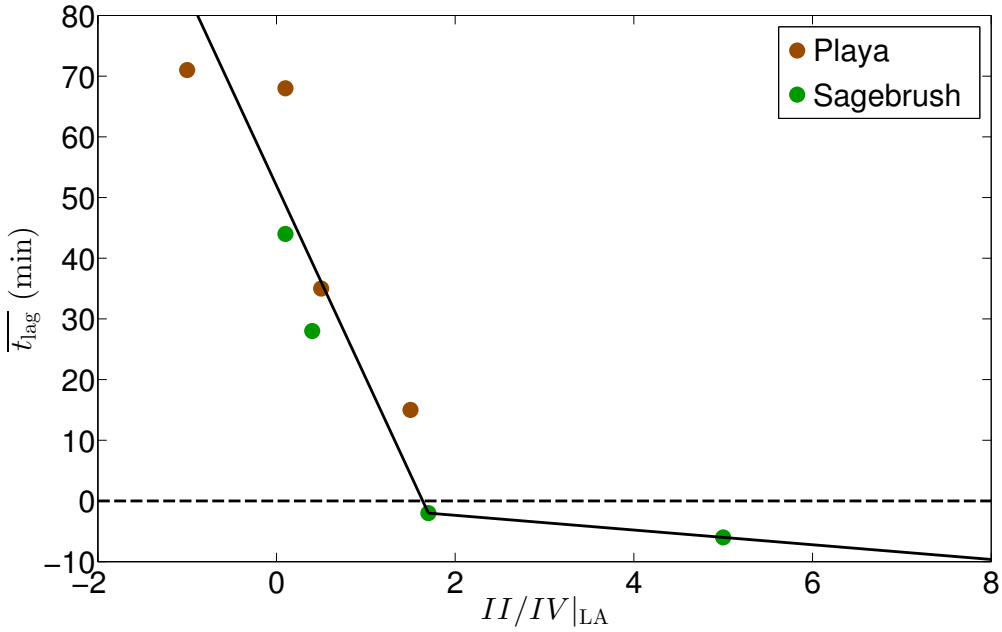

Figure 2.16: Mean lag times as a function of late-afternoon (LA) ratios of the gradient (term II) to buoyant production (term IV) terms in the heat-flux tendency equation (Eq. 2.6) for all heights at the Playa and Sagebrush sites. The solid black lines are a best, linear fit of the data.

rather than the temperature stratification of an individual air layer (Fig. 2.9).

- At Playa, the countergradient behaviour at all tower levels is due to the gradient reversal *preceding* the flux reversal. At Sagebrush, both types of countergradient behaviour are observed. For 10 and 20 m, the gradient reversal *precedes* the flux reversal, and for 5 m and below the gradient reversal *follows* the flux reversal.

- The gradient reversal propagates from the top down at a rate of approximately 4 min m^{-1} and displays site independence (Fig 2.6). The top-down behaviour is due to very weak gradients aloft that reverse with a small amount of stabilization (Figs. 2.10 and 2.11). The stabilization is not fully accounted for by the sensible heat flux divergence (Eq. 2.5 and Fig. 2.12), and it appears that radiative flux divergence, advection, and subsidence may all be important early in the EET.

- The heat-flux reversal occurs nearly simultaneously at all heights but displays site dependence, with the reversal at the Playa site occurring $\approx$ 30 min later than the Sagebrush site.

- Based on the top-down gradient reversal and simultaneous flux reversal, the countergradient behaviour can be estimated as a function of height if the gradient and flux reversal are known at a single level (Eq. 2.4).

- The type and duration of the countergradient behaviour can be predicted by comparing the relative strength of the gradient to buoyant production terms in the heat-flux tendency equation during the late afternoon. There appears to be a critical ratio of $\approx$ 1.6. If the ratio is greater than 1.6, the flux reversal is likely to precede the gradient reversal ($t_{\mathrm{lag}} < 0$), and if the ratio falls below 1.6, the opposite is true. The countergradient duration is proportional to the difference of the ratio and 1.6 (Fig. 2.16).

- At Playa, the high thermal conductivity and heat capacity of the soil prevent large temperature gradients from developing and therefore force the late-afternoon ratio of gradient to buoyant production to be less than 1.6 at all tower levels. At Sagebrush, the late-afternoon ratio for 5 m and below is greater than 1.6, and for 10 and 20 m is less than 1.6.

- Through the EET, both fluxes and vertical temperature gradients are small and evolve rapidly, indicating that instrument uncertainty may be significant. Instrumentation was meticulously calibrated and installed to minimize systematic and random error. The countergradient phenomenon is observed in both individual and ensemble averaged EET periods. Future studies are necessary to confirm the presented findings as well as to verify the general applicability of the results to other surface and subsurface types.

2.5 References

Acevedo, O. C. and D. R. Fitzjarrald, 2001: The early evening surface-layer transition: Temporal and spatial variability. *J. Atmos. Sci.*, **58**, 2650–2667.

Acevedo, O. C. and D. R. Fitzjarrald, 2003: In the core of the night – Effects of intermittent mixing on a horizontally heterogeneous surface. *Boundary-Layer Meteorol.*, **106**, 1–33.

Angevine, W. M., 2007: Transitional, entraining, cloudy, and coastal boundary layers. *Acta Geophys.*, **56**, 2–20.

Aubinet, M., T. Vesala, and D. Papale, 2012: *Eddy Covariance - A Practical Guide to Measurement and Data Analysis — Springer*. Springer Netherlands, 438 pp.

Blay-Carreras, E., E. R. Pardyjak, D. Pino, D. C. Alexander, F. Lohou, and M. Lothon, 2014: Countergradient heat flux observations during the evening transition period. *Atmos. Chem. Phys.*, **14**, 9077–9085.

Blay-Carreras, E., E. R. Pardyjak, D. Pino, S. W. Hoch, J. Cuxart, D. Martinez, and J. Reuder, 2015: Lifted temperature minimum during the atmospheric evening transition. *Atmos. Chem. Phys.*, **15**, 1–11.

Brown, A. R., et al., 2002: Large-eddy simulation of the diurnal cycle of shallow cumulus convection over land. *Q. J. R. Meteorol. Soc.*, **128**, 1075–1093.

Caughey, S. J. and J. C. Kaimal, 1977: Vertical heat flux in the convective boundary layer. *Q. J. R. Meteorol. Soc.*, **103**, 811–815.

Caughey, S. J., J. C. Wyngaard, and J. C. Kaimal, 1979: Turbulence in the Evolving Stable Boundary Layer. *J. Atmos. Sci.*, **36**, 1041–1052.

Chapra, S. and R. Canale, 2010: *Numerical Methods for Engineers*. 6th ed., McGraw-Hill Science/Engineering/Math, 960 pp.

Cole, G. S. and H. J. S. Fernando, 1998: Some aspects of the decay of convective turbulence. *Fluid Dyn. Res.*, **23**, 161–176.

Comte-Bellot, G. and S. Corrsin, 1971: Simple Eulerian time correlation of full- and narrow-band velocity signals in grid-generated, isotropic turbulence. *J. Fluid Mech.*, **48**, 273–337.

Deardorff, J., 1970: Convective velocity and temperature scales for the unstable planetary boundary layer and for Rayleigh convection. *J. Atmos. Sci.*, **27**, 1211–1213.

Dyer, A. J. and B. B. Hicks, 1970: Flux-gradient relationships in the constant flux layer. *Q. J. R. Meteorol. Soc.*, **96**, 715–721.

Edwards, J. M., R. J. Beare, and A. J. Lapworth, 2006: Simulation of the observed evening transition and nocturnal boundary layers: Single-column modelling. *Q. J. R. Meteorol. Soc.*, **132**, 61–80.

Emrick, V. and A. Hill, 1999: Classification of Great Basin plant communities occuring on Dugway Proving Ground, Utah. *Elus. Doc.*, **Paper 64**.

Erell, E., V. Leal, and E. Maldonado, 2005: Measurement of air temperature in the presence of a large radiant flux: An assessment of passively ventilated thermometer screens. *Boundary-Layer Meteorol.*, **114**, 205–231.

Fernando, H., et al., 2015: The materhorn: Unraveling the intricacies of mountain weather. *Bulletin of the American Meteorological Society*, **96 (11)**, 1945–1967.

Fitzjarrald, D. R. and G. G. Lala, 1989: Hudson valley fog environments. *J. Appl. Meteorol.*, **28**, 1303–1328.

Google Earth, 2013: Dugway Proving Ground, UT, USA. 40° 8 5.8956 N, –113° 27 7.7976 pp.

Goulart, A. G., B. E. J. Bodmann, M. T. M. B. de Vilhena, P. M. M. Soares, and D. M. Moreira, 2010: On the time evolution of the turbulent kinetic knergy spectrum for decaying turbulence in the convective boundary layer. *Boundary-Layer Meteorol.*, **138**, 61–75.

Grant, A. L. M., 1997: An observational study of the evening transition boundary-layer. *Q. J. R. Meteorol. Soc.*, **123**, 657–677.

Grimsdell, A. W. and W. M. Angevine, 2002: Observations of the afternoon transition of the convective boundary layer. *J. Appl. Meteorol.*, **41**, 3–11.

Jiménez, P. a., J. Dudhia, J. F. González-Rouco, J. Navarro, J. P. Montávez, and E. García-Bustamante, 2012: A revised scheme for the WRF surface layer formulation. *Mon. Weather Rev.*, **140**, 898–918.

Kang, H. S., S. Chester, and C. Meneveau, 2003: Decaying turbulence in an active-grid-generated flow and comparisons with large-eddy simulation. *J. Fluid Mech.*, **480**, 129–160.

Kumar, V., J. Kleissl, C. Meneveau, and M. B. Parlange, 2006: Large-eddy simulation of a diurnal cycle of the atmospheric boundary layer: Atmospheric stability and scaling issues. *Water Resour. Res.*, **42**, 1–18.

Kumar, V., G. Svensson, A. Holtslag, C. Meneveau, and M. B. Parlange, 2010: Impact of surface flux formulations and geostrophic forcing on large-eddy simulations of diurnal atmospheric boundary layer flow. *J. Appl. Meteorol. Climatol.*, **49**, 1496–1516.

Lothon, M. and D. H. Lenschow, 2011: Studying the afternoon transition of the planetary boundary layer. *Eos, Trans. Am. Geophys. Union*, **91**, 253–254.

Lothon, M., et al., 2014: The BLLAST field experiment: Boundary-Layer Late Afternoon and Sunset Turbulence. *Atmos. Chem. Phys.*, **14**, 10 931–10 960.

Mahrt, L., 1999: Stratified atmospheric boundary layers. *Boundary-Layer Meteorol.*, **90**, 375–396.

Malek, E., 1997: Evaluation of effective atmospheric emissivity and parameterization of cloud at local scale. *Atmos. Res.*, **45 (1)**, 41–54.

Monin, A. S. and A. M. Obukhov, 1954: Basic laws of turbulent mixing in the surface layer of the atmosphere. *Contrib. Geophys. Inst. Acad. Sci.*, **24**, 163–187.

Nadeau, D. F., E. R. Pardyjak, C. W. Higgins, H. J. S. Fernando, and M. B. Parlange, 2011: A simple model for the afternoon and early evening decay of convective turbulence over different land surfaces. *Boundary-Layer Meteorol.*, **141**, 301–324.

Nieuwstadt, F. T. M. and R. A. Brost, 1986: The decay of convective turbulence. *J. Atmos. Sci.*, **43**, 532–546.

Pino, D., H. J. J. Jonker, J. V.-G. D. Arellano, and A. Dosio, 2006: Role of shear and the inversion strength during sunset turbulence over land: Characteristic length scales. *Boundary-Layer Meteorol.*, **121**, 537–556.

Rizza, U., M. Miglietta, G. Degrazia, O. Acevedo, and E. Marques Filho, 2013: Sunset decay of the convective turbulence with Large-Eddy Simulation under realistic conditions. *Physica A*, **392**, 4481–4490.

Sorbjan, Z., 1997: Decay of convective turbulence revisited. *Boundary-Layer Meteorol.*, **82**, 503–517.

Stull, R., 1988: *An Introduction to Boundary Layer Meteorology*. Springer Science, 666 pp.

Taylor, A. C., R. J. Beare, and D. J. Thomson, 2014: Simulating dispersion in the evening-transition boundary layer. *Boundary-Layer Meteorol.*, **153**, 389–407.

Vickers, D. and L. Mahrt, 1997: Quality control and flux sampling problems for tower and aircraft data. *J. Atmos. Ocean. Technol.*, **14**, 512–526.

Webb, E. K., G. I. Pearman, and R. Leuning, 1980: Correction of flux measurements for density effects due to heat and water vapour transfer. *Q. J. R. Meteorol. Soc.*, **106**, 85–100.

Wilczak, J. M., S. P. Oncley, and S. A. Stage, 2001: Sonic anemometer tilt correction algorithms. *Boundary-Layer Meteorol.*, **99**, 127–150.

Wyngaard, J. C., O. R. Cot, and Y. Izumi, 1971: Local free convection, similarity, and the budgets of shear stress and heat flux. *J. Atmos. Sci.*, **28**, 1171–1182.

CHAPTER 3

THE EVOLUTION AND SENSITIVITY OF KATABATIC FLOW DYNAMICS TO EXTERNAL INFLUENCES THROUGH THE EVENING TRANSITION

3.1 Introduction

Over sloping terrain, during clear-sky conditions with undisturbed weather, horizontal temperature gradients between the near-slope and ambient air masses lead to upslope daytime (anabatic) flow and downslope nighttime (katabatic) flow. Katabatic flows have been observed for very shallow slopes of $\ll 1^\circ$ (Brost and Wyngaard, 1978; Mahrt and Larsen, 1990; Whiteman and Zhong, 2008) and in the presence of strong synoptic forcing (Davidson and Rao, 1963; Banta and Cotton, 1981; Mahrt and Larsen, 1990). Within the stable boundary layer, katabatic flows develop over nearly the entire land surface of the Earth (Stull, 1988). For small-scale slopes in mountainous regions, katabatic flows have been found to accelerate and deepen with distance down the slope. The near-surface temperature inversion, which is responsible for driving the flow, has a depth often approximated as 5% of the ridge-top elevation drop where the wind-speed maximum typically occurs somewhere between 0.2 and 0.5 times the inversion depth (Manins and Sawford, 1979a,b; Horst and Doran, 1986). For shallow or steep slopes with complex topography, these approximations rarely hold (e.g. Davidson and Rao, 1963; McKee and O'Neal, 1989; Hunt et al., 2003; Nadeau et al., 2013; Grachev et al., 2016).

The strength, structure and onset of the katabatic flow are a function of the local surface energy balance, ambient stratification, slope elevation and azimuth angles, surrounding topography, roughness elements, and other circulations covering a range

of scales (Neff and King, 1987; Whiteman, 2000; Zardi and Whiteman, 2013). The katabatic onset may occur simultaneously over the entire slope ("sheet transition", Fernando et al., 2013; Villagrasa et al., 2013), propagate down the slope as a front ("front transition", Hunt et al., 2003; Brazel et al., 2005; Pardyjak et al., 2009; Fernando et al., 2013), or follow the direction of the shadow front, upslope for upward propagating shadows (Nadeau et al., 2013) and downslope for downward propagating shadows (Lehner et al., 2015). Furthermore, the katabatic structure and timing can vary dramatically from one day to the next with the onset of the katabatic flow sometimes occurring significantly before or after local sunset (e.g. Banta et al., 2004; Pardyjak et al., 2009; Nadeau et al., 2013, this study).

The conditions governing the katabatic flow can be divided into internal and external influences (Poulos and Zhong, 2008). Internal influences include the interaction between the predominant katabatic flow and tributaries (Erasmus, 1993; Start et al., 1974) and sporadic breakdowns or oscillations within the katabatic flow and surrounding stable boundary layer (Buettner and Thyer, 1965; Manins and Sawford, 1979b; Nappo, 1991). External influences include ambient winds (e.g. Banta and Cotton, 1981; Arritt and Pielke, 1986; Mahrt and Larsen, 1990; Savage et al., 2008), ambient stratification (Neff and King, 1987), cloud cover (Barr and Orgill, 1989; Villagrasa et al., 2013), shadow fronts (Nadeau et al., 2013; Lehner et al., 2015), land cover and soil type and soil moisture. While the influence of ambient winds has been the subject of much previous work, other external variables influencing the katabatic flow have received much less attention. For example, soil moisture plays a strong modulating role in the surface energy balance (McCumber and Pielke, 1981; Massey et al., 2014) and is therefore expected to influence the katabatic flow; however, we are unaware of any observational studies quantifying the relationship. The reason for there being relatively few observational studies investigating the influence of other such external variables influencing the katabatic flow is likely due to the difficulty of isolating one external factor from another (Poulos and Zhong, 2008). Fig. 3.1 gives a schematic of the slope in this study and also illustrates the complexity of the external variables influencing the katabatic flow.

While observational studies are lacking, numerical simulations have been used to

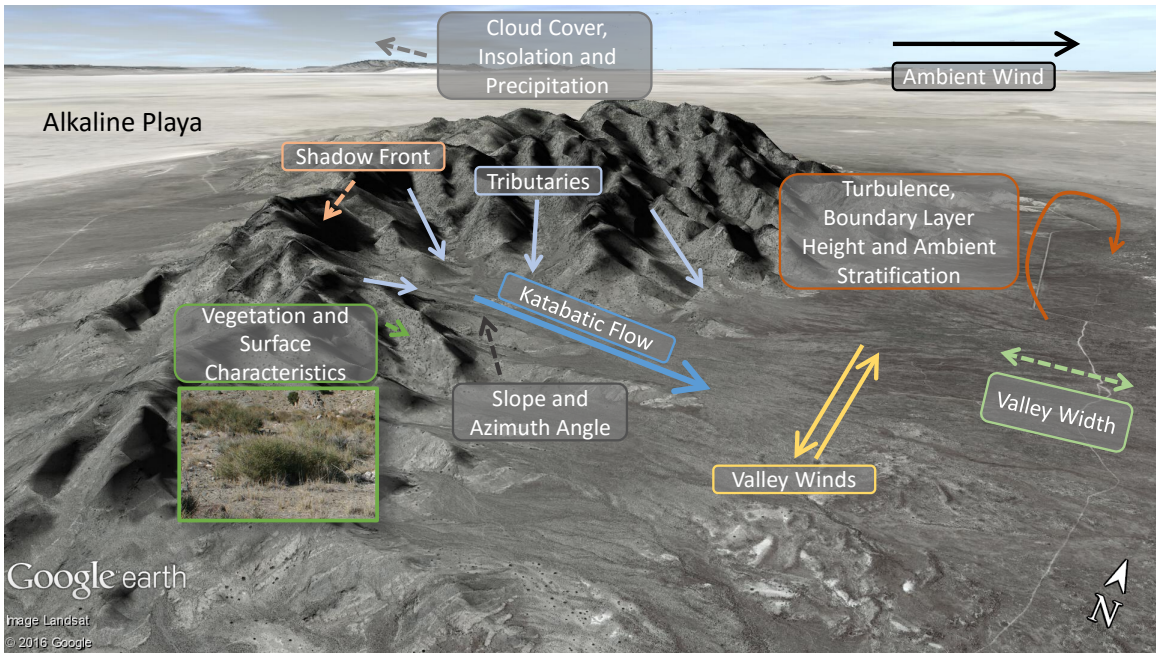

Figure 3.1: Schematic of Granite Peak in the Dugway Proving Ground, utilizing a Google Earth Landsat Image (Google Earth, 2013). The overlay illustrates the complexity of the interaction of the katabatic flow with surrounding external influences. The blue arrow, illustrating the katabatic flow, indicates the approximate transect of instrumentation on the east slope. Solid arrows indicate fluid flow and dashed arrows highlight features. See Fig. 3.2 for exact instrument locations.

study the impact of such external conditions. Ookouchi et al. (1984) found that for increased soil moisture, the magnitude of the daytime anabatic flow is reduced by $\approx 30\%$ due to a decrease in sensible heat flux. For katabatic flows, the simulations of Banta and Gannon (1995) concluded that the katabatic onset is delayed and the flow speed reduced by a similar percentage. The katabatic simulations were run for silty loam and sandy soil types with the same result. Unlike the anabatic study of Ookouchi et al. (1984), the dominant mechanism in reducing the katabatic velocity is the increase in the thermal conductivity of the soil (K_{soil}). The increased soil thermal conductivity allows for heat exchange with a deeper layer of soil and effectively reduces the cooling at the slope surface which in turn retards the katabatic flow. Schmidli et al. (2009) found similar results over the Owens Valley and noted the importance of the soil moisture initialization. The Chow et al. (2006) results confirm the importance of the soil moisture initialization. Conversely, for regional-scale katabatic flows, the simulations of Savage et al. (2008) found that katabatic flow is insensitive to soil moisture, land cover and surface roughness. Finally, Colette et al. (2003) simulated the influence of topographic shading during the morning transition and found that the inclusion of shading significantly delays both the onset of the morning anabatic flow and the subsequent breakdown of the nocturnal stable layer.

In this study, data collected during the field campaigns of the Mountain Terrain Atmospheric Modeling and Observations (MATERHORN) Program are used to observationally investigate the sensitivity of the timing and structure of the katabatic flow through the evening transition (ET) to external influences. The unprecedented spatio-temporal observations taken during the MATERHORN program allow for a more comprehensive investigation than previously possible (Fernando et al., 2015). The structure of the paper is as follows. First, the mean timing and structure of the katabatic flow is discussed. Second, the slope aligned budgets of momentum and temperature and accompanying katabatic time scales are computed. Third, a katabatic model utilizing surface energy budget modeling and the hydraulic katabatic model of Manins and Sawford (1979a) is developed and evaluated. Finally, uni- and multivariate statistical analyses are used to quantify the influence of external variables on the katabatic flow.

3.2 Methods

The MATERHORN field program consisted of two, month-long field campaigns conducted at the US Army Dugway Proving Ground, approximately 100 km southwest of Salt Lake City, UT. The autumn campaign conducted from 26 Sept – 7 Nov 2012 with an emphasis on quiescent, thermally-driven conditions and the spring campaign was conducted from 1 May – 6 June 2013 with an emphasis on high synoptic activity. The primary objective of the program is to improve weather predictability in complex terrain. The focal point of the large, multi-institution effort was Granite Peak, a relatively isolated peak, with a maximum elevation of 850 m above the valley floor. Highly alkaline playa is found to the west and north of the peak and silt-loam soil with arid, desert vegetation to the east and south (Fig. 3.1). Full details of the experiment are described in Fernando et al. (2015).

3.2.1 Study Area

The site of the study is the east slope of Granite Peak, an east-west aligned slope ≈ 4 km in length that opens to an alluvial fan ≈ 2 km downslope from the ridgeline (Figs. 3.1 and 3.2). The primary observation sites are four turbulence towers, ES5–ES2, spanning the east slope of Granite Peak, ES5 being the highest on the slope and ES2, the lowest. ES5 sits in the canyon-like upper portion of the slope, ES4 sits near the opening of the alluvial fan and ES3 and ES2 sit in the more-shallow, lower portion of the slope. ES1 is on the valley floor and is used for ambient conditions. Due to limited data availability at ES1, a permanent weather station, Target R, is utilized to characterize the valley wind field (Fig. 3.2). The near-ridgeline pitch is ≈ 25° and then decreases to 2–4° over the experimental sites (Fig. 3.2 (b)). The vegetation is sparse desert steppe on the order of 1-m tall. The Dugway Proving Ground receives an average ≈ 200 mm of precipitation annually with the soil moisture frequently near the permanent wilting point between precipitation events. Given the arid conditions, even a small amount of precipitation can have a dramatic impact on the surface energy balance (McCumber and Pielke, 1981; Hang et al., 2016). The slope width increases with distance downslope. Near ES5 and ES4, the slope width is relatively narrow and a number of tributaries contribute to the along-slope wind system. At ES3 and

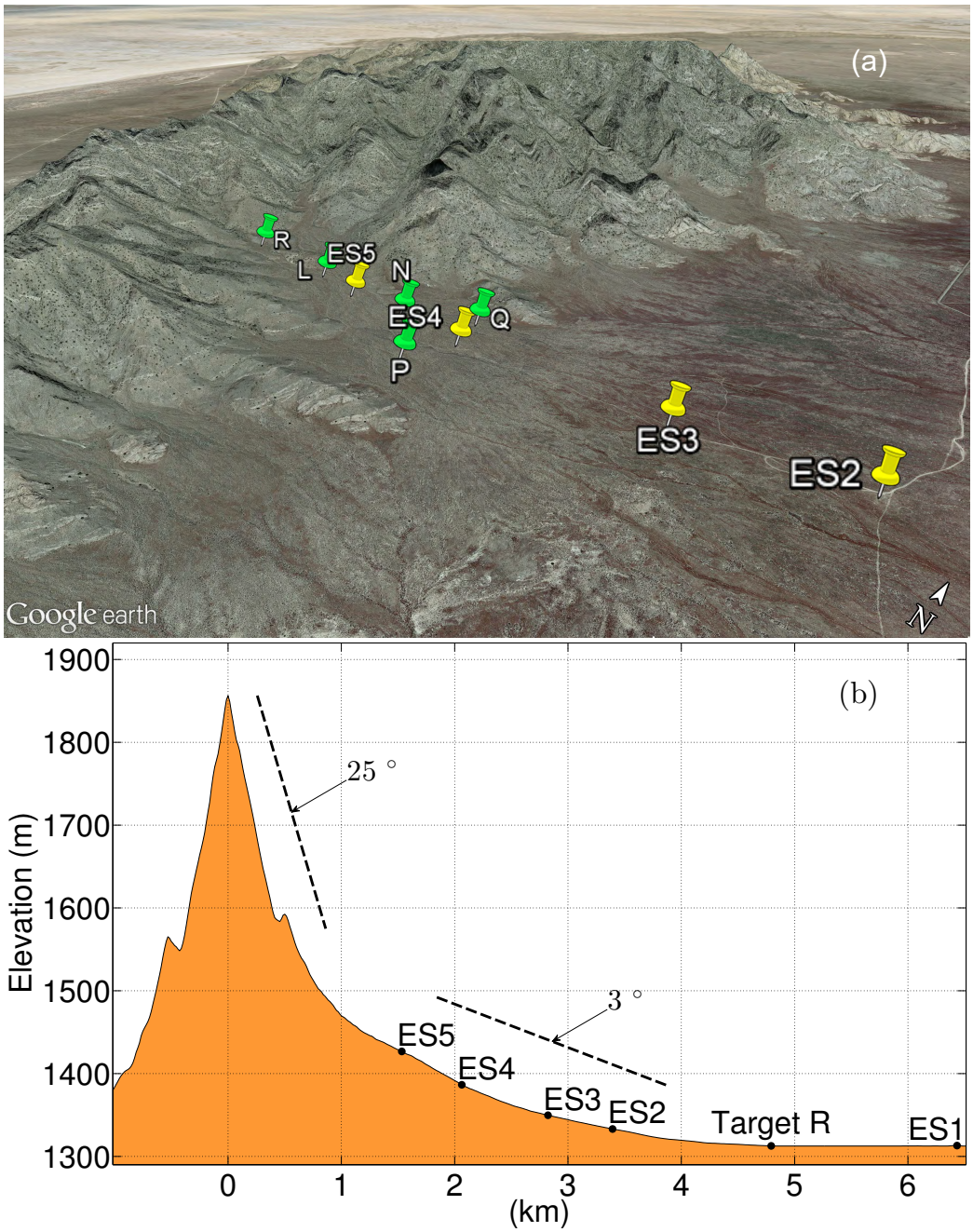

Figure 3.2: (a) Google Earth Landsat Image of the east slope. Yellow markers indicate turbulence towers and green markers indicate LEMS. ES1 and Target R are out of the view of the map. (b) Elevation Transect of the east slope. Target R is located on the valley floor, ≈ 750 m north of the slope transect defined by the five turbulence towers.

ES2, the slope width increases substantially and valley interactions frequently occur in the along-slope wind system.

3.2.2 Instrumentation

Each of the east slope (ES) towers was instrumented with a minimum of 5 levels of turbulent/slow-response instrumentation. The turbulence was recorded with 3-dimensional sonic anemometers sampled at 20 Hz and the slow-response air temperature (T) and relative humidity (RH) were measured with mean T/RH probes sampled at 1 Hz on Campbell Scientific CR3000 and CR5000 dataloggers. At ES5 and ES3, net radiometers observed the four components of the radiation budget. At ES5 only, the 50-mm soil volumetric water content ($VWC_{50\ \mathrm{mm}}$), soil thermal conductivity (K_{soil}) and ground heat flux (H_{g}) were also measured. Figure 3.3 illustrates the instrumentation deployed at each tower and Table 3.1 gives details and uncertainty for each instrument. At Target R, the 10-m average wind speed was measured with an RM Young 05103 wind monitor and the 5-min precipitation was monitored with a tipping bucket rain gauge.

In addition to the tower instrumentation, low-cost local energy-budget measurement stations (LEMS) were deployed at six locations throughout the slope (see Fig. 3.2) to observe incoming solar radiation, 2-m air temperature/relative humidity, pressure, surface temperature, soil moisture and soil temperature at depths of 50 and 250 mm. In this study, the LEMS are used solely to characterize the 50-mm soil moisture throughout the slope. The soil moisture is derived from the observed dielectric permittivity of the soil. A site-specific calibration was performed but showed no significant benefit over the generalized Topp equation (Topp et al., 1980), thus the latter was used to compute $VWC_{50\ \mathrm{mm}}$.

3.2.3 Data Analysis

Data for the analysis were processed with the Utah Turbulence in Environmental Studies processing and analysis code (UTESpac, Jensen et al., 2016). Due to the rapid evolution through the ET, fluxes, moments and mean variables were computed at 5-min intervals. In the field, the sonic anemometers were aligned with the gravitational vector and a 2-sector planar fit, divided between upslope and downslope winds, was

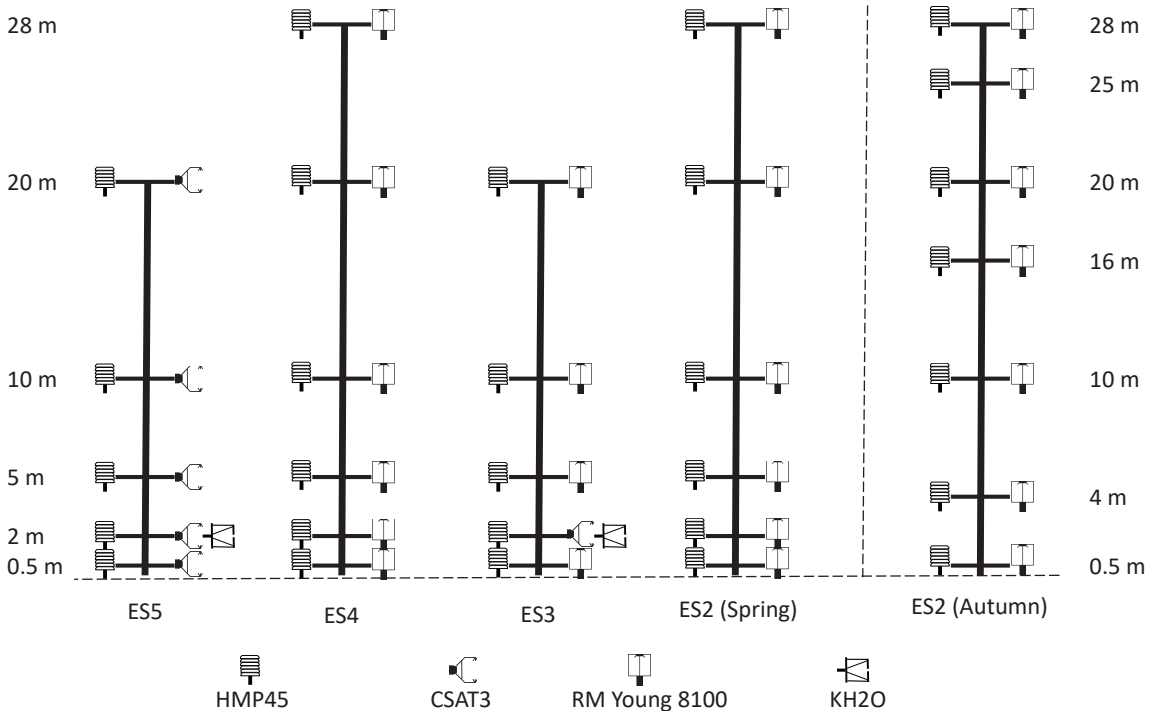

Figure 3.3: Relevant instrumentation on the four east slope towers during the MATERHORN Program. Note that the level heights change at ES2 between campaigns. Net radiometers were deployed at ES5 and ES3. At ES5 only, heat-flux plates (HFP01SC), an averaging soil thermocouple (TCAV), a soil-moisture probe (CS650) and a soil thermal-property sensor (TPO1) were also deployed. See Table 3.1 for instrument details.

Table 3.1: Relevant instrumentation deployed on the turbulence towers and LEMS. See Fig. 3.3 for instrument locations. Accuracy given as reported by the manufacturer. u, v and w are the slope-aligned, valley-aligned and slope-normal velocity components, respectively; T_s is the sonic-derived air temperature; H_2O is the mass density of H_2O; T is air temperature; RH is relative humidity; K_{soil} is the soil thermal conductivity; D is the soil thermal diffusivity; VWC is the soil volumetric water content; H_G is the ground heat flux and $\overline{T_G}_{\text{ 0–80 mm}}$ is the average soil temperature between 0 and 80 mm.

Instrument name	Variables measured	Accuracy	Manufacturer
	Tower Instrumentation		
CSAT3	u, v	±0.08 m s^{-1}	Campbell Sci.
	w	±0.04 m s^{-1}	
	T_s	n/a	
RMY8100	u, v, w	±0.05 m s^{-1}	R.M. Young
	T_s	± 2°C	
KH2O	H_2O	n/a	Campbell Sci.
HMP45	T	± 0.25°C	Vaisala
	RH	±2%	
TP01	K_{soil}	±5%	Hukseflux
	D	±20%	
CS650	VWC	±3%	Campbell Sci.
HFP01SC	H_{G}	±3%	Campbell Sci.
TCAV	$\overline{T_G}_{\text{ 0–80 mm}}$	±0.1°C	Campbell Sci.
	LEMS Instrumentation		
5TM	$VWC_{\text{50 mm}}$	±3%	Decagon
	T_G	±1°C	

applied with the sector-wise planar-fit coefficients computed from 30-min averaged wind data (Wilczak et al., 2001; Oldroyd et al., 2016). The ground heat flux (H_G) was computed as the sum of the flux measured at a depth of 80 mm and the heat storage in the layer of soil above the heat-flux plates (Campbell Sci., 2002).

3.3 Results and Discussion

The evolution of the slope moisture characteristics through both campaigns is illustrated in Fig. 3.4. The 50-mm VWC, albedo (α) and precipitation are reported, with the fifteen days considered in this study shaded grey. There are several rain events through both field campaigns that significantly alter the soil moisture and local energy budgets, which in turn are expected to alter the katabatic flow dynamics (Banta and Gannon, 1995). In general, the soil is more moist during the spring campaign which is evident from both the VWC observations and lower average albedo. For moister conditions, the spatial variability of soil moisture is higher, consistent with previous work over similar soil types (e.g. Henninger et al., 1976). However, at the nearby playa site (west and north or Granite Peak), Hang et al. (2016) observed higher spatial variability under dry soil conditions. The disparity between the two nearby locations is likely due to the differing soil types (alkaline playa vs. silt loam), sloping and runoff channels on the east slope, and background moisture level where the east slope is often near the wilting point while the playa soil is not. The effect of the increased VWC variability under moist conditions at the east slope is to increase heterogeneity in the surface energy balance (McCumber and Pielke, 1981), indicating that the slope wind system may be altered following rain events.

3.3.1 Katabatic Characterization

Due to frequent valley interaction at all ES towers, which typically occurs later into the night (Grachev et al., 2016; Lehner et al., 2015), this study focuses on the timing and structure of the katabatic flow through the ET. Here, we have defined the ET as 1 hr before to 3 hr after local sunset, where local sunset is defined at each site as the moment where the direct insolation drops to zero as the shadow front eclipses

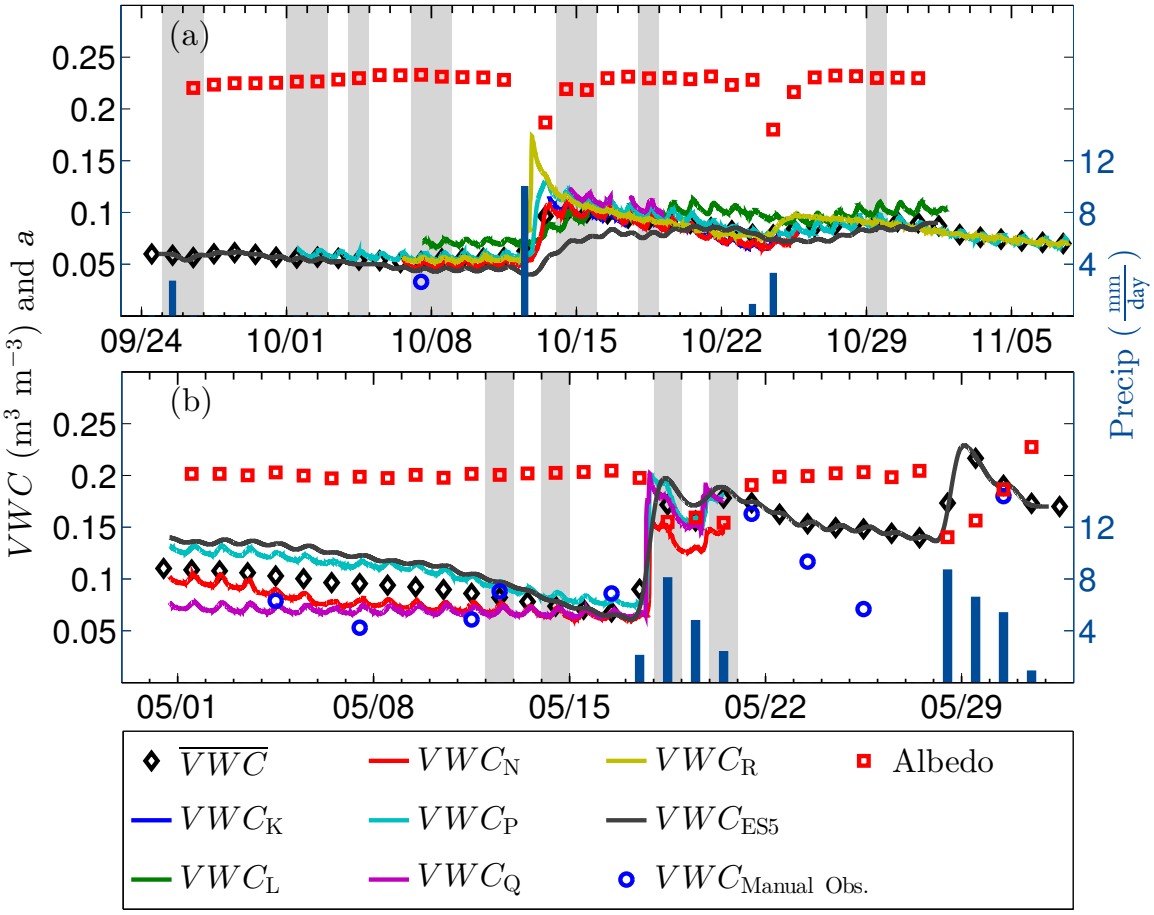

Figure 3.4: 50-mm volumetric water content, albedo and precipitation through the autumn (a) and spring (b) campaigns. $\overline{VWC}$ is the daily and slope averaged volumetric water content, VWC with a subscript is the 5-min VWC observation from the corresponding site and $VWC_{\text{ManualObs.}}$ is observations taken manually on the east slope (Hang et al., 2016). The apparent diurnal cycle in VWC is an artifact of the instrument's weak dependence on soil temperature. The overlayed bar plot gives daily precipitation. The days shaded gray are the fifteen days analyzed in this study. The dates are indicated in local standard time.

the tower. This definition differs from previous studies (e.g. Nadeau et al., 2011), but is used here because it typically captures the onset and evolution of the katabatic flow while minimizing the influence of the valley interactions that occur later in the night. Fifteen ETs, eleven from the autumn campaign and four from the spring (see Fig. 3.4 for dates), are utilized in the present study. The fifteen transitions are characterized by weak synoptic activity, well-defined katabatic flow through the ET, clear skies with a shadow front that propagates downslope and a katabatic onset which propagates down the slope. Of the three evenings considered in Grachev et al. (2016), only 2 October 2012 is common to both studies due to the differing study objectives. Though more rain fell during the spring (Fig. 3.4), high synoptic activity limited the number of suitable transitions during the spring campaign. Because pyranometers are only available at ES5 and ES3, a solar model, able to account for topographical shading at 10-m spatial and 5-min temporal resolution, is used to compute the incoming solar radiation at the four ES towers.

In order to characterize the katabatic flow, we define several variables:

- τ (min): Time relative to local sunset at a given tower. Because the shadow front propagates down the slope, τ must be defined locally at each tower. Prior to local sunset $\tau < 0$, $\tau = 0$ at local sunset and $\tau > 0$ after local sunset.

- τ_{kat} (min): The relative time of the katabatic initialization at a given tower. The katabatic initialization is taken as the first 5-min time step where the 10-m wind direction is pointed downslope (±45°) for a minimum of six consecutive time steps (e.g. if the 10-m wind direction at $\tau = 0$ min is not downslope but at $\tau = 5$, 10, 15, 20, 25 and 30 min the wind direction is downslope, then $\tau_{\mathrm{kat}}=$ 5 min). Though more complicated definitions of the katabatic initialization are possible (Papadopoulos and Helmis, 1999), we found the onset of a well-defined katabatic flow is best captured by this simple definition.

- z_{j} (m): Height of the katabatic jet computed from the vertical profile of momentum fluxes. The jet height is taken as the height above the ground where the linearly-interpolated momentum flux profile crosses zero. This is because momentum is transported toward the surface below the jet maximum and away

from the surface above the jet maximum. The momentum flux is expected to be near-zero at the jet maximum (Grachev et al., 2016). For profiles where no sign change is observed in the momentum flux, z_j is not calculated. The characteristic jet height for a given ET is taken as the mean jet height from τ_{kat} to the end of the ET.

- $\overline{u}_{kat}$ (m s^{-1}): Velocity of the katabatic jet, taken as the maximum velocity of the two anemometers encompassing the momentum flux sign change. When no sign change in the momentum flux is observed, $\overline{u}_{kat}$ is not calculated. The characteristic katabatic jet wind speed for a given ET is taken as the mean jet wind speed from τ_{kat} to the end of the ET.

- S_{KF} (m s^{-1}): Speed at which the katabatic front propagates downslope, computed from a linear fit of τ_{kat} at the four ES towers.

- S_{SF} (m s^{-1}): Speed at which the shadow front propagates downslope, computed from a linear fit of the time of local sunset at the four ES towers. Depending on season, the shadow front propagates in a northeast by east direction rather than due east (slope-aligned). The shadow front speed is computed from the four turbulence towers, thus it represents the easterly component of the shadow front propagation and is assumed to adequately describe the true shadow-front speed.

Sample velocity profiles at the four east slope towers are given in Fig. 3.5. The profiles are grouped by local standard time and the time relative to local sunset (τ) is indicated above each profile. The algorithm-determined relative time of the katabatic onset is indicated by "τ_{kat}" in the corresponding panel. At 1655, the wind profiles at all sites are pointed upslope and upvalley. At ES5, the wind is predominantly upslope and at ES2 the wind is predominantly upvalley. Forty min later at 1735, the wind at ES5 has nearly stopped and an $\approx$ 20-min calm period ensues. During the ES5 calm period, the upslope component at the other three sites decays to nearly zero, and the upvalley component decreases significantly at ES4 and ES3. At 1755, a coherent katabatic flow has developed at ES5 and the near-surface anemometers at the other

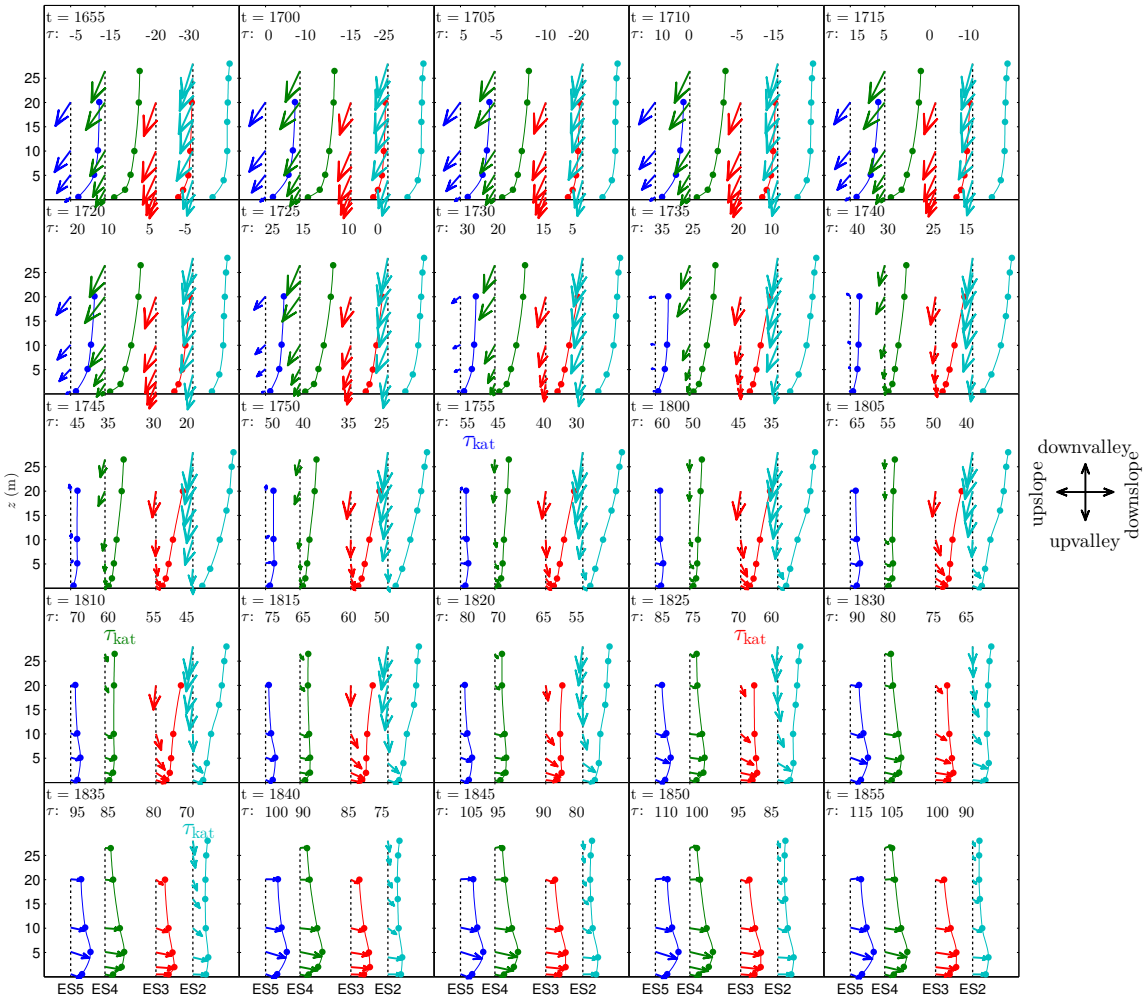

Figure 3.5: Sample velocity profiles observed on 10 Oct 2012 at the four ES towers. Spacing between the profiles is proportional to the actual horizontal distance separating the towers on the slope. The profiles are grouped by local standard time with the corresponding time relative to local sunset in min reported above the respective profile. The flow directions are shown with 3 m s^{-1} quivers to the right of the figure. The velocity magnitude is indicated by the solid curve. Interpolation of the velocity magnitude between levels is achieved with a piecewise cubic hermite interpolating polynomial performed with pchip.m, a function in the MATLAB® Statistics and Machine Learning Toolbox. The τ_{kat} marker indicates the katabatic onset at the given site.

sites indicate a shift toward downslope flow, while the upper-level anemometers still observe upvalley winds. By 1825, all sites but ES2 show coherent katabatic winds. Finally at 1835, ES2 has downslope components at all tower levels and the katabatic onset is determined to have initialized at all sites.

From the sample profiles, opinions may differ as to when the katabatic onset occurs. The near-surface anemometers ($z \leq 2$ m) observe a downslope wind component at all sites around 1755, indicating that the katabatic onset may occur earlier than what is calculated by the chosen algorithm (defined above). However, there are many instances where the 2-m wind speed points downslope for a period early in the ET and then rotates back upslope or upvalley. Also, the low-level maximum wind speed characteristic of katabatic flows is not observed at the towers until much later into the ET. This may be due to the superposition of the valley wind onto the slope-wind system, which, in some cases, may be elucidated by considering only the slope-aligned wind component. However, when only the slope wind component is considered, often the resulting early-evening profiles are somewhat chaotic with multiple local maxima over the height of the tower. Definitions requiring minimum downslope wind speeds, low-level wind-speed maxima and minimum katabatic depths were also explored. Upon qualitative examination of each definition, the potential algorithms at least occasionally failed to capture the onset of a persistent katabatic flow. Additionally, the more complicated definitions allowed for a large degree of ambiguity where the time of the katabatic onset could be altered significantly by a small change in the definition. After this analysis, we feel that the best indicator of the katabatic onset for an individual day is, as described above, simply a persistent downslope 10-m wind direction ($\pm 45°$) for a prolonged period (in this case, 30 min). Once this occurs, we observed that the katabatic flow typically persists, uninterrupted, through the remainder of the ET. This definition is simple, robust and easily identifiable because the 10-m wind velocity is a standard meteorological variable.

3.3.2 Mean Katabatic Characteristics

The katabatic velocity ($\overline{u}_{\mathrm{kat}}$), jet height ($z_{\mathrm{j}}$), onset ($\tau_{\mathrm{kat}}$) and katabatic front speed (S_{KF}) were computed for all ETs. The mean and standard deviations of the observations are reported in Table 3.2. As expected from theory (Manins and

Table 3.2: Katabatic timing and structure for all experimental days during the autumn and spring field campaigns. The mean value is reported first, followed by the standard deviation in brackets. The katabatic front (S_{KF}) and shadow front (S_{SF}) speeds are defined as positive for downslope propagating fronts.

Variable	ES5	ES4	ES3	ES2
$\overline{u}_{\mathrm{kat}}$ (m s^{-1})	2.09 [0.39]	2.25 [0.44]	2.19 [0.36]	2.15 [0.49]
z_{j} (m)	7.0 [1.7]	6.5 [2.3]	5.6 [2.2]	6.5 [4.1]
τ_{kat} (min)	34 [40]	32 [31]	52 [43]	34 [36]
S_{KF} (m s^{-1})		0.78 [0.59]		
S_{SF} (m s^{-1})		0.91 [0.21]		

Sawford, 1979a; Nappo, 1991), the katabatic flow shows a weak acceleration between ES5 and ES4. Beyond ES4, the flow decelerates slightly, likely due to the widening and shallowing of the slope (Fig. 3.2). The acceleration and subsequent deceleration of the katabatic flow as it propagates down the slope is small and is possibly due to data limitations and uncertainty in the jet-height calculation, though it is consistent with theory and the local topography. The total depth of the katabatic layer (not shown) deepens through the ET at all sites, typically exceeding the height of the towers within 2 hr of local sunset. In their case study during the spring campaign, Lehner et al. (2015) reported an approximate katabatic depth of 30 m through the ET, observed with a tethered balloon system located between ES2 and ES3.

Unlike the katabatic velocity, the downslope evolution in jet height shows greater intersite deviations. The height of the katabatic jet decreases with downslope distance between ES5 and ES3. This is counter to theory, and also likely due to the changing topography of the slope. At ES2, z_{j} increases, due to increased mixing associated with valley interactions. Because of variable valley-flow interactions, the variance of z_{j} at ES2 is much greater than at the other sites. The reason for the katabatic onset occurring significantly later at ES3 is somewhat unclear but is likely related to the somewhat smaller sample size at ES3 (due to instrumentation outages) and possibly to local effects.

The katabatic flow typically initializes $\approx$ 30 min after the local sunset with a relatively large degree of variability at all sites, indicating that the mean katabatic front speed moves downslope at approximately the same velocity as the shadow front,

offset by ≈ 30 min. The delay is similar to that observed by Nadeau et al. (2013), over a steep (> 30°) western facing slope. However, counter to the downslope katabatic front propagation discussed in Hunt et al. (2003), Nadeau et al. (2013) observed that the katabatic onset propagated up, rather than down, the slope, following the upward moving shadow front. In Nadeau et al. (2013), the immediate drop in insolation, and therefore net radiation, caused by the shadow front was much larger than observed over the east slope and the shadow front was the dominant mechanism in the flow reversal. Over the east slope, the mechanism is less clear. As mentioned above, both "front" and "sheet" transitions are observed. Additionally, the shadow front propagates downslope, making it difficult to distinguish between "front" driven (as discussed in Hunt et al. (2003)) and shadow-front driven transitions. In the case study of a single night over the east slope, Lehner et al. (2015) concluded that the transition over the east slope is driven predominantly by the shadow front. Given the high degree of interdiurnal variance, we conclude that all three mechanisms likely play a role in the initialization of the katabatic flow.

Figure 3.6 gives the individual and mean katabatic height and velocity evolution at ES5 for all ETs considered. For some ETs, sporadic jumps in z_{j} to heights of ≈ 15-m occur. There is no clear periodicity to the interval between jumps but it is ≈ 1 hr. To a lesser degree, corresponding accelerations are observed in $\overline{u}_{\mathrm{kat}}$. These oscillations are consistent with the katabatic breakdowns observed by Doran and Horst (1981), where adiabatic warming of the downward moving air parcel leads to an adverse pressure gradient that briefly retards the flow (Fleagle, 1950; McNider, 1982). In some cases (not shown), corresponding jumps in the turbulence kinetic energy (tke) are also observed. The period of the oscillations can be estimated with the relation $T = \frac{2\pi}{N\sin(\beta)}$ (McNider, 1982), where $N = \frac{g}{\theta_a}\frac{\partial\theta}{\partial n}$ is the Brunt-Väisälä frequency. The approximate slope angle at ES5 is $\beta = 3.6°$ and a typically observed slope-normal temperature gradient at ES5 through the ET is $\frac{\partial\theta}{\partial n} \approx 0.5$ K m^{-1}. This yields $T \approx 100$ min, which is in approximate agreement with the observed oscillations in the katabatic flow. The katabatic height and velocity both increase in magnitude until ≈ 120 min after sunset, at which point approximate equilibrium is achieved. The behavior at the other sites (not shown) is similar to that at ES5 but the number of gaps and

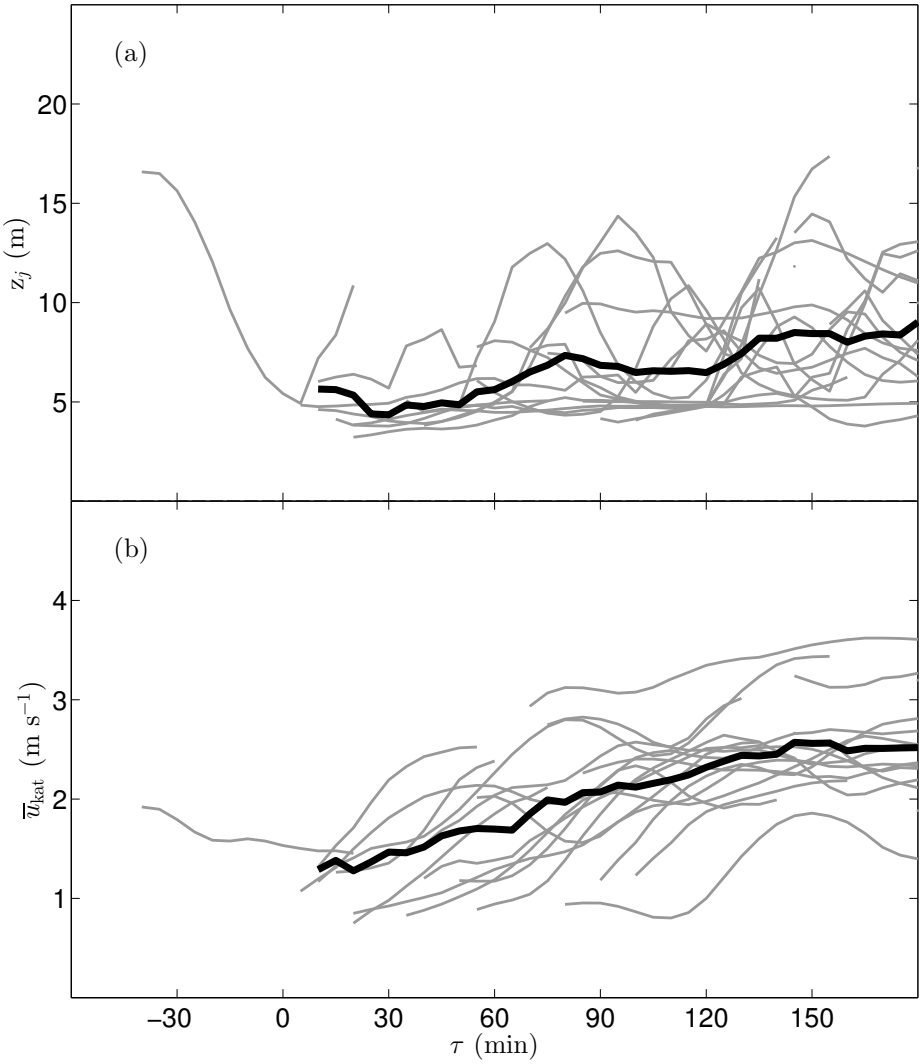

Figure 3.6: Evolution of the katabatic jet height (a) and veloctiy (b) at ES5 through the ET. Individual ETs are shown in gray and the black line is the mean evolution. A 25-min running average is applied to smooth the data. Gaps in the time series from individual ETs indicate that either the 10-m velocity was not directed downslope (±45°) or that a sign change in the momentum flux was not observed. The point where the time series begins indicates τ_{kat} for the given ET

their duration within individual ET time series increases with downslope distance, indicating that valley disturbances increase in frequency with downslope distance.

Finally, the ensembled, along-slope wind velocity time series for all tower levels and all ETs at ES5 and ES4 is given in Fig. 3.7. Note that it is not requisite that the point in the mean time series where $\overline{u}_{10\ \mathrm{m}} = 0$ be equal to τ_{kat} reported in Table 3.2, though at ES5 and ES4, the agreement is close. Rather, we include Fig. 3.7 to illustrate that on the mean, the katabatic flow deepens gradually over the height of the tower and nearly 30 minutes elapse from the point that the katabatic flow initializes at 0.5 m to the point of initialization at 20 m with the 10-m onset occurring approximately midway between the two. Thus, when the ensembled flow field is considered, the katabatic onset occurs very near the surface and the flow gradually deepens. This behavior is difficult to consistently observe on individual ETs due to fluctuations in the near-surface flow field. From Fig. 3.7, it is also evident that the maximum anabatic wind speed occurs at a height of greater than 10 m while the maximum katabatic velocity is observed on the 5-m anemometer, consistent with Table 3.2.

3.3.3 Momentum and Temperature Budgets

As an introduction to this section, the two-dimensional simplified budgets of slope-aligned momentum and potential temperature are briefly reviewed (Manins and Sawford, 1979a). The slope-parallel momentum budget is

$$\underbrace{\frac{\partial \overline{u}}{\partial t}}_{\mathrm{I}} = -\underbrace{\overline{u}\frac{\partial \overline{u}}{\partial s}}_{\mathrm{II}} - \underbrace{\overline{w}\frac{\partial \overline{u}}{\partial n}}_{\mathrm{III}} - \underbrace{\frac{1}{\rho_{\mathrm{a}}}\frac{\partial (p - p_a)}{\partial s}}_{\mathrm{IV}} - \underbrace{\frac{\partial \overline{u'w'}}{\partial n}}_{\mathrm{V}} - \underbrace{g\frac{\overline{d}}{\theta_0}\sin\beta}_{\mathrm{VI}}, \tag{3.1}$$

and the slope-parallel potential temperature budget is

$$\underbrace{\frac{\partial \theta}{\partial t}}_{\mathrm{I}} = -\underbrace{\overline{u}\frac{\partial \theta}{\partial s}}_{\mathrm{II}} + \underbrace{\overline{w}\frac{\partial \theta}{\partial n}}_{\mathrm{III}} - \underbrace{\frac{1}{\rho_{\mathrm{a}} c_p}\frac{\partial R_n}{\partial n}}_{\mathrm{IV}} - \underbrace{\frac{\partial \overline{w'\theta'}}{\partial n}}_{\mathrm{V}}, \tag{3.2}$$

where s and n are the downslope and slope-normal coordinates, respectively, ρ_{a} is the unperturbed reference air density, p is the local air pressure, p_a is the ambient air pressure, g is gravitational acceleration, β is the local slope angle, d is the temperature deficit defined as the difference between the local air potential temperature (θ) and

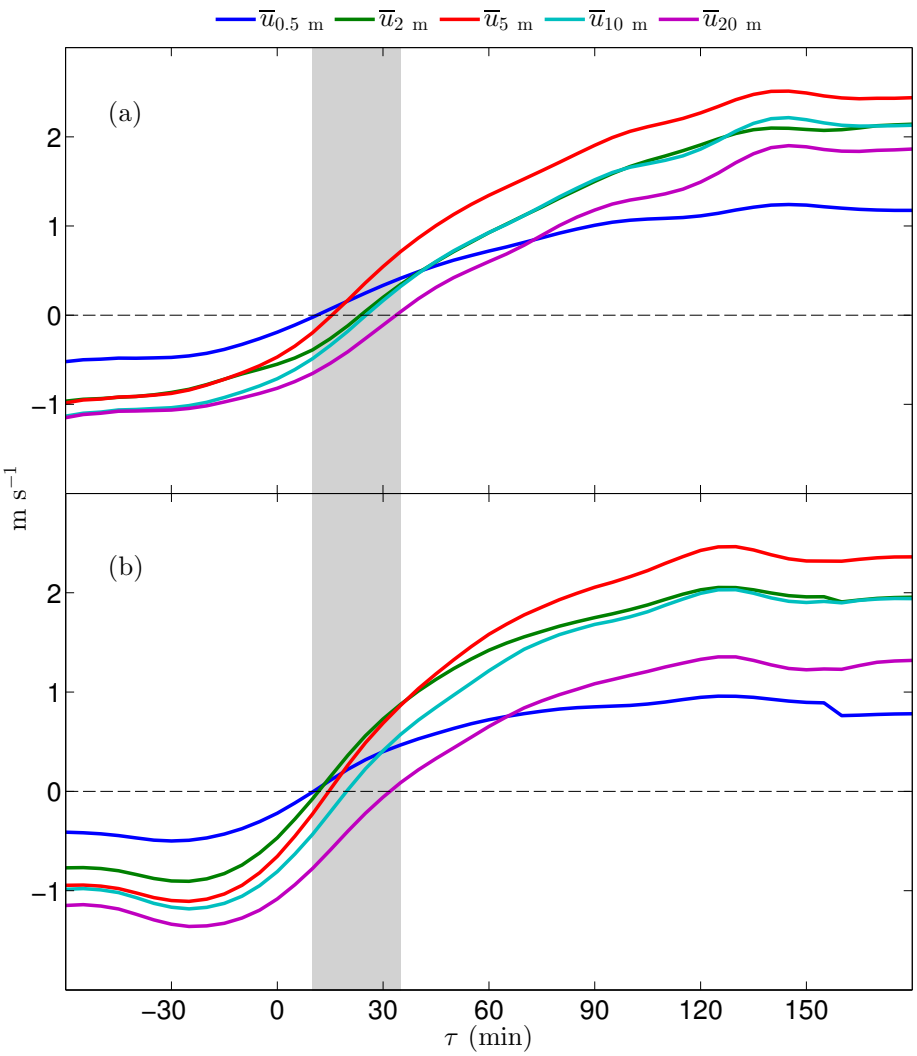

Figure 3.7: Composite time series of the tower velocities at ES5 (a) and ES4 (b). Negative (Positive) velocities indicate upslope (downslope) flow. The gray shading indicates the range of the katabatic onset, identified here as the velocity sign change in the emsembled time series, over all tower levels and is identical at ES5 and ES4.

the unperturbed potential temperature (θ_{a}), c_p is the specific heat capacity of air and R_n is net radiation. Terms I–III are the storage, slope-parallel advection and slope-normal advection of momentum (Eq. 3.1) and heat (Eq. 3.2), respectively. In Eq. 3.1, term IV is the along-slope pressure gradient and in Eq. 3.2, term IV is the net-radiative heat flux divergence. Term V is the divergence of momentum flux and sensible heat flux in Eqs. 3.1 and 3.2, respectively. Finally, term VI in Eq. 3.1 is buoyancy acceleration.

The composite time series of the terms in Eqs. 3.1 and 3.2 at the ES5 2-m level are reported in Fig. 3.8. Due to uncertainty in $\overline{w}$, the slope-normal advection terms and residual terms (slope-parallel pressure gradient and radiative heat-flux divergence) are omitted. In panel (a), the most apparent force balance is between buoyancy (term VI) and friction (term V). The anabatic inertia (term II) is relatively insignificant. In the temperature budget (Fig. 3.8 (b)), the maximum cooling rate occurs at local sunset and is driven by the sensible heat flux divergence, which begins to cool the layer while the mean sensible heat flux is still directed away from the surface. Later into the ET, slope-parallel advection also significantly cools the layer. This is contrary to the observations of Nadeau et al. (2013), where along-slope advection warms the layer. The difference is due to the direction of the shadow front propagation. Here, the shadow front propagates downslope, while in Nadeau et al. (2013), the shadow propagates upslope. Though not directly observed, it is expected that radiative flux divergence (term V) also cools the layer and vertical advection (term III) of warm air (through entrainment) warms the layer and consequently brings the budget into approximate balance. The 2-m velocity begins accelerating at $\tau \approx -30$ min and continues until $\tau \approx 120$ min. Prior to τ_{kat}, a positive acceleration in $\overline{u}$ may be viewed as a deceleration in the anabatic velocity.

Following Mahrt (1982), the Froude number, $Fr = \frac{U_{\mathrm{kat}}^2}{g\frac{-\overline{d}}{\overline{\theta}_a} Z_{\mathrm{inv}}}$, can be used to characterize the katabatic flow as either shooting ($Fr > 1$) or tranquil ($Fr < 1$) flow, where U_{kat} is the average katabatic velocity in the layer and Z_{inv} is the depth of the katabatic layer. Taking typical values observed early (late) in the ET at ES5 of $U_{\mathrm{kat}} = 0.5$ (1.5) m s^{-1}, $\theta_a = 294$ (291) K, $\overline{d} = 1$ (2) K and $Z_{\mathrm{inv}} = 20$ (30) m yields $Fr = 0.37$ (1.11), indicating that early in the transition, the flow is tranquil and later into the ET, the

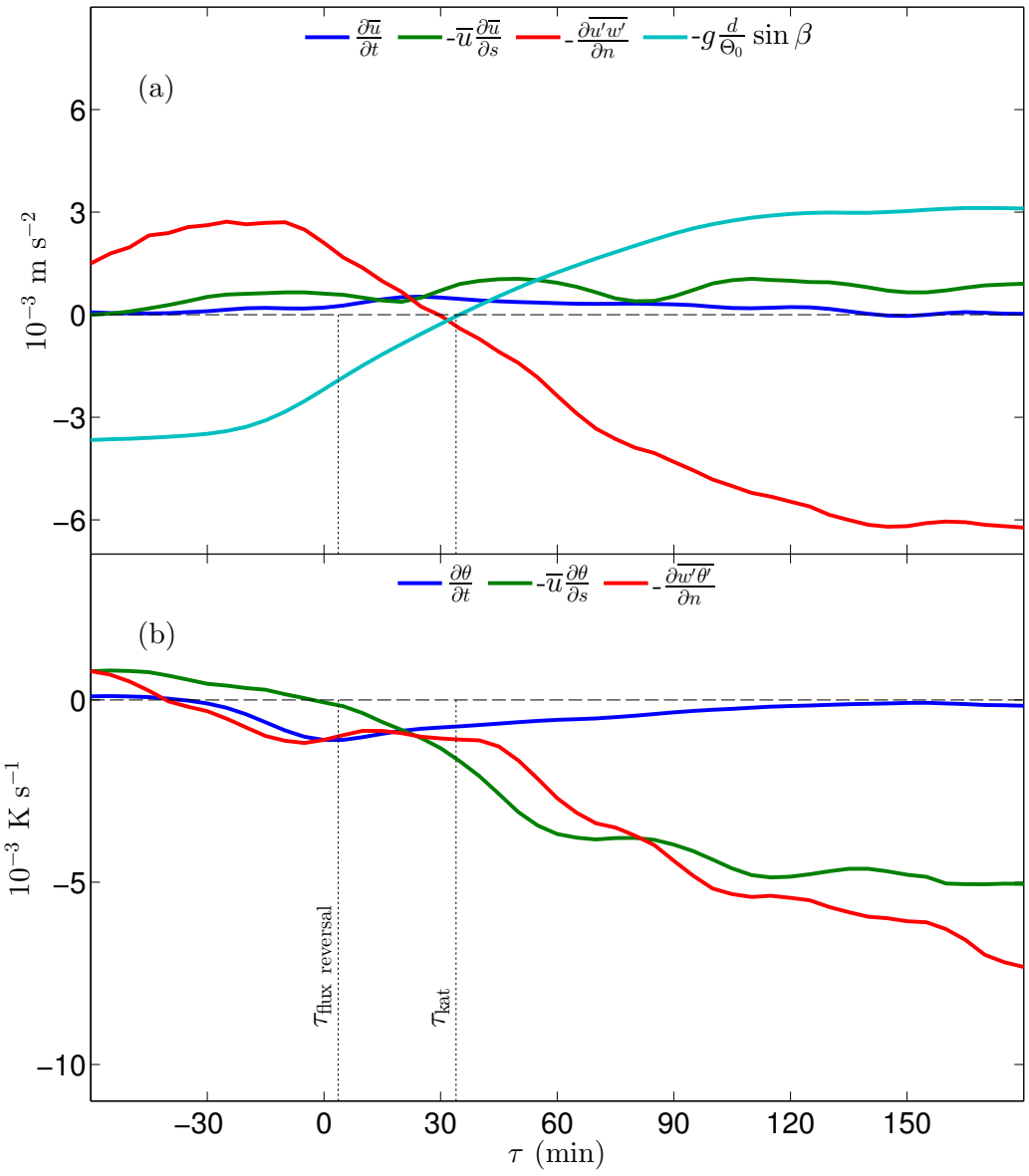

Figure 3.8: Composite time series of the momentum budget (a) and temperature budget (b) at the ES5 2-m level. The mean relative time of the sensible-heat flux reversal (τ_{flux}) and katabatic onset are indicated in the figure. Slope parallel gradients are computed with forward differencing between the 2-m levels at ES5 and ES4, and the slope-normal gradients are computed with forward differencing between the 2 and 5-m levels. The temperature deficit is computed as the difference in potential temperature between the 2 and 20-m levels. A 25-min running average is applied to smooth the data. The terms a plotted such that values greater (less) than 0 increase (decrease) momentum (a) and heat storage (b).

flow transitions to shooting. Lower on the slope, $\overline{d}$ is typically several degrees larger, indicating that flow is tranquil on the lower slope throughout the ET.

From Fig. 3.8, several time scales can be identified. The time scales are illustrated schematically in Fig. 3.9. First, the sensible-heat flux reversal occurs just after sunset at $\tau_{\text{kat}} \approx 4$ min. Just after the the heat flux reversal, the 2-m temperature gradient changes sign, allowing for short periods where the 2-m heat flux is countergradient (Blay-Carreras et al., 2014; Jensen et al., 2016). At approximately the same time, the along-slope temperature advection (term 2) changes sign. After the heating "cutoff", t_{frict} is the period where the residual anabatic flow is predominantly arrested by friction. This period is the evening decay period described in Hunt et al. (2003). However, on the east slope, the duration of the period is typically much shorter (< 20 min) than the 120 min estimate of Hunt et al. (2003) for a wide, shallow slope. This is consistent with the relatively weak residual anabatic inertia term (term II). Next, a 10 - 20 min calm period (t_{calm}) often, though not always, ensues. Near the end of the calm period, the temperature deficit changes sign (indicated by τ_{buoy}) and buoyancy begins to accelerate the katabatic flow with the onset ($\tau_{\text{kat}} \approx 34$ min) occurring shortly after τ_{buoy}. Finally, the katabatic flow accelerates until approximate equilibrium between buoyancy and friction is achieved at $\tau_{\text{eq}} \approx 120$ min.

With the exception of τ_{kat}, all time scales are computed here at a height of 2-m. It has been shown previously that τ_{flux} and τ_{buoy} are both functions of height (e.g. Caughey and Kaimal, 1977; Jensen et al., 2016). Also, when the composite time series of wind velocity is considered (Fig. 3.7), the definition of τ_{kat} becomes less restricted to allow τ_{kat} to become height dependent as well. Thus, with the exception of τ_{eq}, all time scales presented here are height dependent, though the general relative duration of the near-surface time scales (below the jet maximum) is consistent.

3.3.4 Katabatic Modeling

In this section, a simple katabatic model is developed to estimate the mean and interdiurnal variability observed in the katabatic flow. The model is based on the hydraulic approach derived in Manins and Sawford (1979a) (see Nappo and Rao (1987) for a review) along with the force balance proposed in Hunt et al. (2003). In

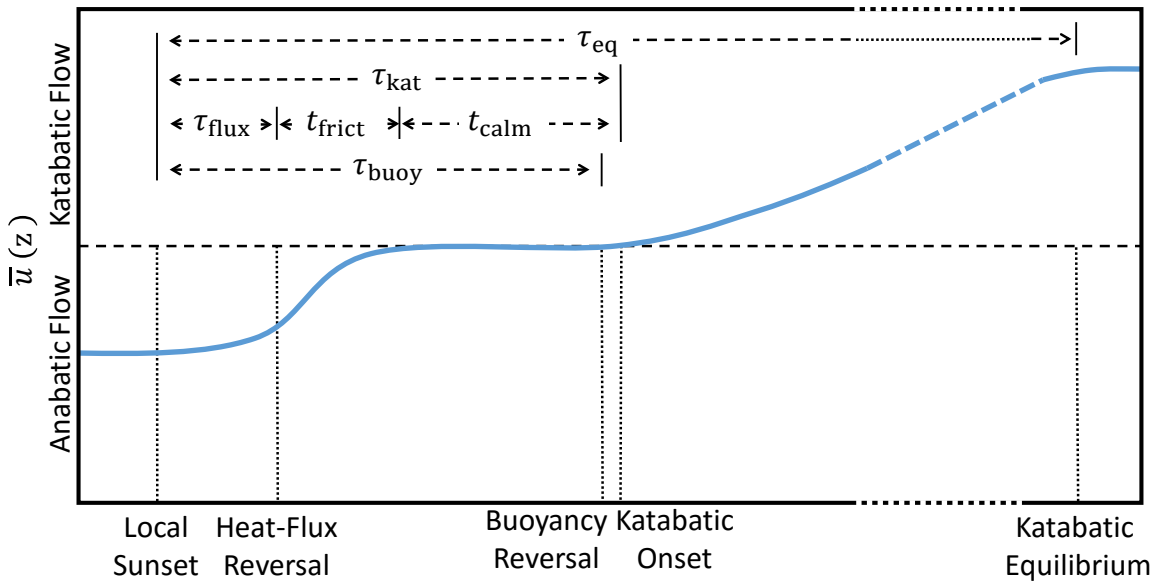

Figure 3.9: Schematic of an idealized velocity time series through the ET with accompanying time scales.

the hydraulic model, Eqs. 3.1 and 3.2 are integrated vertically to remove the vertical structure of the flow and derive characteristic variables describing the katabatic depth and velocity. The characteristic katabatic depth is given by

$$Z_{\mathrm{kat}} = C_1(\sin\beta)^{2/3}s, \tag{3.3}$$

and the characteristic katabatic velocity is

$$U_{\mathrm{kat}} = C_2(\sin\beta)^{2/9}\left(\frac{g}{\theta_{\mathrm{a}}}\overline{w'\theta'}_0\right)^{2/3}s^{-1/3}, \tag{3.4}$$

where C_1 and C_2 are constants, taken as $C_1 = 0.037$ and $C_2 = 2.15$ (Briggs, 1981), and s is the downslope distance from the top of the slope. *Note that Z_{kat} and U_{kat} are integrated quantities and cannot be directly compared with the observations of z_{j} and $\overline{u}_{\mathrm{kat}}$.*

Next, neglecting friction effects (Hunt et al., 2003), the katabatic onset is estimated to occur from a force balance of the slope-parallel momentum budget (Eq. 3.1) given by

$$g\frac{\overline{d}}{\theta_{\mathrm{a}}}\sin\beta \approx \overline{u}\frac{\partial\overline{u}}{\partial s}. \tag{3.5}$$

However, from Fig 3.8, it was observed that the residual anabatic flow was typically relatively insignificant and the relevant force balance was between buoyancy and friction. Given that friction acts on the flow proportional to its velocity, it is expected that friction will have little impact in delaying the onset of the katabatic flow. Thus, the RHS of Eq. 3.5 is insignificant and the katabatic onset occurs at approximately the same time that the temperature deficit passes through zero, allowing Eq. 3.5 to be further simplified to

$$\tau_{\mathrm{kat}} \approx \tau_{\mathrm{buoy}}. \tag{3.6}$$

This indicates that the katabatic onset is expected to occur in consonance with the sign change of the temperature deficit.

Next, from Manins and Sawford (1979a), the temperature deficit may be estimated by

$$\overline{d} = C_3(\sin\beta)^{-8/9}\overline{w'\theta'}_0^{2/3}\theta_{\mathrm{a}}^{1/3}(sg)^{-1/3}, \tag{3.7}$$

where $C_3 = 12.6$ is a constant (Briggs, 1981).

Equations 3.3, 3.4 and 3.6 represent a simple katabatic model that can be used to estimate the katabatic height, velocity and onset with the only required inputs being slope angle, sensible heat flux, temperature deficit and a reference temperature.

In the following subsections, the model is evaluated twice, first with observations of the sensible heat flux and temperature deficit (Sect 3.3.4.1), and second with the sensible heat flux modeled from the energy balance and the temperature deficit computed from Eq. 3.7 (Sect. 3.3.4.2). The results of both runs are presented in Sect. 3.3.4.3. The model is evaluated at the ES5 site only. This is done for simplicity in the presentation of the results as well as because ES5 lies in the upper portion of the slope and is assumed to agree most strongly with existing theory. Because the characteristic katabatic height depends only on slope angle and downslope distance, the result of $Z_{\mathrm{kat,\ ES5}} = 8.8$ m is constant and therefore not included in the discussion.

3.3.4.1 Observationally-Based (OB) Model

The first method we present will be referred to as the OB model. Observations of the 5-min sensible heat flux with an applied 25-min running average are used to drive the model. Eq. 3.4 and 3.7 take the surface sensible heat flux ($\overline{w'\theta'_0}$) as input. However, the lowest observation was recorded at 0.5 m and is influenced by canopy effects. Additionally, at all levels, the sensible heat flux is influenced to varying degrees by the along-slope wind system (Grachev et al., 2016). To overcome this and further limit signal noise, the input sensible heat flux is taken as the average sensible heat flux observed over all tower levels.

Next, assuming $\overline{\theta}_{20\mathrm{m}} \approx \overline{\theta}_{\mathrm{a}}$ and $\overline{\theta}_{0.5\ \mathrm{m}} \approx \overline{\theta}_0$, the temperature deficit is calculated from observations by

$$\overline{d} = \overline{\theta}_{0.5\mathrm{m}} - \overline{\theta}_{20\mathrm{m}}. \tag{3.8}$$

While this is the most direct method of modeling the katabatic flow with Eqs. 3.3, 3.4 and 3.6, it has the disadvantage of requiring *in situ* flux observations and temperature profiles, meaning that the katabatic characteristics could just as easily be observed directly. Therefore, it is used predominantly as a validation.

3.3.4.2 Energy-Balance (EB) Model

The second method, referred to as the EB model, utilizes much more easily obtained variables and models the sensible heat flux and temperature deficit by means of the surface energy balance using a variant of the Penman-Monteith method (Allen, 1998). The method assumes horizontal homogeneity, quasi-steady conditions, no advection and no thermal inertia. Every variable, with exception of the 2-m wind speed, necessary to run the second method is measured by the LEMS and is also a standard variable in most weather models. Since the MATERHORN campaigns, a 2-m wind speed has been added to the most recent version of the LEMS. The flow chart for the second method is shown in Table 3.3.

The first step in the EB model requires that the soil properties be estimated as a function of soil moisture. The modeled and observed soil properties are shown in Fig. 3.10. Though the albedo parametrization, described in Idso and Jackson (1975), was derived to use surface soil moisture as an input, the model performs well with $VWC_{50\ \mathrm{mm}}$ as the input. Also, the parameterization for the soil volumetric heat capacity (C_v) shows remarkable agreement with observations. As will be further discussed in Sect. 3.3.5.1, the K_soil parameterization of McCumber and Pielke (1981) substantially overestimates the sensitivity of K_soil to soil moisture (Massey et al., 2014). Therefore, we use a linear regression of our data to model K_soil.

The second step in the EB model is the computation of the net-longwave radiation (LW_N). Eq. 39 in Allen (1998) may be used to estimate the mean value throughout the day. LW_N can then be calculated at smaller time steps using outgoing longwave radiation ($LW_\uparrow$) from the Stefan-Boltzmann law and the assumption that the incoming longwave ($LW_\downarrow$) radiation is approximately constant over the day. The difficulty with this method is that knowledge of the cloud cover is necessary. Given that we are most interested in modeling the SEB through the ET, when the fluxes are small, relatively small errors can dramatically reduce the performance of the model. Thus, we rely on observations of the incoming longwave radiation.

The third step of the OB model is the computation of the surface energy budget. The ground heat flux (H_G) is computed as the sum of the heat flux estimated at a depth of 50 mm from the vertical temperature gradient, computed from T_G at the

Table 3.3: Process of the EB model. The bolded inputs are necessary observations to run the model. The OB model begins at step 4 with direct observations of H and $\overline{d}$.

Model Input	**Model Output**	**Reference**
1. Soil Properties		
$\boldsymbol{VWC_{50mm}}$	a	Idso and Jackson (1975)
$\boldsymbol{VWC_{50mm}}$	C_{V}	Moene and van Dam (2014)
$\boldsymbol{VWC_{50mm}}$	K_{soil}	McCumber and Pielke (1981)
2. Net Radiation		
Long, Lat, t	$SW_{\downarrow}$	Whiteman and Allwine (1986)
$\boldsymbol{T_0}$	$LW_{\uparrow}$	Stefan-Boltzmann law
$\boldsymbol{LW_{\downarrow}}$,$LW_{\uparrow}$, $SW_{\downarrow}$, a	R_N	Radiation Balance
3. Surface Energy Budget		
C_{V}, K_{soil}, $\boldsymbol{T_0}$, $\boldsymbol{T_{G,\ 50mm}}$, $\boldsymbol{T_{G,\ 250mm}}$	H_{G}	Bailey et al. (2016)
R_N, H_{G}, $\boldsymbol{\overline{u}_{2m}}$ $\boldsymbol{RH_{2m}}$, $\boldsymbol{T_{2m}}$, $\boldsymbol{P}$	H, H_{L}	Allen (1998)
4. Katabatic Characterization		
β, s	Z_{kat}	Eq. 3.3
H, β, θ_{a}, s	U	Eq. 3.4
$\overline{d}$	τ_{kat}	Eq. 3.5

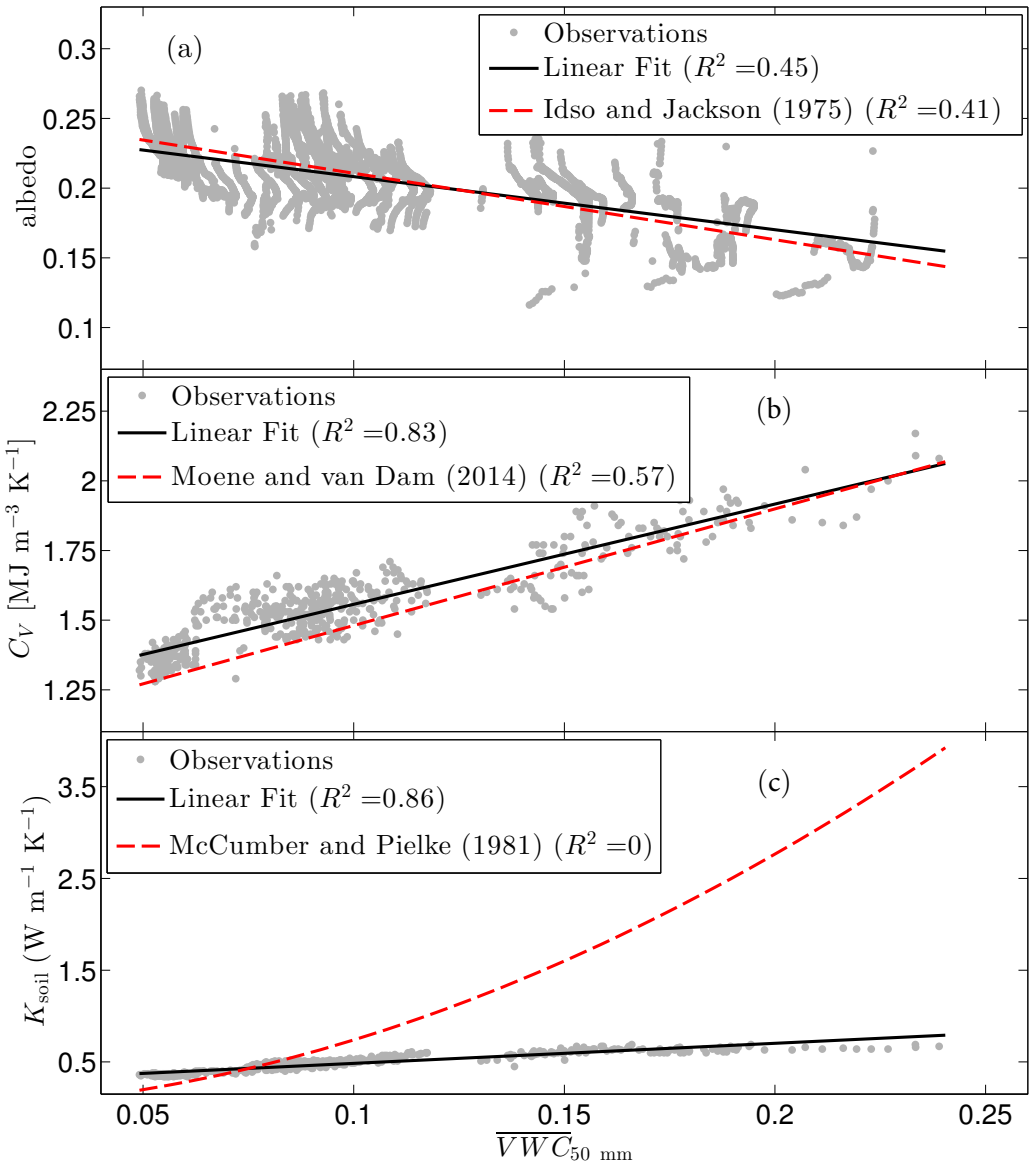

Figure 3.10: Parameterizations and observations of (a) albedo, (b) soil volumetric heat capacity and (c) soil thermal conductivity vs. the volumetric water content at 50 mm. Since the McCumber and Pielke (1981) performs poorly, the EB model uses the linear fit to calculate K_{soil} as a function of VWC. The fit is given by $K_{\text{soil}} = 2.2\overline{VWC}_{50\ \text{mm}} + 0.27$.

surface, 50 mm and 250 mm, and the storage term estimated from the temporal temperature gradient evaluated at 50 mm (Eq. A.2 in Bailey et al., 2016). The latent heat flux (H_{L}) is then calculated using the FAO Penman-Monteith equation (Eq. 53 in Allen, 1998), with an assumed crop coefficient of 0.25 which was estimated from Fig. 23 in Allen (1998) (see Steinwand et al., 2001, for additional discussion). Finally, the sensible heat flux (H) is calculated from the energy balance.

Figure 3.11 (a) gives a sample of the modeled and observed energy balance for 8 Oct 2012. In general, the agreement is quite good. The shadow front is well captured and the ground heat-flux observations and model closely agree. The model forces a closure of the energy budget and reports larger latent and sensible heat fluxes than what is observed from the 5-min eddy-covariance observations. In Fig. 3.11 (b), sample time series of the buoyancy term through the ET, also for 8 Oct 2012, are given. $\overline{d}$ computed from Eq. 3.7 with H_{OB} is only used as a validation of Eq. 3.7 and is not used in either katabatic model. In general, both methods agree reasonably well with observations, with the EB model slightly overestimating the magnitude of $\overline{d}$ and also decaying too abruptly. This is due to the shortcoming of the EB method where the model is unable to gradually respond to abrupt changes in external forcing. For example, the shortwave heating at the surface cuts off abruptly due to the passing shadow front. In reality, the temperature gradients, sensible heat flux and net radiation all respond over the course of minutes to hours (Blay-Carreras et al., 2014; Jensen et al., 2016). This is overcome to an extent by applying a running average to the modeled sensible heat flux but the model still has the most difficulty with the ET.

3.3.4.3 Katabatic Model Results

In Fig. 3.12, the results of the OB and EB models are presented. Both models perform adequately in certain circumstances and poorly in others. Fig. 3.12 (a) shows the skill of the models in predicting τ_{kat}. The outstanding performance of the OB model in estimating τ_{kat} is surprising. As expected from Fig. 3.8 (a), the katabatic flow typically initiates very near the time of the near-surface stabilization (when $\overline{d}$ changes sign). The bias is slightly negative, indicating that in reality, the katabatic

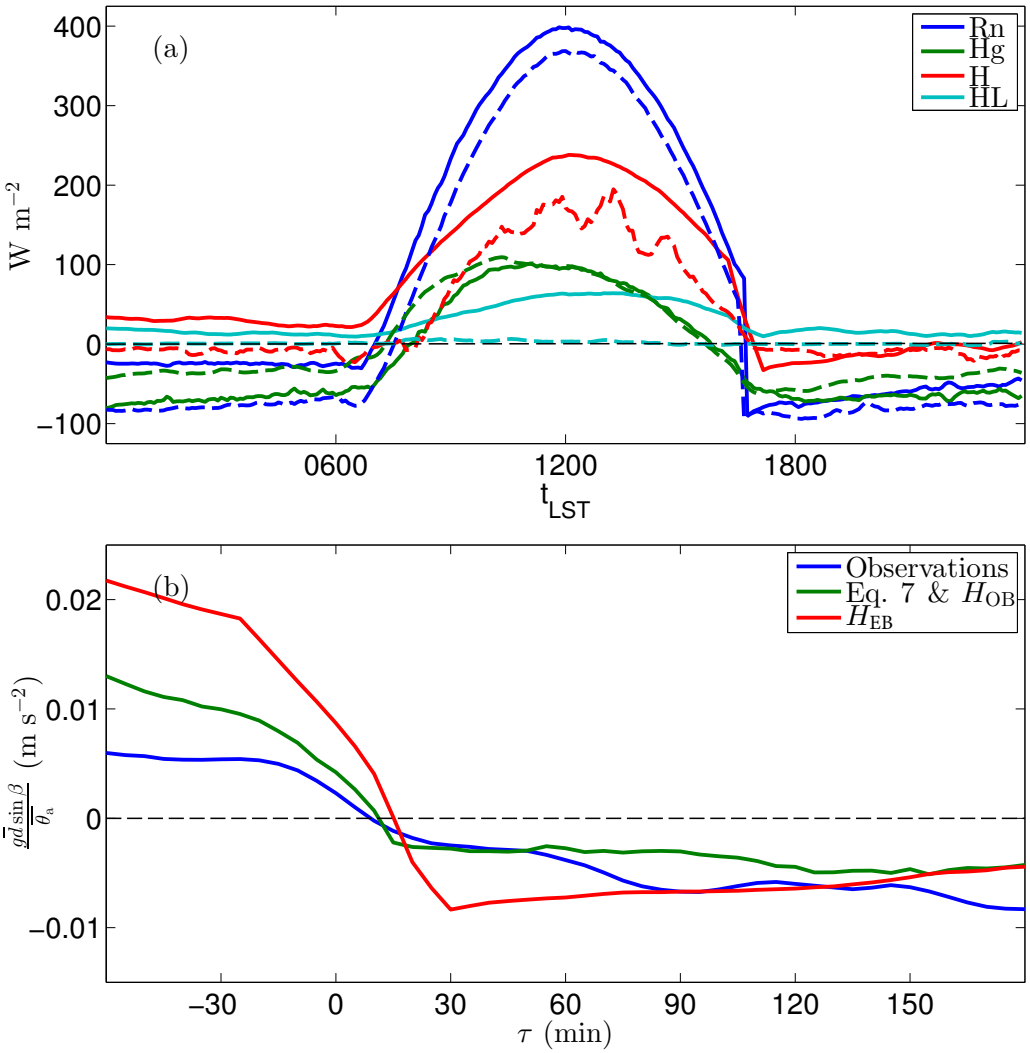

Figure 3.11: (a) Modeled energy balance on 8 Oct 2012 at ES5. A 45-min running average is applied to smooth the data. Observations are shown as dashed lines and the model is indicated by solid lines. (b) Sample time series of the buoyancy term through the ET from direct observations of d and Eq. 3.7 with H_{OB} and H_{EB} as inputs. Note that $\overline{d}$ computed from Eq. 3.7 with H_{OB} is not used to model the katabatic flow, it is only shown here as a validation.

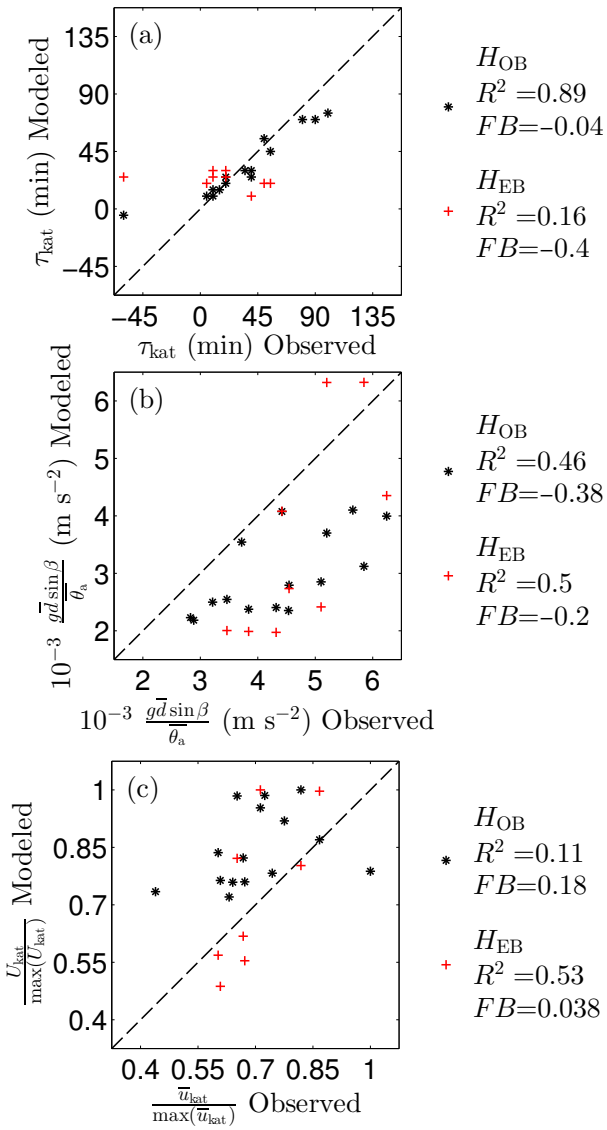

Figure 3.12: Results of both the OB and EB katabatic models at ES5 with the coefficient of determination (R^2) and fractional bias, defined as $FB = -2(\overline{C_O} - \overline{C_P})/(\overline{C_O} + \overline{C_P})$, where C_O is the observed value and C_P is the predicted value, indicated in the legend. Note that the OB model has more data points because the EB model was limited by available soil temperature data. The katabatic initialization estimated from Eq. 3.5 is shown in (a), the buoyancy term estimated from Eq. 3.7 is shown in (b) and the normalized katabatic velocities computed from Eq. 3.4 are shown in (c). Note that the modeled (U_{kat}) and observed ($\overline{u}_{kat}$) katabatic velocities are both normalized by their maximum values to allow for a comparison between the two variables. The maximum values are $\max(\overline{u}_{kat}) = 2.96$, $\max(U_{kat,\ OB}) = 0.95$ and $\max(U_{kat,\ EB}) = 1.19$ m s^{-1}. Also, a single outlier in the EB model was removed from the analysis.

onset occurs a short period after the sign change in $\overline{d}$. We conclude that for shallow slopes similar to the east slope, the onset of the katabatic flow may then be estimated to occur with or just after the reversal of the near-surface bulk temperature gradient (calculated here between $\approx$ 0.5 – 20 m). Given that the EB model most poorly estimates the heat fluxes near local sunset (Fig. 3.11 (b)), it is no surprise that τ_{kat} is poorly estimated by the EB model.

Next, in Fig. 3.12 (b), the parameterization of the buoyancy term is evaluated. Again, $\overline{d}$ from Eq. 3.7 with H_{OB} was not used to model τ_{kat} nor U_{kat}, but only as a validation of Eq. 3.7. Surprisingly, the buoyancy term modeled by Eq. 3.7 with H_{EB} performs better than the buoyancy term computed from Eq. 3.7 with H_{OB}; this is possibly due to the inability of the 5-min eddy-covariance to capture all of the downward sensible heat flux.

Finally, Fig. 3.12 (c) illustrates the model performance of the katabatic velocity. Because the observed katabatic velocity, $\overline{u}_{\mathrm{kat}}$, is the velocity of the katabatic jet and the modeled katabatic velocity, U_{kat}, is the integrated, characteristic katabatic velocity (Eq. 3.4), they cannot be directly compared. The observed katabatic profiles could be integrated over the height of the tower, but this is only valid if the height of the katabatic profile is smaller than the height of the tower, which is not the case through most of the ET (Fig. 3.5). To overcome this, the two velocities have been normalized by their maximum values (indicated in the figure caption). Again, the EB model outperforms the OB, and is able to capture the observed interdiurnal variability observed in the katabatic velocity, while the OB model cannot. Though one outlying point was omitted from the EB model, it more accurately estimates U_{kat} than the OB model.

Of the three katabatic variables compared, it is interesting that the EB model more accurately estimates the temperature deficit and katabatic velocity. The EB model could be further improved by including observations of the near-surface temperature gradient and then estimating the katabatic onset from the gradient reversal. In this way, the EB model could accurately estimate the katabatic onset and strength with only easily obtained variables as inputs.

The shortcoming of both models, in terms of the study objectives, is that they

are only able to account for the interdiurnal katabatic variance inasmuch as the meteorological and slope conditions governing the variance manifest themselves in the observed/modeled sensible heat flux and, in the OB model, the observed temperature deficit. Of the many external influences expected to affect the katabatic flow, this is not necessarily the case. Additionally, the models are unable to identify and quantify the specific influences affecting the flow. This is overcome statistically in the next section.

3.3.5 Statistical Modeling

In an effort to understand the sources of the interdiurnal katabatic variability, statistical analysis is used, first, with univariate, and second, with multivariate analysis. The objective of this section is to quantify the influence of external variables affecting the katabatic flow.

3.3.5.1 Univariate Analysis

Here, univariate analysis is utilized to investigate the dependence of $\overline{u}_{\mathrm{kat}}$, z_{j}, τ_{kat}, S_{KF} on observable external influences. The four katabatic variables are outcome variables assumed to be an unknown function of the observable, external predictor variables describing the slope. The relationship between the outcome variables and over 25 predictor variables were evaluated first quantitatively, and second, qualitatively. The predictor variables were selected by considering all observed variables that could potentially influence the katabatic flow dynamics. The univariate correlations between a given predictor and outcome variable were evaluated quantitatively by both the coefficient of determination, R^2, and the Student's t-test, $P(H_0)$, where P is the probability of H_0 and H_0 is the null hypothesis stating that there is no relationship between the outcome and predictor variable. The minimum requirement was that $P(H_0) < 0.05$ and $R^2 > 0.1$ for the correlation computed from the data from all of the sites. The R^2 threshold was set quite low because the quality of fit varied, in some cases dramatically, from site to site. Next, the relationships were evaluated qualitatively by answering three questions. First, is the relationship meaningful at all sites, and if not, is there a likely explanation for the disparity or is it likely due to noise in the data? Second, is the phenomenon manifest in codependent predictor variables?

For example, the influence of soil moisture is observed via the albedo, Bowen Ratio, and $VWC_{50\ \mathrm{mm}}$. Third, is the relationship non-obvious? As an example of an obvious relationship, $\overline{u}_{\mathrm{kat}}$ at all sites is strongly correlated with the magnitude of the velocity at ES5 through the ET. Relationships that were found to be both statistically and qualitatively significant are reported in Fig 3.13 and Table 3.4. Fig. 3.13 gives a graphical example for each outcome variable and a single predictor variable. Table 3.4 describes the nature of the relationship for additional significant phenomena, including those reported in Fig 3.13.

The variables influencing the katabatic flow can be grouped into four broad categories of external influence. The categories are indicated by cell color in Table 3.4. Ambient winds are shaded green, the shadow front is shaded red, soil moisture is shaded blue and turbulence is shaded brown. In multiple cases, correlations between a katabatic outcome variable and several related predictor variables (e.g. soil thermal conductivity and VWC) were found to be significant. In Table 3.4, only the most strongly correlated predictor variable from a given group is reported.

As expected from previous work (Wagner, 1938; Horst and Doran, 1986; Whiteman, 2000; Savage et al., 2008), the katabatic flow is highly sensitive to ambient winds. In particular, the valley circulation, observed at Target R, is very indicative of the development and structure of the katabatic flow. The Target R upvalley component is the most highly correlated variable for $\overline{u}_{\mathrm{kat}}$ and S_{KF} and the upslope component also shows significant correlation with z_{j}. The sign of the correlations is negative, indicating that for ETs dominated by an active upvalley circulation, the katabatic flow is weakened, the katabatic front moves slower and the height of the katabatic jet is reduced. This finding is consistent with existing theory (Whiteman, 2000; Zardi and Whiteman, 2013), where areas dominated by strong up-valley circulations have weaker katabatic development. Note that the quality of fit for the correlations decreases with increased distance up the slope, indicating that the influence of the valley circulation is gradually dampened with upslope distance. Interestingly, the valley circulation, observed at Target R, shows little correlation with τ_{kat} and is not included in Table 3.4. Instead, the upvalley component observed at ES5 shows a much stronger correlation with τ_{kat}. The onset of the katabatic flow is delayed and

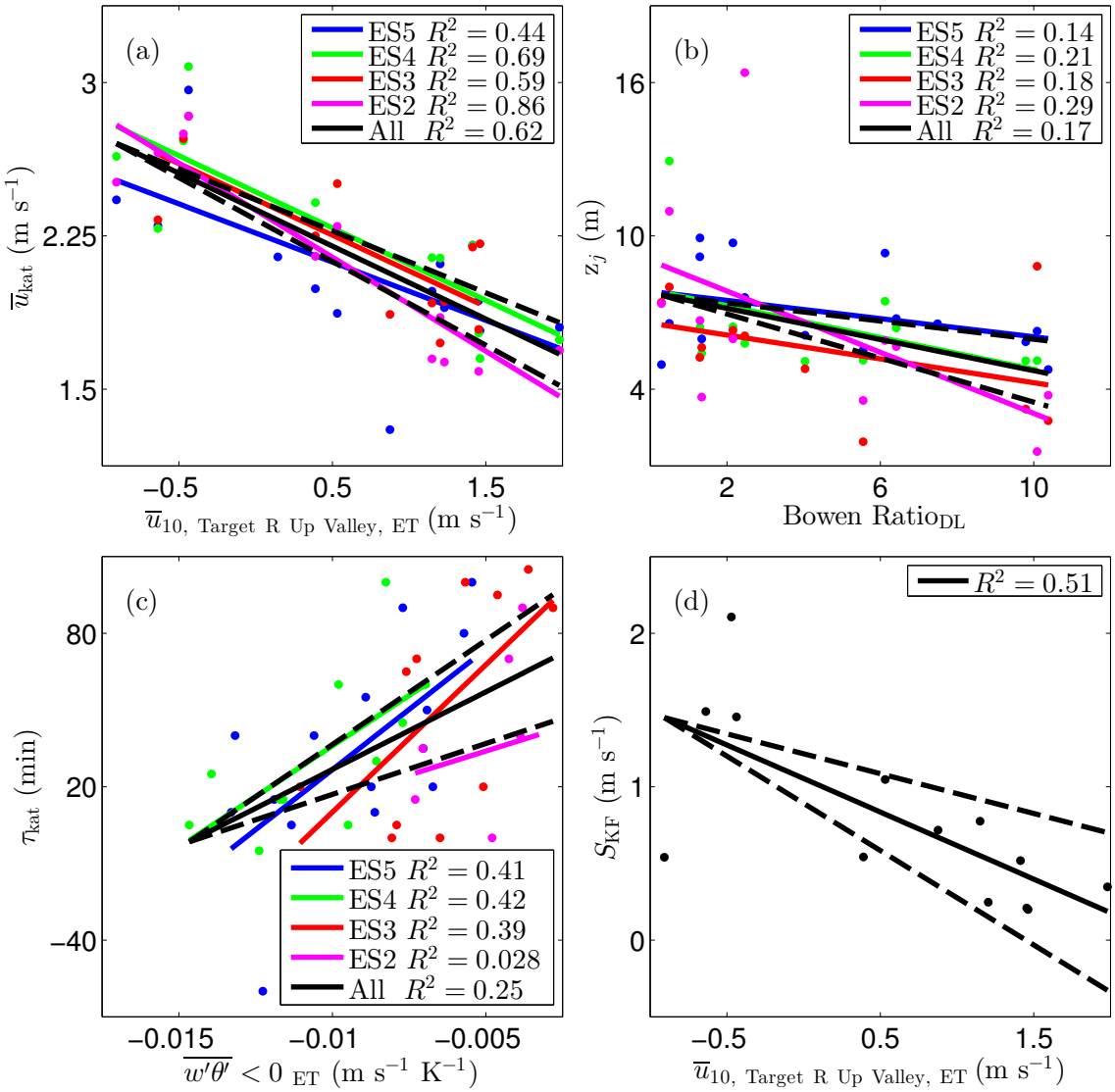

Figure 3.13: Sample univariate correlations for (a) the katabatic velocity vs. the up-valley wind component at the base of the slope through the ET, (b) the katabatic nose height vs. the observed daytime Bowen Ratio, (c) the katabatic onset vs. the mean downward sensible heat flux through the ET and (d) the katabatic front speed vs. the up-valley wind component at the base of the slope through the ET. Table 3.4 illustrates the correlations shown in this figure along with additional statistically significant correlations. The black line indicates a linear regression with data from all sites and the black dashed lines give the 90% confidence interval on the fitted slope.

Table 3.4: Statistically significant results of the univariate analysis. The katabatic variable is listed vertically and the external influence variables are listed horizontally in descending quality of fit. The shaded triangles describe the correlation in three ways. First, the direction of the triangle indicates the sign of the correlation, upward for positive and downward for negative. Second, the shading of the triangle is proportional to the coefficient of determination of the fit (R^2); note the colobar at the bottom of the table. Third, the relative size of the triangle is proportional to the magnitude of the slope of the linear fit. The relative triangle size for a given row is normalized by the slope with the highest magnitude within that row, thus comparisons of triangle size cannot be made between rows. Each predictor variable is placed into one of four groups of variables; the cell color indicates the group. The subscript $_{\text{ET}}$ denotes that the variable is averaged through the ET and $_{\text{DL}}$ indicates that the variable is averaged over daylight hours. The subscripts $_{\text{up valley}}$ and $_{\text{up slope}}$ are defined as positive for upward flow and negative for downward flow. *tke* is turbulence kinetic energy computed as the mean from all tower levels, $\overline{w'\theta'} < 0\ _{\text{ET}}$ is the mean negative sensible heat flux averaged over all tower levels. The Bowen Ratio is computed at all sites as the mean of the Bowen ratio observed at ES3 and ES5. With the exception of S_{SF}, all outcome variables are computed locally at each tower. The column labeled "All" gives the results of the linear fit computed with data from all sites.

z_j reduced proportionally to the strength of the upvalley winds observed at ES5 through the ET. In this way, the valley-aligned wind component at ES5 provides a measure of the extent to which valley winds penetrate the east slope. Finally, the katabatic front is observed to propagate downslope more quickly under high wind speeds at ES5. It is interesting that the correlation between S_{KF} and 10-m winds at ES5 is strongest for the magnitude of the velocity and not for the slope component.

The katabatic velocity and onset are both found to correlate with the shadow front speed. The correlation between $\overline{u}_{kat}$ and S_{SF} is relatively strong and consistent at all sites. The correlation is negative, meaning that for a fast moving shadow front, the katabatic wind speed is observed to be relatively low. Though the mechanism behind the correlation is not entirely clear, it is likely related to the strengthening buoyant force (term VI in Eq. 3.1) higher on the slope. For a slow-moving shadow front, radiative cooling is able to cool the surface high on the slope for a longer period of time, relative to a fast-moving shadow front. The increased surface cooling leads to a more strongly negative buoyancy force higher on the slope which is able to more rapidly accelerate the flow and increase the observed katabatic wind speed. Similarly, the increased buoyancy force allows the katabatic flow to begin earlier for slow-moving shadow fronts.

Next, the influence of soil moisture is considered. Though weaker than the correlation with ambient winds, soil moisture is observed to significantly correlate with the katabatic flow via the Bowen ratio, K_{soil}, $VWC_{50\ mm}$ and the surface albedo (only the Bowen ratio is included in Table 3.4). One of the objectives of this study is to experimentally evaluate the findings of Banta and Gannon (1995). Banta and Gannon (1995) identify several competing influences resulting from increased soil moisture. Banta and Gannon (1995) initially hypothesized that for arid conditions (no condensation), increased evaporative cooling should dominate and the katabatic flow should strengthen for increased soil moisture. After running the simulations, Banta and Gannon (1995) found that the increase of K_{soil}, from the increased soil moisture, is more important and allows for heat exchange with a deeper layer of soil and effectively reduces surface cooling and weakens the katabatic flow. They also noted a secondary effect of increased near-surface air moisture leading to stronger

downwelling longwave radiation, further reducing surface cooling. Considering that we are interested in the ET, we also consider that the residual anabatic flow may be weaker due to less sensible heating during the day (Ookouchi et al., 1984). This would allow for a stronger katabatic flow to develop earlier in the ET. We also speculate that the increased K_{soil} may lead to idealized mixing conditions, where the temperature gradient is optimized between driving potential (strength of gradient) and mixing conditions, maximizing the the sensible heat flux toward the surface and thereby strengthening term V in the momentum budget (Caughey et al., 1979). Unfortunately, we are unable to resolve this relationship with our data.

Contrary to the conclusions of Banta and Gannon (1995), we observe a positive correlation between the katabatic strength and soil moisture. The flow is observed to both accelerate and deepen for moist conditions. The correlation is weak at ES5 but stronger and more consistent at ES4–ES2. The competing influences were evaluated, but no clear correlations were identified. Given that ES5 is the site most sheltered from valley interaction and is the most "idealized" station, and also shows little to no correlation with soil moisture, we conclude that we are neither able to validate nor reject the findings of Banta and Gannon (1995). It should be noted that the simulations of Banta and Gannon (1995) utilized the thermal conductivity parameterization described in McCumber and Pielke (1981). Fig. 3.10 (c) shows the parameterization vs. observations at the east slope. The parametization dramatically overestimates the sensitivity of K_{soil} to soil moisture, something Banta and Gannon (1995) recognized as a possibility. This is likely partially responsible for the disparity between their simulations and our observations.

Finally, the influence of turbulence is discussed. The mean turbulence kinetic energy through all daylight hours and averaged over all tower levels (tke_{DL}) shows a strong correlation with jet height at ES2. The correlation is virtually nonexistent at the other sites. For highly turbulent days, z_{j} is much higher at ES2 (see Table 3.4), due to increased interaction with the valley turbulence. As discussed in the previous section, the variability of z_{j} at ES2 is much higher and tke_{DL} accounts for more than 80% of the observed variance (Table 3.4).

The onset of the katabatic flow, particularly at ES3 and ES5, is also observed

to correlate with tke_{DL}. The correlation is negative. That is, τ_{kat} is delayed with increasing magnitude of tke_{DL}. Conversely, τ_{kat} is positively correlated with the mean, negative sensible heat flux through the ET ($\overline{w'\theta'} < 0$ $_{\mathrm{ET}}$). Thus, when the magnitude $\overline{w'\theta'} < 0$ $_{\mathrm{ET}}$ is relatively large, the katabatic buoyant force is strengthened and the katatabic flow begins earlier (Fig. 3.13 (c)). This correlation is not clear at ES2 because of increased valley-flow interactions. Finally, we observe a strong correlation at ES5 between τ_{kat} and time relative to local sunset of the sensible heat flux sign change ($\tau_{\mathrm{flux\ reversal}}$). It is an intuitive result for near-equilibrium conditions, and also evident from Eq. 3.7, that when the sensible heat flux sign change occurs earlier in the ET, the katabatic onset also occurs earlier. This correlation is much stronger at ES5 than the other sites and indicates that ES5 is the most "idealized" site for classical katabatic development.

3.3.5.2 Multivariate Analysis

Because the katabatic variables show sensitivity to multiple external influences, multivariate analysis is also used. Here, a simple linear regression model with multivariate inputs is considered. Because of the expected correlation between many of the predictor variables, a simple multiple-linear regression is expected to perform poorly. Instead, partial least-squares (PLS, Rosipal and Krämer, 2006) regression is used. PLS is similar to principal component regression (PCR, Jolliffe, 2002) in that the input predictor variables are transformed into orthogonal components that are linear combinations of the original predictor variables. The number of components utilized in the PLS and PCR regressions is typically less than the original number of predictor variables. Because the components are orthogonal, PLS and PCR regressions are able to account for correlations in the original predictor variables. The difference between PLS and and PCR is that PCR only accounts for variance in the predictor variables with no consideration of the outcome variable. PLS accounts for both predictor and outcome variables and in many cases, including here, allows for a more accurate regression with fewer components necessary.

The weighting functions of the PLS regression can be examined to identify the predictive power of the individual predictor variables. The analysis in this study was

performed with plsregress.m, a function in the MATLAB® Statistics and Machine Learning Toolbox. In general, the PLS weighting agreed with the quantitative analysis of the univariate correlations discussed in the previous section. However, the weighting was unable to account for the qualitative analysis that was also performed. Also, the weighting showed significant variation from one site to another. Therefore, a PLS regression was developed with only the predictor variables that were observed to be significant both quantitatively and qualitatively. This regression is referred to as the "Complete" PLS regression because all significant predictors are included. Cross-validation, which helps to avoid over-fitting of the data and to create a more generalizable regression, was used to select the appropriate number of components for the PLS regression. Here, 5-fold cross-validation is used. The results indicated that three to five components is ideal at most sites, for most outcome variables. Therefore, four PLS components were used. The PLS regression, utilizing all significant predictors, showed strong correlations with all outcome variables. The mean reported R^2 values at all sites are 0.85, 0.74, 0.81, 0.75 for $\overline{u}_{\mathrm{kat}}$, z_{j}, τ_{kat} and S_{SF}, respectively.

Next, the number of predictor variables was further restricted to only include the valley wind component at Target R and ES5, shadow front speed and Bowen Ratio. This is referred to as the "Simple" PLS regression. In the Simple PLS regression, the predictor variables were limited to easily observed or modeled parameters, and all turbulent quantities were removed. Based on the results of cross-validation, the Simple PLS regression was run with four components. Fig. 3.14 gives the results of the Simple regression. In general, the katabatic flow is reasonably well described by the four predictor variables. Due to the omission of turbulence, $\tau_{\mathrm{kat}}$is poorly modeled at ES5 and z_{j} is somewhat poorly modeled at ES2. z_{j} at ES5 is also poorly represented by the regression, but this was also observed to be the case from the univariate analysis (see Table 3.4). We hypothesize that, to a reasonable level of accuracy, the katabatic dynamics over slopes similar to the east slope could be modeled with only the upvalley wind components observed near the base and higher on the slope, Bowen ratio and the shadow front speed. Though the Simple PLS regression is able to accurately model the katabatic flow over the east slope, it has the disadvantage that the regression must first be trained for a specific slope, which requires extensive instrumentation.

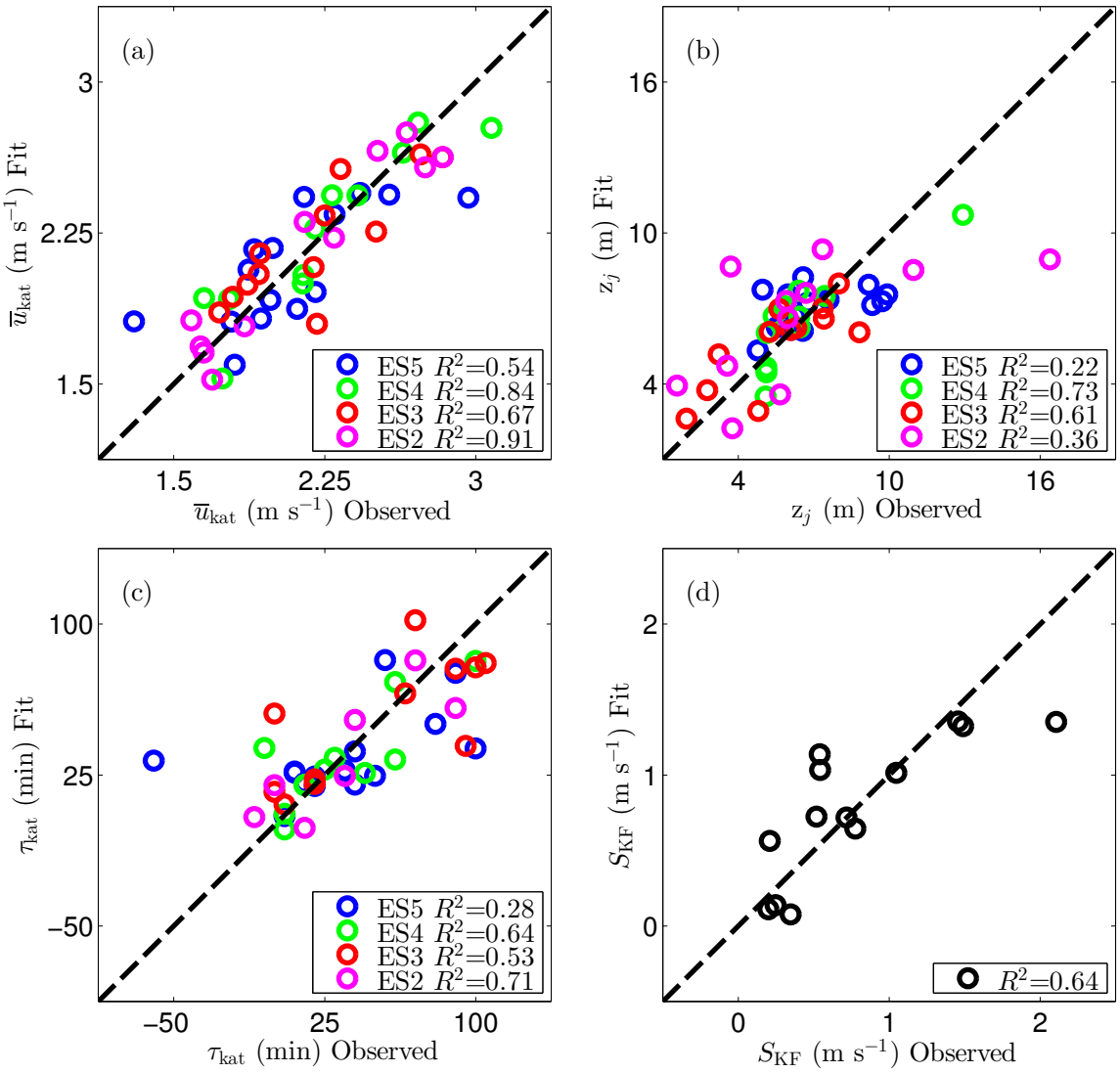

Figure 3.14: Results of the Simple PLS regression for the katabatic velocity (a), katabatic nose height (b), katabatic onset (c) and katabatic front speed (d). The simple PLS model takes the valley-wind component at ES5 and Target R, Bowen Ratio$_{\rm DL}$ and $S_{\rm SF}$ as inputs.

Nonetheless, we conclude that the upslope winds, Bowen ratio and shadow front speed are responsible for a significant portion of the interdiurnal variance observed over the east slope and the result is likely applicable to similar slopes.

The results of both regression models and the katabatic models, discussed in Sect. 3.3.4, are summarized in Table 3.5. The Complete PLS model performs much better than the other three models but has the significant shortcoming of requiring many observational inputs and needs to be trained specifically for a given slope. The Simple katabatic model reduces the number of required inputs to mean variables that are easily observed or modeled but still requires a site-specific training. Nonetheless, the model is valuable because it shows that a substantial portion of the interdiurnal variance can be diagnosed by valley winds, soil moisture and the shadow front. Given that turbulence is omitted, this is a surprising result and likely due to the "idealized" ETs considered in this study. The katabatic model using direct observations of the sensible heat flux and temperature deficit is able to very accurately estimate the onset of the katabatic flow but only shows modest skill in estimating the temperature deficit (computed from Eq. 3.7 with H_{OB} as an input) and almost no skill in estimating $\overline{u}_{\mathrm{kat}}$. Finally, the katabatic model utilizing the Penman-Monteith method requires only simple inputs and is broadly generalizable. The model is unable to accurately model the katabatic onset, due to the Penman-Monteith equation's inability to model inertial driving forces. Nonetheless, the model captures the general trend of both the katabatic velocity and temperature deficit.

3.4 Conclusions

The onset and structure of katabatic flow through the ET (taken in this study as 1 hr before to 3 hr after local sunset) is subject to a number of external influences that can dramatically change the katabatic properties from one day to the next. In this study, we have utilized the spatio-temporally unprecedented MATERHORN dataset to study both the mean and interdiurnal properties of the katabatic flow over a shallow, arid slope in Utah's West Desert. Fifteen exemplary transitions characterized by low synoptic activity and well-defined katabatic flow were used in the study. We began the discussion with a quantification of the mean statistics of the katabatic

Table 3.5: Review of the four katabatic models discussed in this study. In the OB Katabatic model, R^2 is reported for $\overline{d}$ computed from Eq. 3.7 with H_{OB}.

	Katabatic Models (Sect. 3.3.4) ES5 Only		**PLS Regression Models (Sect. 3.3.5)** All Sites	
	OB	EB	All Predictors	Simple Predictors
Model Inputs	H	$VWC_{50\ \mathrm{mm}}$	All Significant	Valley Wind (valley)
	d	$T_{\mathrm{G,\ 50mm}}$	Predictors	Valley Wind (slope)
		$T_{\mathrm{G,\ 250mm}}$	(see Table 3.4)	Bowen Ratio
		T_0		Shadow Front Speed
		$T_{2\mathrm{m}}$		
		$RH_{2\mathrm{m}}$		
		$LW\downarrow$		
		P		
Mean Model Coefficient of Determination (R^2)				
$\overline{u}_{\mathrm{kat}}$	0.11	0.53	0.85	0.74
z_{j}	-	-	0.74	0.48
τ_{kat}	0.89	0.16	0.81	0.54
S_{KF}	-	-	0.75	0.64
$\overline{d}$	0.46	0.50	-	-

flow through the ET. Next, the budgets of momentum and heat were examined and time scales identified. In Sect. 3.3.4, we used the hydraulic approach of (Manins and Sawford, 1979a) along with the Penman-Montheith method to develop a simple model for the katabatic timing and structure through the ET. The skill of the model was evaluated for both the mean and interdiurnal properties of the katabatic flow. Finally, the contributions of individual external influences were quantified with uni- and multivariate statistical analysis. The main conclusions of the study are:

- For individual ETs, the best definition for the katabatic onset is a 10-m wind velocity pointed downslope ±45° for a persistent duration; here, 30 min is used. It has the advantage of being simple, robust and a commonly available variable (Sect. 3.3.1). When composite data are analyzed (Fig. 3.7), this definition of τ_{kat} is unnecessary and it is observed that the katabatic onset begins low on the tower and gradually deepens to > 20 m over an ≈ 30 min period.

- The near-surface (below jet maximum) momentum budget (Eq. 3.1 and Fig. 3.8) is dominated by a force balance between friction and buoyancy, the residual anabatic flow is typically quite weak and arrested quickly after local sunset by friction. This allows for remarkably accurate estimates of τ_{kat} from observations of only the temperature deficit (Eq. 3.6 and Fig. 3.12).

- The peak cooling rate occurs near local sunset and is comparable in magnitude to the cooling from the sensible heat flux divergence (Eq. 3.2 and Fig. 3.8). Later in the ET, slope-parallel advection significantly cools the layer.

- From the budgets of momentum and temperature (Fig. 3.8), several time scales can be identified (Fig. 3.9). The katabatic onset (τ_{kat}) typically occurs at all sites ≈ 30 min after local sunset. The time between local sunset and τ_{kat} is broken into three subperiods. First, just after local sunset, the sensible heat flux changes sign and heating is "cut-off" to the near-surface air mass (τ_{flux}); next, friction arrests any residual anabatic flow (t_{frict}); this is followed by a calm period (t_{calm}) that persists until the katabatic onset. Near the end of the calm period, the near-surface air mass stabilizes and buoyancy begins to accelerate

the katabatic flow downslope at τ_{buoy}. The acceleration continues until $\tau_{\text{eq}} \approx 120$ min, at which point a force balance between friction and buoyancy is achieved and the flow is quasi steady.

- The hyrdraulic model of Manins and Sawford (1979a) combined with energy-balance modeling and the Penman-Monteith method (Allen, 1998) allow for simple modeling of the katabatic flow with easily obtainable variables. The model results (Fig 3.12) indicate that the interdiurnal katabatic variance is captured to a first order. The model is especially useful because it is broadly generalizeable to other slopes.

- From univariate analysis, four broad groups of external variables were found to influence the katabatic flow. First, persistent upvalley winds were found to decrease the katabatic flow velocity, jet height and katabatic front speed. Second, relatively fast-moving shadow fronts were found to correlate with slower katabatic velocities and delayed katabatic onsets. Third, turbulence was found to influence the jet height and the katabatic onset. Finally, contrary to the simulations of Banta and Gannon (1995), soil moisture was found to positively correlate with higher katabatic velocities and jet heights and faster katabatic front speeds. Though the reason for the disparity is not entirely clear, it likely related to the overly sensitive soil moisture parameterization of McCumber and Pielke (1981) utilized in the simulations.

- The results of the univariate analysis can be used in a partial-least squares (PLS) regression to more accurately model the katabatic outcome variable as a function of the external, predictor variables. Using only valley wind speed, Bowen Ratio and the shadow front speed, the PLS model is able to more accurately model the flow than the hydraulic/Penman-Monteith model (Sect. 3.3.4), though the PLS model has the significant shortcoming that it must be trained specifically for a slope. Nonetheless, the PLS regression shows that most of the interdiurnal katabatic variance may be diagnosed by only four external variables.

3.5 References

Allen, R. G., 1998: Crop evapotranspiration-Guidelines for computing crop water requirements-FAO Irrigation and drainage paper 56. *Irrig. Drain.*, **300**, 1–300.

Arritt, R. W. and R. A. Pielke, 1986: Interactions of nocturnal slope flows with ambient winds. *Boundary-Layer Meteorol.*, **37**, 183–195.

Bailey, B. N., R. Stoll, E. R. Pardyjak, and N. E. Miller, 2016: A new three-dimensional energy balance model for complex plant canopy geometries : Model development and improved validation strategies. *Agric. For. Meteorol.*, **218**, 146–160.

Banta, R. and W. Cotton, 1981: An analysis of the structure of local wind systems in a broad mountain basin. *J. Appl. Meteorol.*, **20**, 1255–1266.

Banta, R. M., L. S. Darby, J. D. Fast, J. O. Pinto, C. D. Whiteman, W. J. Shaw, and B. W. Orr, 2004: Nocturnal low-level jet in a mountain basin complex. Part I: Evolution and effects on local flows. *J. of Appl. Meteorol.*, **43**, 1348–1365.

Banta, R. M. and P. T. Gannon, 1995: Influence of soil moisture on simulations of katabatic flow. *Theor. Appl. Climatol.*, **52**, 85–94.

Barr, S. and M. M. Orgill, 1989: Influence of external meteorology on nocturnal valley drainage winds. *J. Appl. Meteorol.*, **28**, 497–517.

Blay-Carreras, E., E. R. Pardyjak, D. Pino, D. C. Alexander, F. Lohou, and M. Lothon, 2014: Countergradient heat flux observations during the evening transition period. *Atmos. Chem. Phys.*, **14**, 9077–9085.

Brazel, A., H. Fernando, J. Hunt, N. Selover, B. Nedquist, and E. Parkyjak, 2005: Evening transition observations in Phoenix, Arizona, USA. *J. Appl. Meteorol.*, **44**, 99–112.

Briggs, G., 1981: Canopy effects on predicted drainage flow characteristics and comparisons with observations. *Preprints, Fifth Sympos. on Turbulence, Diffusion and Air Pollution*, Amer. Meteorol. Soc: Boston. 113-115, Atlanta, GA, 113–115.

Brost, R. a. and J. C. Wyngaard, 1978: A model study of the stably stratified planetary boundary layer. *J. Atmos. Sci.*, **35**, 1427–1440.

Buettner, K. J. K. and N. Thyer, 1965: Valley winds in the mount Rainier area. *Arch. für Meteorol. Geophys. und Bioklimatologie Ser. B*, **14**, 125–147.

Campbell Sci., 2002: *Model HFP01SC Self-Calibrating Soil Heat Flux Plate Instruction Manual*. Campbell Scientific, Inc., 32 pp.

Caughey, S. J. and J. C. Kaimal, 1977: Vertical heat flux in the convective boundary layer. *Q. J. R. Meteorol. Soc.*, **103**, 811–815.

Caughey, S. J., J. C. Wyngaard, and J. C. Kaimal, 1979: Turbulence in the Evolving Stable Boundary Layer. *J. Atmos. Sci.*, **36**, 1041–1052.

Chow, F. K., A. P. Weigel, R. L. Street, M. W. Rotach, and M. Xue, 2006: High-resolution large-eddy simulations of flow in a steep alpine valley. part i: Methodology, verification, and sensitivity experiments. *Journal of Applied Meteorology and Climatology*, **45 (1)**, 63–86.

Colette, A., F. K. Chow, and R. L. Street, 2003: A numerical study of inversion-layer breakup and the effects of topographic shading in idealized valleys. *J. Appl. Meteorol.*, **42**, 1255–1272.

Davidson, B. and P. K. Rao, 1963: Experimental studies of the valley-plain wind. *J. Air Water Poll.*, **7**, 907–923.

Doran, J. C. and T. W. Horst, 1981: Velocity and Temperature Oscillations in Drainage Winds. *J. Appl. Meteorol.*, **20**, 361–364.

Erasmus, D. A., 1993: Observations of the nocturnal stable boundary layer in the Greeley area. Faculty Research and Publications Board, University of Northern Colorado, Denver, CO.

Fernando, H., et al., 2015: The materhorn: Unraveling the intricacies of mountain weather. *Bulletin of the American Meteorological Society*, **96 (11)**, 1945–1967.

Fernando, H. J. S., B. Verhoef, S. Di Sabatino, L. S. Leo, and S. Park, 2013: The Phoenix Evening Transition Flow Experiment (TRANSFLEX). *Boundary-Layer Meteorol.*, **147**, 443–468.

Fleagle, R. G., 1950: A theory of air drainage. *Journal of Meteorology*, **7**, 227–232.

Google Earth, 2013: Dugway Proving Ground, UT, USA. 40° 8 5.8956 N, –113° 27 7.7976 pp.

Grachev, A. a., L. S. Leo, S. D. Sabatino, H. J. S. Fernando, E. R. Pardyjak, and C. W. Fairall, 2016: Structure of turbulence in katabatic flows below and above the wind-speed maximum. *Boundary-Layer Meteorol.*, **159**, 469–494.

Hang, C., D. F. Nadeau, D. D. Jensen, S. W. Hoch, and E. R. Pardyjak, 2016: Playa soil moisture and evaporation dynamics during the MATERHORN field program. *Boundary-Layer Meteorol.*, **159**, 521–538.

Henninger, D. L., G. W. Petersen, and E. T. Engman, 1976: Surface soil moisture within a watershed: Variations, factors influencing, and relationship to surface runoff. *Soil Sci. Soc. Am. J.*, **40**, 773.

Horst, T. W. and J. C. Doran, 1986: Nocturnal drainage flow on simple slopes. *Boundary-Layer Meteorol.*, **34**, 263–286.

Hunt, J., H. J. S. Fernando, and M. Princevac, 2003: Unsteady thermally driven flows on gentle slopes. *J. Atmos. Sci.*, **60**, 2169–2182.

Idso, S. and R. Jackson, 1975: The dependence of bare soil albedo on soil water content. *J. Appl. Meteorol. Climatol.*, **14 (1)**, 109–113.

Jensen, D. D., D. F. Nadeau, S. W. Hoch, and E. R. Pardyjak, 2016: Observations of near-surface heat-flux and temperature profiles through the early evening transition over contrasting surfaces. *Boundary-Layer Meteorol.*, **159**, 567–587.

Jolliffe, I. T., 2002: Principal component analysis and factor analysis. *Principal Component Analysis*, Springer New York, 150–166.

Lehner, M., C. D. Whiteman, S. W. Hoch, D. Jensen, E. R. Pardyjak, L. S. Leo, S. Di Sabatino, and H. J. S. Fernando, 2015: A case study of the nocturnal boundary layer evolution on a slope at the foot of a desert mountain. *J. Appl. Meteorol. Climatol.*, **54**, 732–751.

Mahrt, L., 1982: Momentum Balance of Gravity Flows. *J. Atmos. Sci.*, **39**, 2701–2711.

Mahrt, L. and S. Larsen, 1990: Relation of slope winds to the ambient flow over gentle terrain. *Boundary-Layer Meteorol.*, **53**, 93–102.

Manins, P. C. and B. L. Sawford, 1979a: A model of katabatic winds. *J. Atmos. Sci.*, **36**, 619–630.

Manins, P. C. and B. L. Sawford, 1979b: Katabatic winds: A field case study. *Quart. J. Roy. Meteor. Soc.*, **105**, 1011–1025.

Massey, J. D., W. J. Steenburgh, S. W. Hoch, and J. C. Knievel, 2014: Sensitivity of near-surface temperature forecasts to soil properties over a sparsely vegetated dryland region. *J. Appl. Meteorol. Climatol.*, **53**, 1976–1995.

McCumber, M. C. and R. A. Pielke, 1981: Simulation of the effects of surface fluxes of heat and moisture in a mesoscale numerical model: 1. Soil layer. *J. of Geophys. Res.*, **86**, 9929–9938.

McKee, T. B. and R. D. O'Neal, 1989: The role of valley geometry and energy budget in the formation of nocturnal valley winds. *J. Appl. Meteorol.*, **28**, 445–456.

McNider, R. T., 1982: A note on velocity fluctuations in drainage flows. *Journal of the Atmospheric Sciences*, **39**, 1658–1660.

Moene, A. F. and J. C. van Dam, 2014: *Transport in the Atmosphere-Vegetation-Soil Continuum*. Cambridge University Press, Cambridge, 446 pp.

Nadeau, D. F., E. R. Pardyjak, C. W. Higgins, H. J. S. Fernando, and M. B. Parlange, 2011: A simple model for the afternoon and early evening decay of convective turbulence over different land surfaces. *Boundary-Layer Meteorol.*, **141**, 301–324.

Nadeau, D. F., E. R. Pardyjak, C. W. Higgins, H. Huwald, and M. B. Parlange, 2013: Flow during the evening transition over steep Alpine slopes. *Q. J. R. Meteorol. Soc.*, **139**, 607–624.

Nappo, C. J., 1991: Sporadic breakdowns of stability in the PBL over simple and complex terrain. *Boundary-Layer Meteorol.*, **54 (1-2)**, 69–87.

Nappo, C. J. and K. Rao, Shankar, 1987: A model study of pure katabatic flows. *Tellus A*, **39**, 61–71.

Neff, W. D. and C. W. King, 1987: Observations of complex-terrain flows using acoustic sounders: Experiments, topography, and winds. *Boundary-Layer Meteorol.*, **40**, 363–392.

Oldroyd, H. J., E. R. Pardyjak, H. Huwald, and M. B. Parlange, 2016: Adapting tilt corrections and the governing flow equations for steep, fully three-dimensional, mountainous terrain. *Boundary-Layer Meteorology*, **159**, 539–565.

Ookouchi, Y., M. Segal, R. C. Kessler, and R. A. Pielke, 1984: Evaluation of soil moisture effects on the generation and modification of mesoscale circulations. *Mon. Weather Rev.*, **112**, 2281–2292.

Papadopoulos, K. H. and C. G. Helmis, 1999: Evening and morning transition of katabatic flows. *Boundary-Layer Meteorology*, **92**, 195–227.

Pardyjak, E. R., H. J. S. Fernando, J. C. Hunt, A. A. Grachev, and J. Anderson, 2009: A case study of the development of nocturnal slope flows in a wide open valley and associated air quality implications. *Meteorol. Zeitschrift*, **18**, 85–100.

Poulos, G. and S. S. Zhong, 2008: An observational history of small-scale katabatic winds in mid-latitudes. *Geogr. Compass*, **2**, 1798–1821.

Rosipal, R. and N. Krämer, 2006: Overview and recent advances in partial least squares. *Subspace, Latent Structure and Feature Selection*, Springer Berlin Heidelberg, 34–51.

Savage, L. C., S. Zhong, W. Yao, W. J. O. Brown, T. W. Horst, and C. D. Whiteman, 2008: An observational and numerical study of a regional-scale downslope flow in Northern Arizona. *J. Geophys. Res.*, **113 (14)**, 1–17.

Schmidli, J., G. S. Poulos, M. H. Daniels, and F. K. Chow, 2009: External influences on nocturnal thermally driven flows in a deep valley. *Journal of Applied Meteorology and Climatology*, **48 (1)**, 3–23.

Start, G. E., C. R. Dickson, and L. L. Wendell, 1974: Diffusion in a canyon within rough mountainous terrain.pdf. *J. Appl. Meteorol.*, **14**, 333–346.

Steinwand, A. L., R. F. Harrington, and D. P. Groeneveld, 2001: Transpiration coefficients for three Great Basin shrubs. *J. Arid Environ.*, **49**, 555–567.

Stull, R., 1988: *An Introduction to Boundary Layer Meteorology*. Springer Science, 666 pp.

Topp, G. C., J. L. Davis, and A. P. Annan, 1980: Electromagnetic determination of soil water content: Measurements in coaxial transmission lines. *Water Resour. Res.*, **16**, 574–582.

Villagrasa, D. M., M. Lehner, C. D. Whiteman, S. W. Hoch, and J. Cuxart, 2013: The upslope-downslope flow transition on a basin sidewall. *J. Appl. Meteorol. Climatol.*, **52**, 2715–2734.

Wagner, A., 1938: Theorie und Beobachtung der periodi schen Gebi rgswi nde [Theory and observation of periodic mountain winds]. *Gerlands Beitr. Geophysik*, **52**, 408–449.

Whiteman, C. and K. Allwine, 1986: Extraterrestrial solar radiation on inclined surfaces. *Environ. Softw.*, **1**, 164–169.

Whiteman, C. D., 2000: *Mountain Meteorology: Fundamentals and Applications*. 1st ed., Oxford University Press, Oxford, 355 pp.

Whiteman, C. D. and S. Zhong, 2008: Downslope flows on a low-angle slope and their interactions with valley inversions. Part I: Observations. *J. Appl. Meteorol.*, **47**, 2023–2038.

Wilczak, J. M., S. P. Oncley, and S. A. Stage, 2001: Sonic anemometer tilt correction algorithms. *Boundary-Layer Meteorol.*, **99**, 127–150.

Zardi, D. and C. D. Whiteman, 2013: Diurnal mountain wind systems. *Mountain weather research and forecasting: recent progress and current challenges*, Springer Science and Business Media, 219–260.

CHAPTER 4

THE MORNING AND EVENING TRANSITIONS OVER COASTAL, TROPICAL TERRAIN

4.1 Introduction

Morning and evening transition processes are typically marked by stark changes in the state of the atmospheric boundary layer. For example, during nighttime hours over land with clear skies, limited large scale advection and calm winds, the statically stable boundary layer (SBL) adjacent to the ground is characterized by weak and intermittent turbulence. Immediately above the SBL, a statically neutral residual layer (RL) persists as a remnant of the mixed layer from the previous day. Just after sunrise, surface heating begins to erode the SBL, eventually recoupling the RL with the ground, which in turn leads to the rapid development of the daytime convective boundary layer (Stull, 1988). The several hour period over which this transition occurs is the morning transition (MT). Similarly, the evening transition (ET) is a several hour period around sunset, when surface heating diminishes and the convective boundary layer (CBL) decays, while a near-surface SBL forms with an overlying RL (Lothon et al., 2014). The daytime CBL and nighttime SBL have been extensively studied and successfully modeled for a range of conditions (see Holtslag et al., 2013; Steeneveld, 2014, for a review). However, accurate modeling of the MT and ET has been much more problematic (Lothon et al., 2014). The processes are inherently transient, daytime scaling laws are invalid (Blay-Carreras et al., 2014; Jensen et al., 2016), turbulence develops/decays anisotropically (e.g. Nieuwstadt and Brost, 1986; Pino et al., 2006; Lampert et al., 2016), the influence in surface heterogeneities is magnified (e.g. Acevedo and Fitzjarrald, 2001; Cuxart

et al., 2016) and the background state evolves rapidly. For example, through the MT, Lenschow et al. (1979) observed temperature and wind speed changes of 12 K and 6 m s^{-1} in less than 30 min.

Due to such complications, only recently have researchers began studying the ET and MT intensively. Such studies are of both fundamental and pragmatic importance because the conditions near the end of the ET and MT serve as the initial condition for prognostic models of the CBL and SBL, respectively (Angevine et al., 2001). To this point, the ET has received more attention than the MT because the development of the CBL shows less sensitivity to the initial condition than the SBL. For example, Acevedo and Fitzjarrald (2001) observed the development of large spatial variability in near-surface temperature through the ET that persisted through much of the night. Such spatial variability that evolves through the night is typically homogenized early in the MT, due to strengthened mixing associated with the development of the CBL (Lenschow et al., 1979).

Studies of the ET have been performed numerically and observationally. In general, the objective is to understand how the near-surface atmosphere responds to the reduction of surface heating. Computational work began with the large-eddy simulations (LES) of Nieuwstadt and Brost (1986), who modeled the decay of convective turbulence when surface heating is cut off abruptly. Since then, modeling efforts have have improved to include more realistic time scales and forcing (e.g. Sorbjan, 1997; Pino et al., 2006; Goulart et al., 2010). In recent years, several large field campaigns have been conducted to study the decay of convective turbulence through the ET (e.g. Grant, 1997; Acevedo and Fitzjarrald, 2001; Brazel et al., 2005; Lothon et al., 2014; Fernando et al., 2015). Blay-Carreras et al. (2014) and Jensen et al. (2016) used tower data collected during the BLLAST and MATERHORN field programs, respectively, to study near-surface countergradient heat fluxes through the ET. Jensen et al. (2016) found that the duration of the countergradient heat flux is proportional to the ratio of the buoyant to gradient production terms in the sensible heat flux tendency equation. Nadeau et al. (2011) used data from the LITFASS-2003 field campaign to successfully model the decay of turbulence through the ET using only the surface buoyancy fluctuations and turbulence dissipation. Later, Nilsson et al.

(2016a) used data from the BLLAST field campaign to make detailed observations of the turbulence kinetic energy budget through the ET. Nilsson et al. (2016b) built on this work by developing a simple model to estimate the terms of the TKE budget as a function of height. The model takes the boundary layer depth, near-surface wind speed and surface buoyancy flux as inputs.

Until somewhat recently, most studies of the MT focused on the rapid-growth phase of the CBL (Angevine et al., 2001). Bange et al. (2007) used helicopter probe measurements to study the rapid evolution of the shallow convective boundary layer (SCBL). They found that entrainment is the most important mechanism for SCBL growth. Sorbjan (2007) used LES beginning after the erosion of the SBL to evaluate similarity relations in the mixed layer with reasonable success. Angevine et al. (2001) used observational data to study the full MT, including the erosion of the SBL early in the MT. They observe that surface heating is responsible for relaxing surface stability but that most of the warming in the near-surface air mass is due to shear driven entrainment. Similarly, the six-year dataset analyzed in Lapworth (2006) confirms that through the MT, nearly all warming in the surface layer is due to turbulent diffusion from above. Beare (2008) also confirmed this finding numerically by using a combination of grid sizes to run an LES study of the full evolution of the MT. In the study, the mixed CBL–SBL state, consisting of a near surface convective layer capped by a shear driven stable layer, is resolved. Shear production is found to be the dominant source of turbulence production throughout the MT.

Only a small number of studies have examined both the ET and MT in a single study. In all cases that we are aware of, the studies have focused on the diurnal cycle, rather than processes unique to the MT and ET. Several studies have successfully modeled a full diurnal cycle using LES (e.g. Wang et al., 1998; Kumar et al., 2006; Basu et al., 2008; Rizza et al., 2013), and others have studied the diurnal cycle utilizing mesoscale models (e.g. Zhang et al., 2004; Svensson et al., 2011).

Studies of coastal flow in tropical regions have also received little attention, given that most observations have been made in the mid-latitudes. In this study, both onshore and offshore flow in a tropical environment is considered. As the flow crosses the coast, an internal-boundary layer (IBL) develops as the air mass near the surface

adapts to the changing surface conditions (see Garratt, 1990; Angevine, 2008, for reviews). In the case of daytime onshore flow, the surface transitions from the smooth, cool ocean to the rough, warm land. The flow decelerates and turbulence increases, the deepening of the IBL is roughly proportional to the square root of the inland distance, depending on stability and surface roughness (Garratt, 1990). For the offshore case, the flow accelerates and turbulence decays proportional to the drop in surface roughness between the land and the sea. The study of Parameswaran et al. (1997) used data collected at a tropical coastal station to study the influence of the coastal transition on aerosol concentrations through the ET. Similarly, Manoj et al. (2013) used lidar data collected over a tropical, urban site in India to relate the development of low-level stratoform clouds to aerosol concentrations. We are unaware of any studies that investigate the MT and ET over coastal, tropical terrain.

In the present study, we use an extensive 30-month dataset to study processes specific to the MT and ET. Data were collected on three tall masts at a coastal site over heterogeneous terrain in Belize. The structure of the study is as follows. First, the predominant wind regimes are discussed. Second, composite time series of meteorological variables are used to study the development of the mean and turbulence variables through the MT and ET. Next, multiresolution flux decomposition is used to study the scales of turbulence. Finally, the budget of TKE is examined.

4.2 Methods

Data for the study were collected as part of a wind-resource assessment over a shrimp farm in Stann Creek, Belize. Data collection began on 1 December 2013 and concluded on 25 April 2016.

4.2.1 Study Area

Three experimental sites are used in the study. The Beach, Shrimp Farm and Substation sites form an approximate inland transect between 0 and 5 km. Fig. 4.1 gives the location of the sites and site photos are shown in Fig. 4.2. Elevation change between the sites is minimal, with approximate elevations of 2, 9 and 20 m at Beach, Shrimp Farm and Substation, respectively. Discussion of site heterogeneity

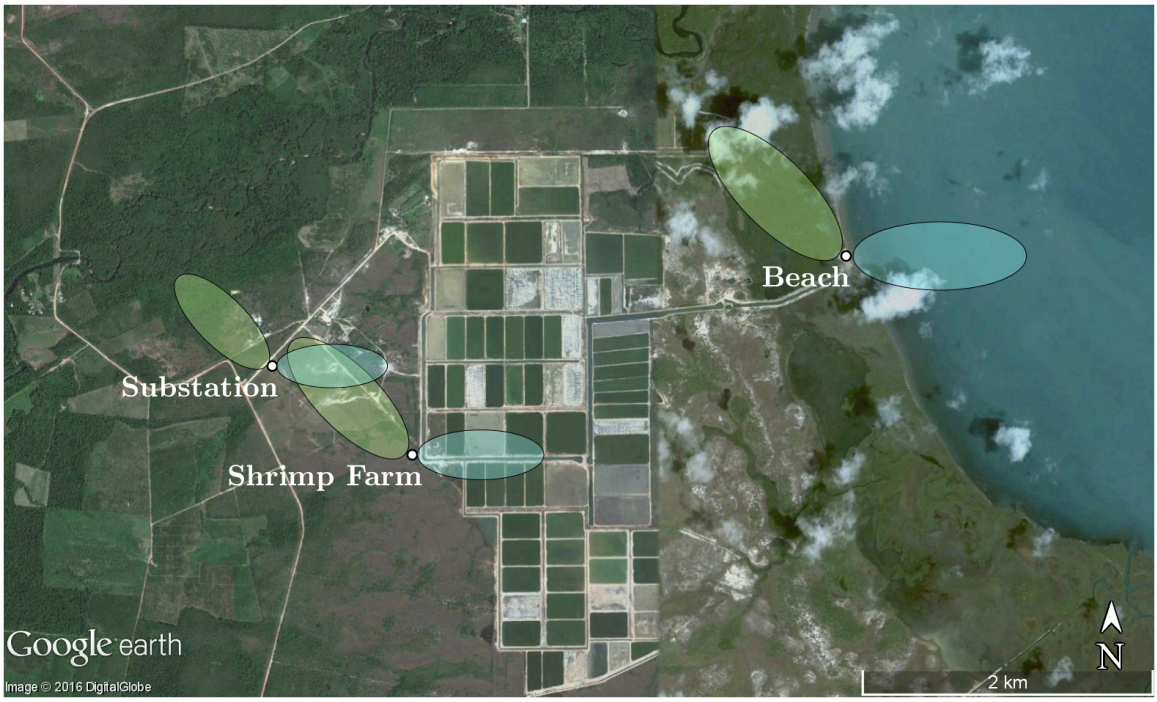

Figure 4.1: Map of the study area, patches in the center of the image are shrimp ponds that are approximately 1.5 m in depth. The transparent ellipse represent the approximate onshore (blue) and offshore (green) flux footprints calculated at a height of 10 m for weakly unstable conditions using eq. 4.1 (See Sect. 4.3.1).

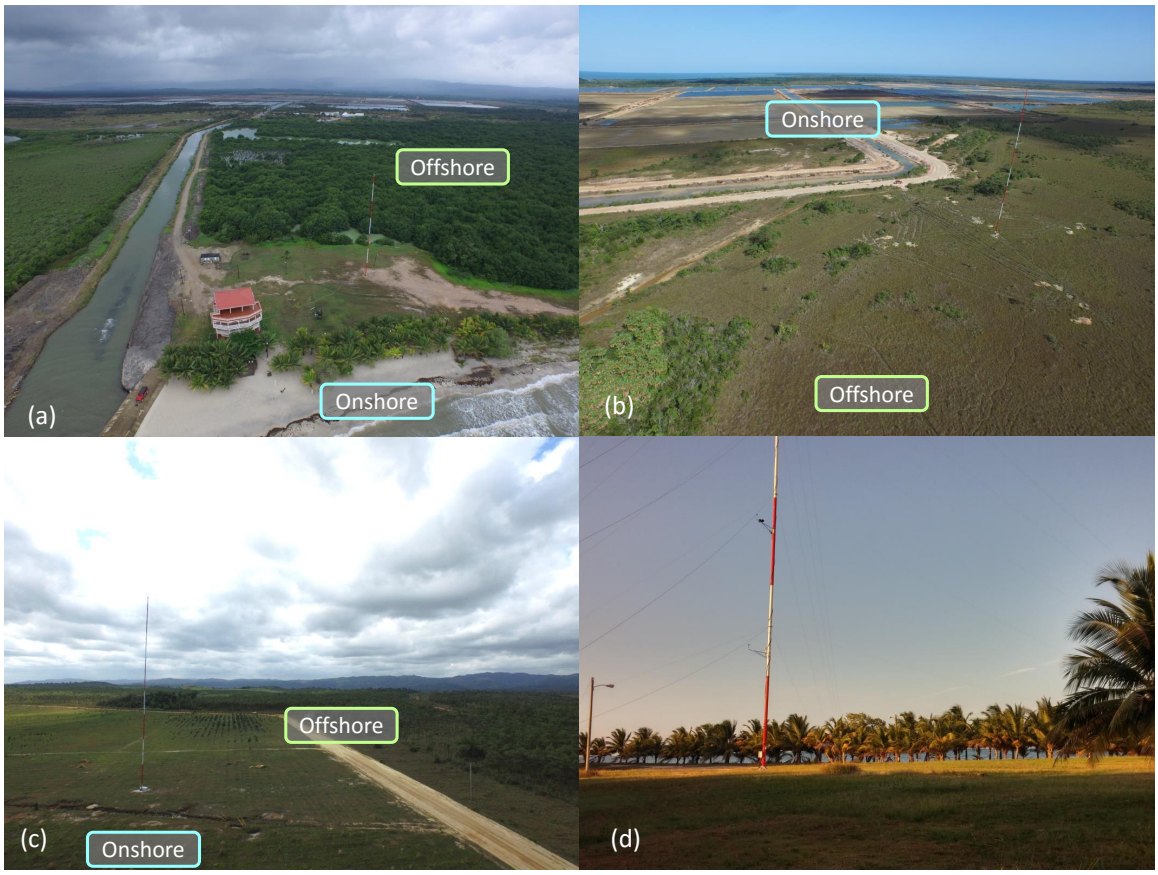

Figure 4.2: Photos of the (a) Beach (b) Shrimp Farm and (c) Substation sites, with the approximate onshore and offshore fetches indicated (see Sect. 4.3.1), and (d) along-shore wind break at the Beach site.

and tower fetches is found in Sect. 4.3.1. At the Beach site, a three-row wind break of palms exists between the Beach tower and the ocean (Fig. 4.2 (d)). The break is approximately 15 m wide and begins 35 m to the east of the Beach tower. The height of the canopy base is approximately 2 m and the height of the top of the canopy is approximately 6 m.

4.2.2 Instrumentation

Mean variables were sampled at multiple levels at all sites and sonic anemometers were used to measure turbulence at the Beach and Substation sites. Fig. 4.3 illustrates the instrumentation at each site and Table 4.1 gives instrument details. Each tower level was instrumented with redundant anemometers. Unless otherwise noted, all mean wind speeds were taken from the cup anemometers. Mean variables were sampled at 1 Hz; turbulence was initially sampled at 20 Hz and subsequently dropped to 10 Hz to improve logger stability.

Data were stored locally on Campbell Scientific data loggers and 10-min averaged data were transmitted via cellular modems nightly. Because of the remoteness of the site, instrumentation problems could not always be corrected immediately, thus, data availability diminished slightly through the experiment.

4.2.3 Data Analysis

Data were analyzed with the Utah Turbulence in Environmental Studies processing and analysis code (UTESpac, Jensen et al., 2016). A multisector planar fit and subsequent yaw rotation was applied to the sonic anemometer data to align the sonic coordinate system with the mean wind field. u is the longitudinal velocity, v the transverse and w the vertical. Given that the emphasis of the study is on the MT and ET, where conditions evolve rapidly, 10-min averaging periods were used to compute both the mean variables and higher-order moments. Later in section 4.3.3, we show that 10-min is sufficient to capture the majority of the turbulent flux while omitting larger-scale fluctuations associated with the meso- and synoptic scales.

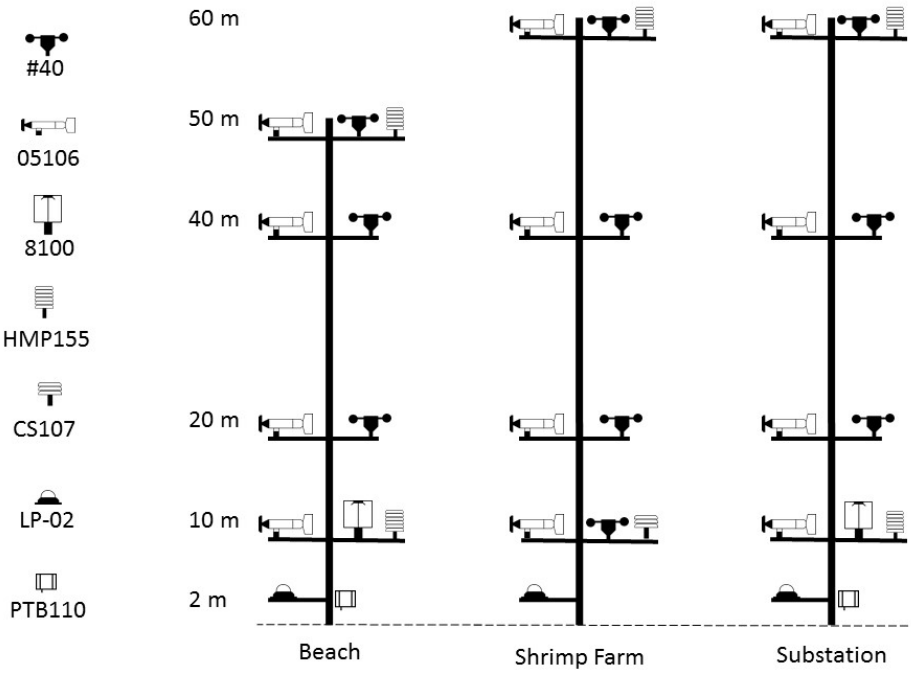

Figure 4.3: Instrumentation deployed at the three sites. See Table 4.1 for instrument details.

Table 4.1: Instrumentation deployed during the 30-month field campaign. See Fig. 4.3 for instrument locations. WS is wind speed; u, v and w are the longitudinal, transverse and vertical wind speed, respectively; T_s is the sonic derived temperature and is approximately equal to virtual temperature; T is air temperature; RH is relative humidity, $R_S\downarrow$ is incoming global shortwave radiation and P is pressure.

Instrument name	Variables measured	Accuracy	Manufacturer
NRG #40	WS	± 0.15 m s^{-1}	NRG Systems
RMY05106	WS	± 0.3 m s^{-1}	R.M. Young
RMY8100	u, v, w T_s	±0.05 m s^{-1} ± 2°C	R.M. Young
HMP155	T RH	± 0.2°C ±1%	Vaisala
CS107	T	± 0.4°C	Campbell Sci.
LP-02	$R_S\downarrow$	± 10%/day	Huskeflux
PTB110	P	± 0.6 mb	Vaisala

4.2.4 Morning and Evening Transition

To examine the morning and evening transition, time relative to sunrise (τ_{sunrise}) and sunset (τ_{sunset}) is used. Fig. 4.4 gives the sunrise and sunset times at all sites. The time of sunrise and sunset was calculated with a threshold of 5 W m^{-2}. The calculated transition times were then smoothed using the smooth.m function in Matlab with the "rloess" option. A simple solar model was also tested but was unable to account for diffuse effects that apparently vary seasonally. Sunrise and sunset were assumed to be constant at all three sites and the transition times, τ_{sunrise} and τ_{sunset}, were taken from the smoothed signals. Because Belize is in the tropics (17° N), the annual variation in sunrise and sunset is less than sites in the mid-latitudes.

4.3 Results and Discussion

4.3.1 Wind Regimes

The prevailing wind directions were identified using their probability density function (Fig. 4.5). The distributions are strongly bimodal, with the predominant wind regimes being easterly onshore and northwesterly offshore. The shading indicates the predominant wind directions; blue indicates onshore winds and green indicates offshore winds. The width of the bins is 45° and is centered around 90° for onshore flow and 315° for offshore flow.

Contours of the time series of 40-m wind direction are shown in Fig. 4.6. The contours illustrate that the bimodal flow regime is seasonal, rather than diurnal, as might be expected for thermally driven sea breezes (see Stull, 1988, Sect. 14.1.2). The observed wind regimes are consistent with those typical of the region (see National Meteorological Service of Belize, 2016, Figures 5–8). The onshore regime occurs mostly during the rainy season (April – October) and the offshore regime occurs primarily during the dry season (November–March). Though the actual mechanisms driving the flow are more complicated (Sáenz and Durán-Quesada, 2015), the onshore flow and precipitation is predominantly driven by tropical waves, tropical storms and hurricanes that move westward through the Carribbean. The offshore flow is produced by cold fronts that move southeast across the continental United States. On average, a cold front passes over Belize about once in every ten days through the dry season

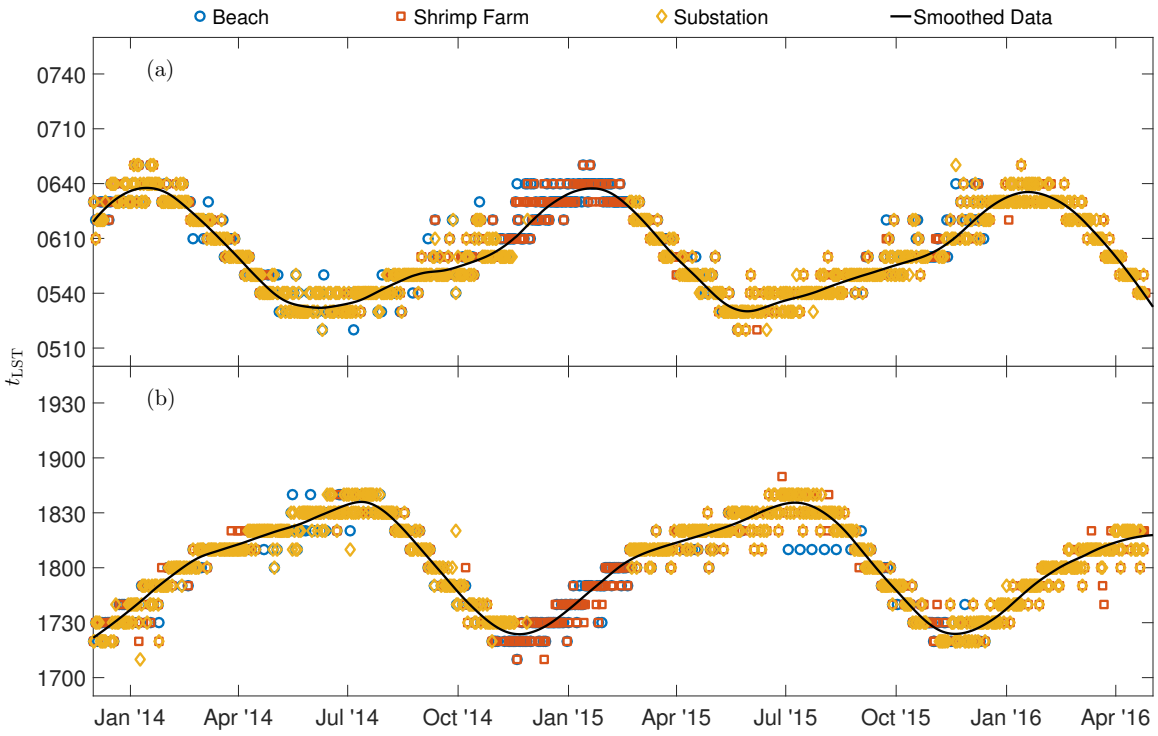

Figure 4.4: Sunrise (a) and sunset (b) times inferred from $R_S \downarrow$ observations at the three sites. The stratification in the calculated sunrises and sunsets is due to the 10-min resolution of the dataset. The smoothed signal is used to estimate τ_{sunrise} and τ_{sunrise} at all sites.

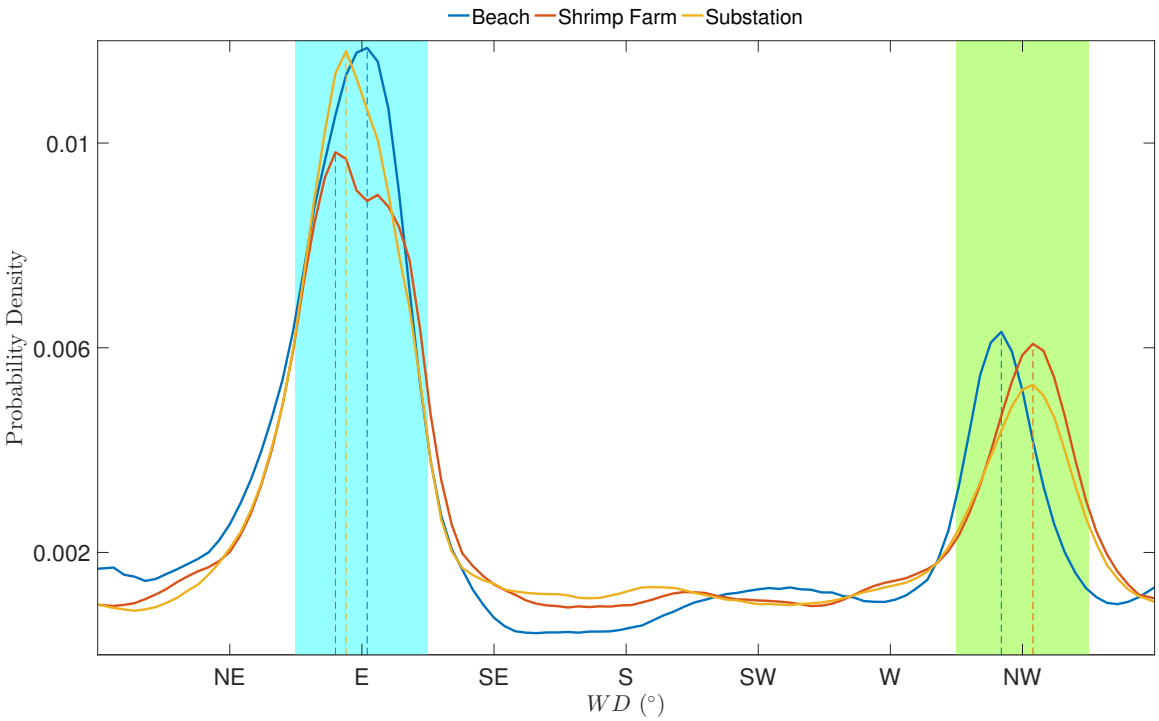

Figure 4.5: 40-m wind direction probability density functions. Blue shading indicates the onshore flow regime ($90° \pm 22.5°$) and green indicates the offshore flow regime ($315° \pm 22.5°$).

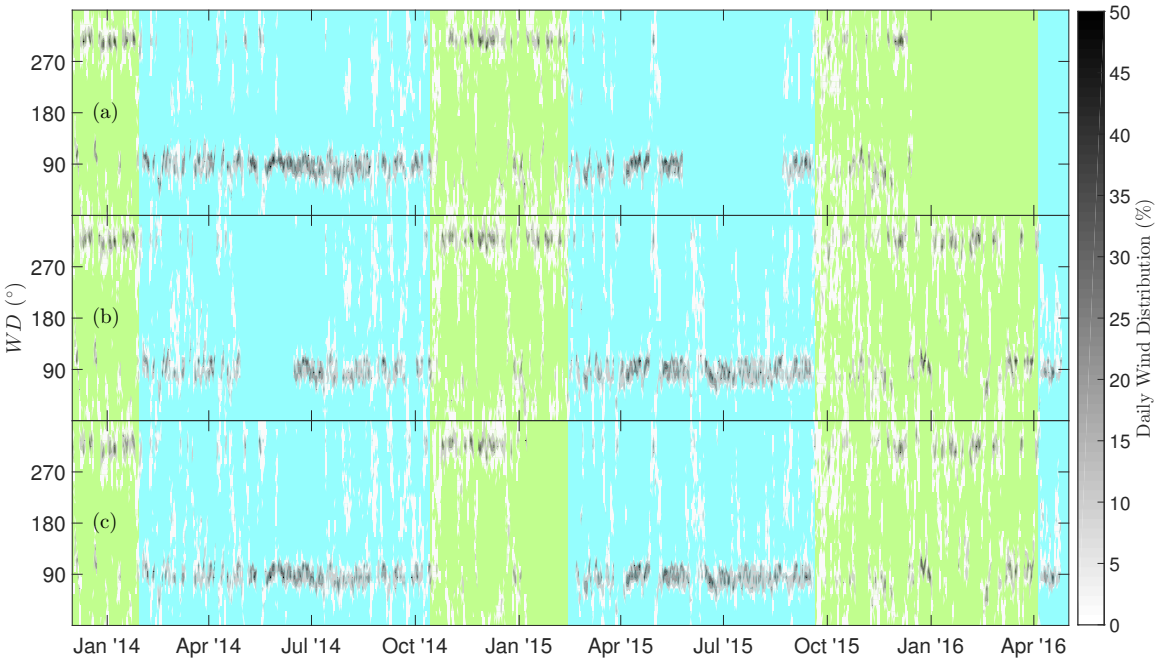

Figure 4.6: Wind direction contours at (a) Beach, (b) Shrimp Farm and (c) Substation. The onshore and offshore regimes are indicated by the blue and green shading, respectively. Gaps in the time series indicate periods with instrument malfunctions.

(National Meteorological Service of Belize, 2016). The variability in the arrival of the cold fronts leads to more variability in wind direction through the dry season (Fig. 4.6).

Regardless of season, the air temperature remains relatively constant throughout the year. Fig. 4.7 illustrates the 10-m maximum and minimum daily temperatures and relative humidity throughout the field program. The amplitude of the daily minimum (maximum) annual temperature oscillation, computed as the difference between the 95$^{\text{th}}$ and 5$^{\text{th}}$ percentiles, is ≈ 7 °C (5 °C) at all sites. The mean diurnal temperature range is approximately 3.6 °C at Beach and 4.5 °C at Shrimp Farm and Substation. Finally, at all sites, the relative humidity is persistently between 80 and 90 %.

Given that the flow regimes are predominantly seasonal, rather than diurnal, days can be characterized by the mode of the 40-m wind direction. The daily wind mode is computed by sorting the wind direction into bins with widths of 10°. In general, the daily wind mode is a very good indicator of the predominant wind direction for a given day.

Table 4.2 describes the two flow regimes. Days whose wind modes are neither onshore nor offshore were omitted from the study. We are left with well over 300 days of onshore flow at all sites and over 100 days of offshore flow at all sites. This allows us to composite a tremendous amount of data to allow for a more climatological analysis of the two flow regimes, rather than studying isolated events.

As illustrated in Fig. 4.1 and 4.2, the three sites are situated approximately at land cover transition zones, therefore, the upwind fetches vary between wind regimes. At the Beach site, the tower sits roughly 70 meters from the ocean shore, with a wind break positioned parallel to the beach and between the shore and tower (see Sect. 4.2.1). The offshore regime consists predominantly of mangrove forest that is approximately 5 m tall. At the Shrimp Farm site, the onshore fetch is over shrimp ponds that are approximately 1.5 m in depth. All ponds have a north-south dimension of ≈ 300 m and an east-west dimension of either 150 or 300 m (Fig. 4.1). Throughout the experiment, the shrimp ponds were periodically emptied for cleaning and harvesting. From June 2015 through the end of the experiment, the ponds

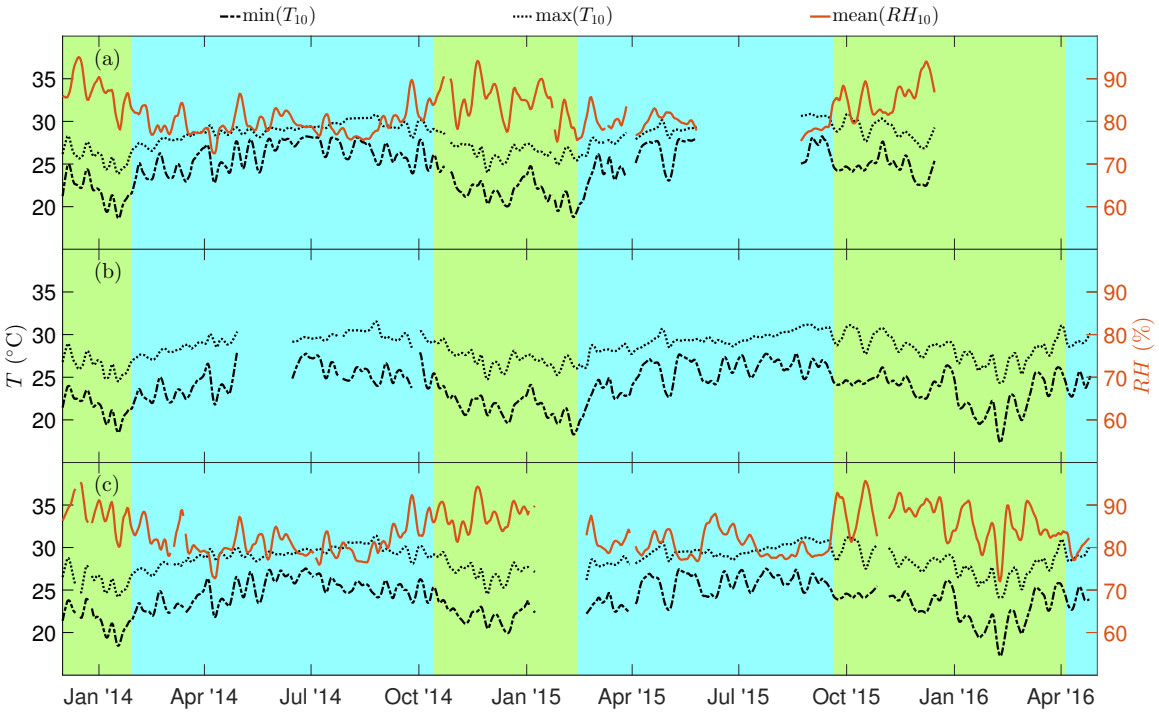

Figure 4.7: Daily minimum and maximum air temperatures at (a) Beach, (b) Shrimp Farm and (c) Substation. Also, at Beach and Substation, the mean daily 10-m relative humidity is reported. A 10-day running average has been applied to smooth the data. Gaps in the time series indicate periods with instrument malfunctions.

Table 4.2: Flow regime characterization at the three sites for onshore ($90° \pm 22.5°$) and offshore ($315° \pm 22.5°$) flow. The days are sorted by their daily wind mode observed at 40 m. *Freq.* is the percentage of the 10-min, 40-m wind observations that falls within the wind-direction envelope. z_0 is estimated from Fig. 9.6 in Stull (1988).

	Onshore Regime				**Offshore Regime**			
	Freq. (%)	*No. of days*	*Fetch*	z_0 (m)	*Freq.* (%)	*No. of days*	*Fetch*	z_0 (m)
Beach	42.9	368	Ocean	10^{-3}	18.0	160	Mangrove	0.4
Shrimp Farm	38.9	465	Shrimp Ponds	0.03	19.6	209	Grassland/ Tropical Forest	0.5
Substation	41.3	482	Grassland	0.08	18	189	Tropical Forest	0.8

were typically empty. In the present study, differences between the emptied and filled ponds are not considered. The offshore fetch at Shrimp Farm is predominantly tropical grassland with presumably some influence from tropical forests located farther upstream. Finally, the Substation site is located over an immature grove of mahogany trees. Though not explicitly measured, from photography, the height of the trees did not change substantially over the experiment, with small saplings near the tower base and trees between 3–5 m tall ≈ 100 m to the west of the tower (Fig. 4.1 (a)). Beyond the grove, the offshore fetch is predominantly tropical forest with hills approximately 8 km to west of the tower. Finally, the onshore fetch is mostly tropical grassland with shrimp ponds and the ocean further upstream.

Because of the heterogeneous topography at each site, it is difficult to accurately estimate the surface roughness (z_0) and zero-plane displacement using both profile methods (Robinson, 1962) and single-level sonic anemometer estimates (Graf et al., 2014). Instead, the surface roughness was estimated as a best guess, using a combination of the profile method and Fig. 9.6 in Stull (1988). Though this leads to uncertainty in the estimate of z_0, the parameter is only used in this study to calculate the approximate flux footprints at each site. Therefore, the added uncertainty is tolerated.

The flux footprints for both wind regimes at all three sites are indicated by shaded ellipses in Fig. 4.1. Their major axes, x_{FP}, are estimated following Hsieh et al. (2000) as

$$x_{\mathrm{FP}} = \frac{D z_u^p |L|^{1-p}}{\kappa^2 \ln(F^*)}, \tag{4.1}$$

where D and p are stability-dependent constants, $z_u = z_m(\ln(z - m/z_0) - 1 + z_0/z_m$ is a combined length scale where z_m is the measurement height, $\kappa = 0.4$ is the von Kármán constant and F^*, taken here as 0.9, is the fraction of the total flux generated between the tower base and an upwind distance of x_{FP}. The Obukhov length is calculated by

$$L = \frac{-\overline{\theta_v} u_*^3}{\kappa g \overline{w'\theta_v'}}, \tag{4.2}$$

where θ_v is the virtual potential temperature, estimated here by the sonic derived

air temperature θ_s, u_* is the friction velocity and g is gravitational acceleration. Qualitatively, the magnitude of L indicates the depth over which shear production of turbulence is important (Stull, 1988).

The flux footprints were estimated at 10-m (the level of the sonic anemometers) under slightly unstable conditions typical at the beginning of the ET or end of the MT. For higher tower levels or stable conditions, the flux footprint becomes much larger. Nonetheless, the calculated footprints show the general area of upwind fetch for each flow regime at each tower.

Composite time series of the normalized wind speed and wind direction for the onshore and offshore flow regimes are shown in Fig. 4.8 and 4.9, respectively. The wind speed is normalized by the maximum wind speed in the composite time series for both wind regimes and at all sites. The maximum occurs at the Beach site for the onshore regime. The normalization is performed in order to not disclose the wind resource and also to visualize the inland wind speed deficit.

In general, the onshore wind regime is associated with higher wind speeds. At the Beach site, the offshore winds are typically < 75% of the onshore values. In both cases, the diurnal range of the Beach wind speed is quite small relative to the other sites. At the Shrimp Farm and Substation sites, the difference in wind speed is less between the two flow regimes. However, the onshore regime is still associated with stronger winds. There is also a much stronger diurnal signal in the wind speed for the onshore regime, with the higher winds associated with daytime hours. The strengthening of the winds is associated with a superposition of the larger scale synoptic conditions and the thermally driven sea breeze. The existence of the sea breeze is evident from the inland temperature gradient. This is further illustrated by the narrowing of the wind direction distribution (indicated by the standard deviation) through daylight hours, where both the larger scale circulation and sea breeze are congruently driving the flow inland. At night, when the sea breeze transitions to a land breeze, the wind direction distribution widens and the wind speed decreases as a result of the land breeze working against the onshore flow.

For the onshore wind regime, the inland wind speed deficit is much more pronounced. Taking the mean velocity at each site and using a linear fit, the inland

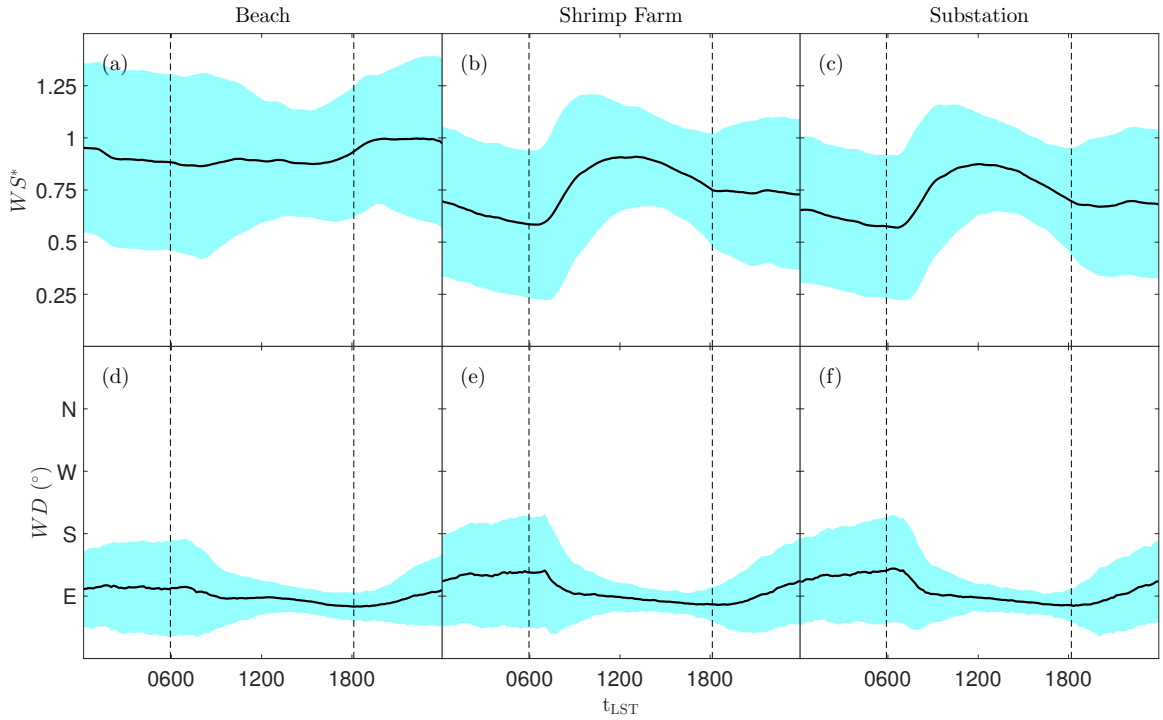

Figure 4.8: 40-m composite wind speed and wind direction time series for the onshore flow regime at Beach (a) and (d), Shrimp Farm (b) and (e) and Substation (c) and (f). Note that the wind speed (WS^*) is the wind speed normalized by the maximum observed velocity in either regime and all sites; this occurs in the onshore regime at Beach. The shading illustrates ±1 standard deviation from the mean and the mean time of sunrise and sunset for the onshore flow regime is indicated by the vertical lines.

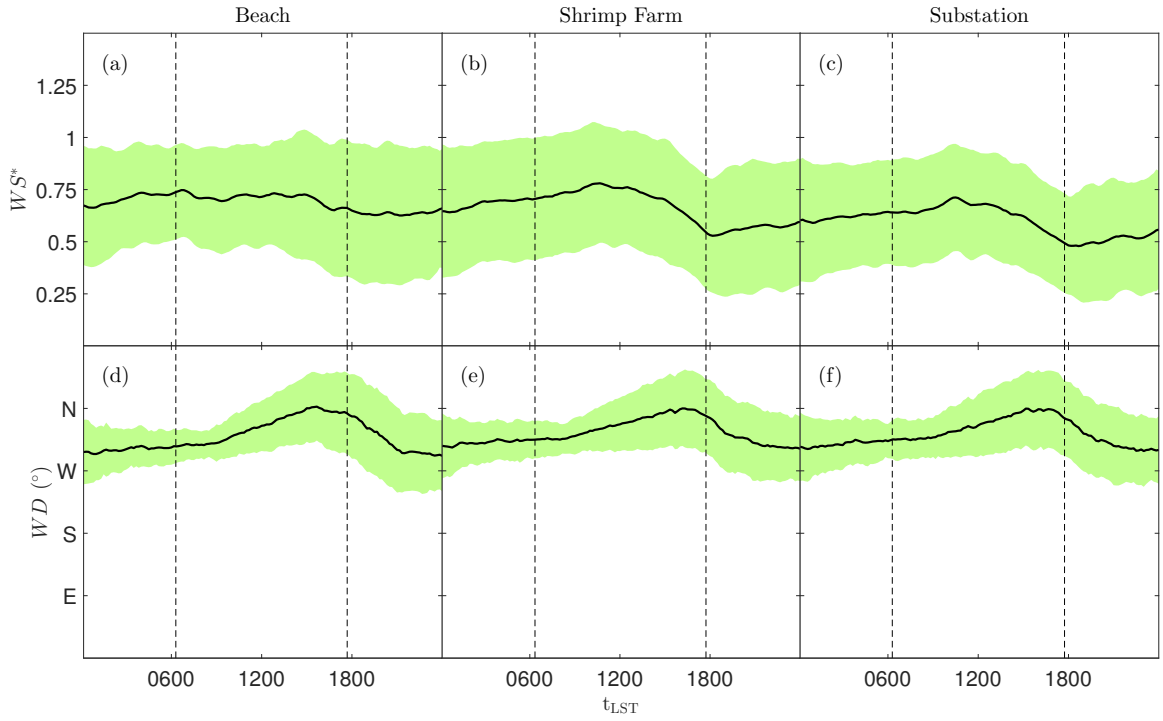

Figure 4.9: Same as Fig. 4.8 but for the offshore flow regime.

wind speed deficit is estimated to be approximately 5% km^{-1}. The offshore deficit is much smaller but, interestingly, slightly higher mean winds are still observed at the Beach site. This is largely due to the calmer winds that occur through the ET as the Shrimp Farm and Substation sites but does not occur at the Beach site.

4.3.2 Mean Transition Behaviour

In this section, the mean behaviour through the MT and ET is considered with composite time series of turbulence variables. Since sonic anemometers were only deployed at the 10-m level at Beach and Substation, there is no discussion of the Shrimp Farm site. However, based on similarities between Shrimp Farm and Substation in the previous section, we use the Beach site observations to characterize the coastal evolution and Substation to characterize the inland evolution.

The sensible heat flux and potential temperature gradient in Fig. 4.10 indicate that countergradient heat fluxes occur through the ET and MT at both sites. Near-surface countergradient heat fluxes through the ET have been discussed previously in Blay-Carreras et al. (2014) and Jensen et al. (2016). Blay-Carreras et al. (2014) observed countergradient durations of 30–80 minutes using heat flux observations at a height of 2.23 m and gradient observations calculated with temperature measurements at 2.23 and 3.23 m. The crossover point of the sensible heat flux was found to always precede the crossover point of the temperature gradient. Jensen et al. (2016) studied near-surface countergradient heat fluxes at multiple levels between 0.5 and 20 m at two contrasting sites. Jensen et al. (2016) observed both the crossover of sensible heat flux occurring prior to the crossover of the temperature gradient, consistent with the observations of Blay-Carreras et al. (2014), as well as the opposite, where the temperature gradient crossover precedes the heat flux crossover. They modeled the countergradient type and countergradient duration by considering the ratio of gradient to buoyant production in the sensible heat flux budget.

At Substation and Beach through the ET, the temperature gradient is observed to crossover prior to the crossover of the heat flux, opposite to what was observed by Blay-Carreras et al. (2014), though the countergradient duration at Substation for the onshore flow regime is very short. It should be noted that the situation encountered

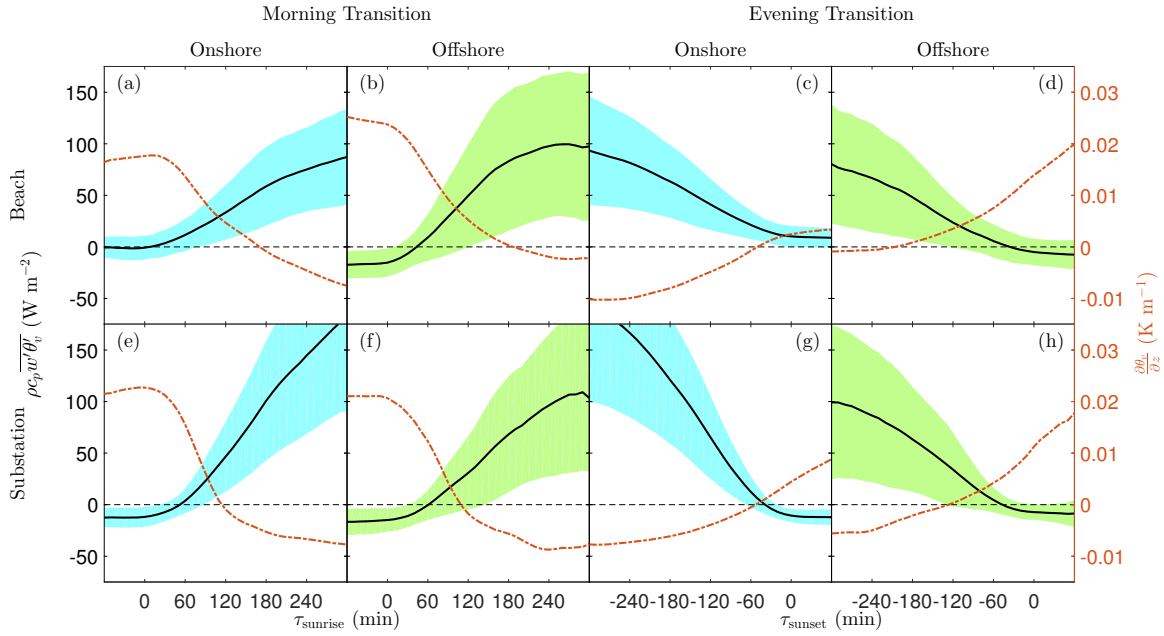

Figure 4.10: Composite time series of the 10-m sensible heat flux and potential temperature gradient through the MT and ET for both onshore (40-m daily wind mode = $90 \pm 22.5°$) and offshore (40-m daily wind mode = $315 \pm 22.5°$) flow regimes at Beach and Substation. The shading indicates ±1 standard deviation of the composite sensible heat flux time series. The virtual potential temperature gradient is computed with forward differencing between the 10 and 50 (60) m levels at Beach (Substation).

in the present study is broadly different from the observations of Blay-Carreras et al. (2014) and Jensen et al. (2016). First, the temperature gradient is computed over a vertical distance of 40 or 50 m, creating a large degree of uncertainty in the estimate of the local temperature gradient. Second, the sites considered here are characterized by heterogeneous terrain, indicating that advection is important, particularly for the onshore regime at Beach.

Nonetheless, the observations presented here build on existing literature and indicate that the use of the so-called "gradient-transport theory" or "K-theory" is poorly suited for the MT and ET. This is due to the rapid evolution of the atmoshere through such transitions, where local gradients become poor indicators of the scales that are actually responsible for transporting sensible heat. The application here is further complicated by the heterogeneous terrain and advection.

It is interesting that at both sites and for both flow regimes, the sensible heat flux crossover precedes the gradient crossover for the MT, while the opposite is true through the ET. This occurs in both the composite time series as well as many individual days (not shown). This indicates that for a given day, the total duration of positive sensible heat flux (directed away from the surface) is longer than the total duration of the unstable temperature gradient. Based on previous work (see Jensen et al., 2016), we hypothesize that if the temperature gradient were observed locally, just above the surface, that the countergradient duration would shrink to nearly zero. Although we are unable to validate the hypothesis, we observe that in general, the countergradient duration at Substation is much shorter than at Beach. We also observe that the sensible heat flux is typically much larger at Substation, leading to stronger mixing and thus shorter countergradient durations.

Next, stability through the MT and ET is considered using the stability parameter, defined as $\zeta = z/L$, where L is the Obukhov length (Eq. 4.2) and $z = 10$ m is the height where the observations were made. The composite time series of ζ is presented in Fig. 4.11. For ζ only, the composite time series is constructed using the median, rather than the mean. This is done to limit the influence of extremely large and small values that occur in L through the MT and ET. Qualitatively, $\zeta < 0$ for for unstable conditions, $\zeta \approx 0$ for neutral conditions and $\zeta > 0$ for stable conditions.

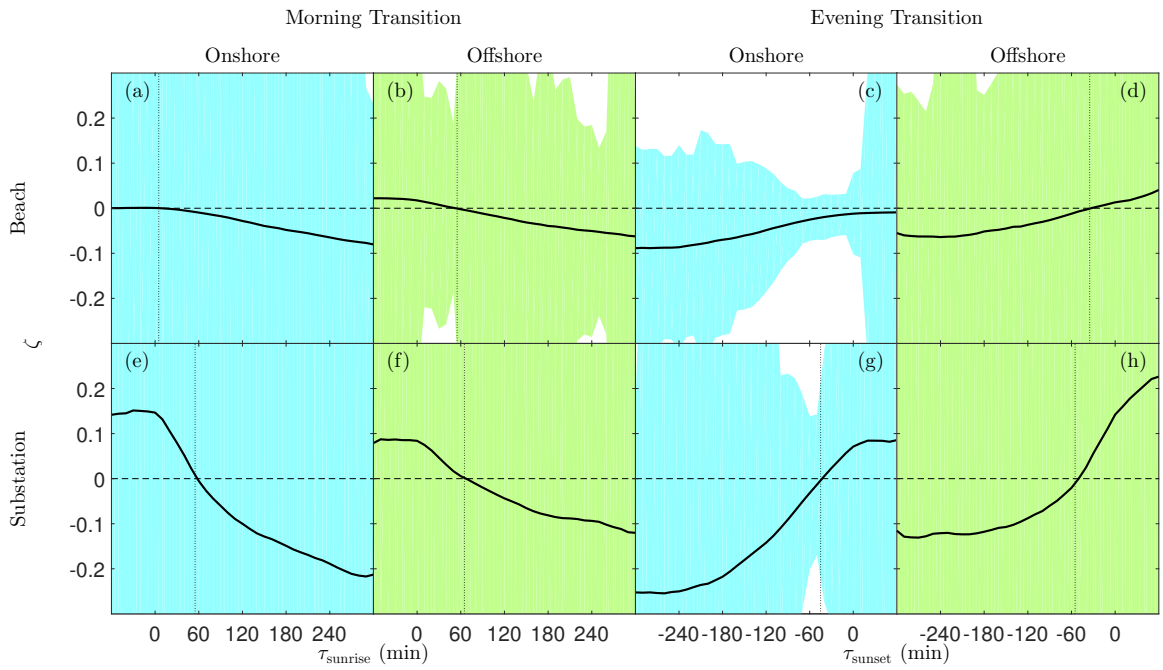

Figure 4.11: Composite time series of the stability parameter, $\zeta = z/L$, computed at 10 m at Beach and Substation through the MT and ET for both flow regimes. For the composite time series of ζ only, the median, rather than the mean, is used. This is done to limit the influence of extreme values that occur in L through the transition. If a crossover in stability occurs through the transition, it is indicated by a dashed vertical line. The shading indicates the time series ± 1 standard deviation.

With the exception of the onshore regime at Beach through the ET, the variability in ζ is large for all cases. Stability at the Beach site is typically near neutral or slightly unstable throughout the diurnal cycle for the onshore regime. This behaviour has been observed previously over tropical oceans (Garratt, 1994) and indicates that the warm Caribbean water is able to drive a positive sensible heat flux through nearly the entire day. For the Beach offshore regime and both wind regimes at the Substation site, the crossover in stability typically occurs $\approx$ 60 min after sunrise and $\approx$ 60 min prior to sunset, indicating that, during the first hour after sunrise and the last hour prior to sunset, insolation is insufficient to drive an upward sensible heat flux, indicating that all warming that occurs through the MT, prior to the crossover of ζ, must be generated by a mechanism other than sensible heat flux, such as horizontal advection, radiative/sensible heat flux divergence or surface inhomogeneities (Angevine, 2008). Though all mechanisms likely play a role, from previous literature (e.g. Lenschow et al., 1979; Angevine et al., 2001; Lapworth, 2006), it has been shown that the majority of warming through the beginning of the MT is driven by entrainment of warm air.

Next, the composite time series of turbulence kinetic energy, defined as $\overline{e} = \frac{1}{2}(\overline{u'^2} + \overline{v'^2} + \overline{w'^2})$, is given in Fig. 4.12. With the exception of the Beach onshore regime, $\overline{e}$ shows the expected behaviour. Typically through the MT, $\overline{e}$ increases in response to increased surface heating and then decreases through the ET due to decreased surface heating. For the Beach onshore regime, the behaviour is unique because $\overline{e}$ varies little in response to solar forcing and for the ET, $\overline{e}$ actually increases late in the evening, when the solar forcing has been cut off. This indicates that shear production of $\overline{e}$ is very important for the Beach onshore regime and is consistent with the observed increase in wind speed (Fig. 4.8). It is unclear whether this would be the case if the wind break were not present. However, we speculate that due to the high wind speed and relatively low surface heating associated with the onshore wind regime that shear production of TKE is the dominant source of turbulence generation. In Sect. 4.3.4, the budget of $\overline{e}$ is discussed in detail.

Finally, the sea breeze, inferred by the horizontal temperature gradient, $\partial T/\partial x$, is considered. For typical sea breeze circulations, surface heating warms the inland

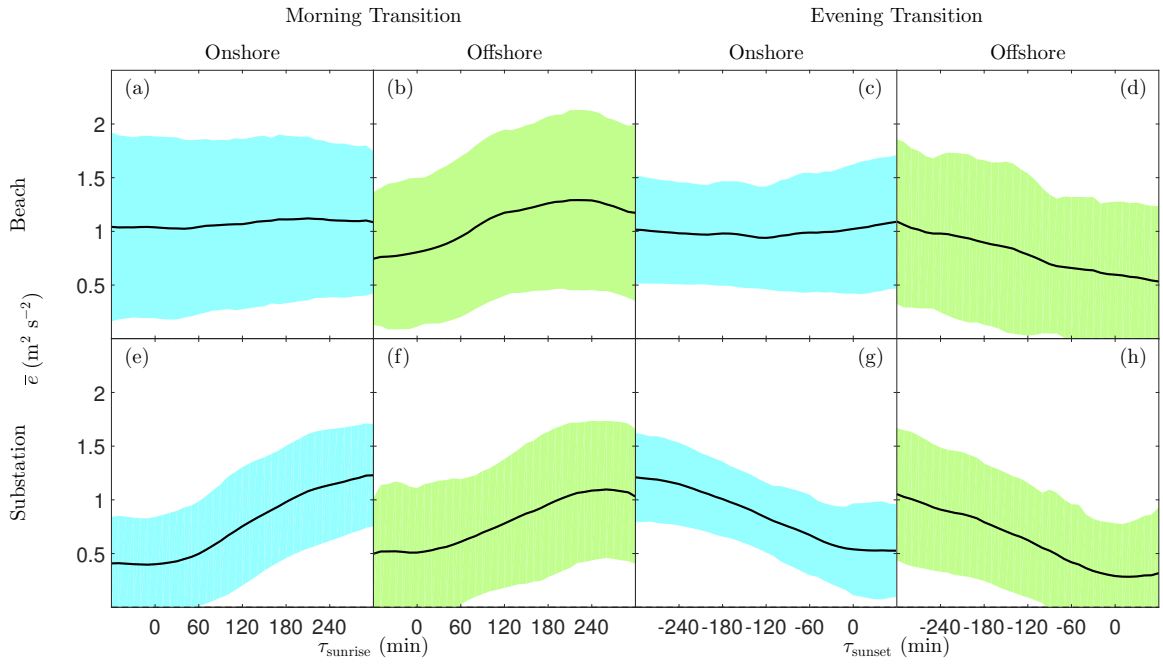

Figure 4.12: Same as Fig. 4.11 but for turbulence kinetic energy.

air mass causing it to rise, the cool air over the body of water then flows inland due to the horizontal pressure gradient generated by the rising inland air mass. During the night, the opposite occurs and the cooler inland air mass flows toward the warmer body of water (Stull, 1988). Fig. 4.13 illustrates the horizontal temperature gradients responsible for driving the sea/land breeze circulation over the shrimp farm. However, as noted in Sect. 4.3.1, the influence of the land/sea breeze is insufficient to overpower the prevailing synoptic forcing that dominates the onshore and offshore flow regimes (National Meteorological Service of Belize, 2016). Nonetheless, Fig. 4.13 illustrates the interaction between the land/sea breeze and the prevailing synoptic forcing. Of particular interest is the crossover in the horizontal temperature gradient. For the morning onshore regime, the crossover in $\partial T/\partial x$ occurs a little more than 2 hours after sunrise; this is more than an hour later than the offshore case. For the evening transition, the onshore crossover again occurs more than an hour before the offshore case. From this, we observe that the duration of the positive inland temperature gradient is much shorter lived for the onshore flow. The reason for this is not immediately clear but is likely related to seasonality and increased precipitation through most of the onshore flow regime.

4.3.3 Multiresolution Flux Decomposition

Multiresolution flux decomposition (MRFD) is a tool which is similar to Fourier decomposition but has the advantage of satisfying Reynold's averaging at all scales and does not assume periodicity (Howell and Mahrt, 1997). MRFD is implemented by decomposing the signal into simple averages computed over different time scales and represents the simplest possible orthogonal decomposition (see Vickers and Mahrt, 2003). Similar to Fourier spectra, MRFD can be used to show the time scales that contribute to the variance of the signal. Vickers and Mahrt (2003) used MRFD to determine the proper flux averaging period by identifying the cospectral gap between turbulence fluctuations and mesoscale motions. Katul and Parlange (1995) used MRFD to study the structure of turbulence at production wave numbers.

Here, we use MRFD to study the structure of turbulence through the MT and ET at the Beach and Substation sites. We follow the methodology described in Vickers

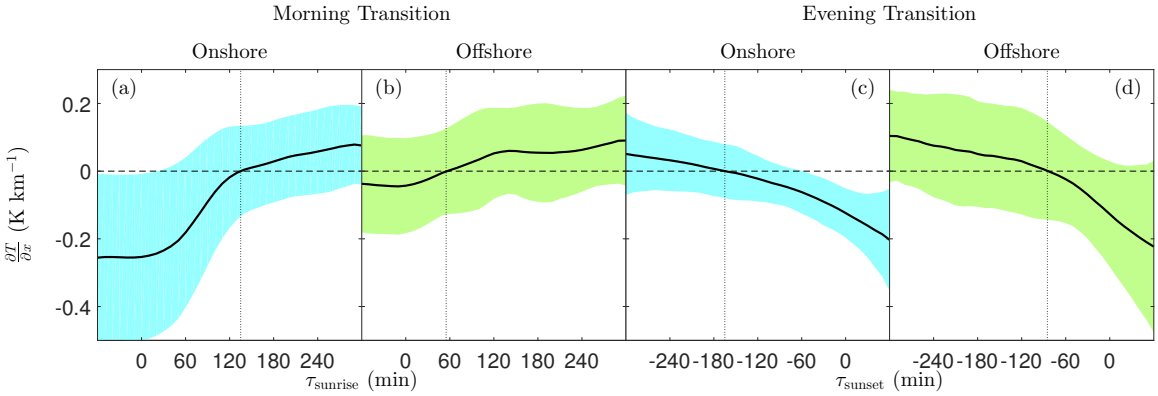

Figure 4.13: Composite time series of the inland temperature gradient computed at the 10-m levels at Beach and Substation using simple differencing. Positive (negative) gradients indicate that the air temperature increases (decreases) with inland distance. The shading indicates the time series ± 1 standard deviation.

and Mahrt (2003), where the multiresolution spectra are interpreted in terms of a simple, unweighted moving averages, rather than the Haar transform (Howell and Mahrt, 1997) or wavelets (Katul and Parlange, 1995). MRFD works by splitting the time series into simple averages over different scales. First, the average over the entire record is calculated and subsequently subtracted. The average departure from the mean is then recorded. Next, the averaging period is broken into two sub-periods, over which the respective means are computed and subsequently removed. The sub-periods are divided again and the process is repeated until there is only one sample per averaging period (see Vickers and Mahrt (2003) Fig. 1). With each step, the data are high-pass filtered with the filter width becoming progressively more narrow. The departures from each period are then used to compute the spectra and cospectra with Eq. 2 and 3 in Vickers and Mahrt (2003).

Figures 4.14 and 4.15 give composite contour plots of the sensible heat and momentum flux MRFD cospectra through the MT and ET at Beach and Substation for both flow regimes. The spectra and cospectra are calculated using 2^{16} data points, which equates to $\approx$ 55 min of data recorded at 20 Hz. Note that much of the experiment was recorded at 10 Hz and subsequently interpolated to 20 Hz to yield a uniform dataset. Thus, little to no information is available beyond the effective Nyquist frequency of 5 Hz ($10^{-0.7}$ s). To improve temporal resolution, the MRFD spectra and cospectra advance forward in time in increments of $2^{16}/2$ data points, or $\approx$ 27 min. The spectra and cospectra fluctuation time scales are indicated along the ordinate; the time relative to sunrise or sunset is indicated along the abscissa and the shading indicates the magnitude of the fluctuations associated with the given fluctuation scale and temporal location. In Fig. 4.16 and 4.17, selected small, peak and large time scales of the sensible heat and momentum flux are given as time series. The location of the scales within the cospectra are indicated in Fig. 4.14 and 4.15. The peak scale is taken as time scale associated with the largest flux, the small and large time scales are taken as the point where the energy content has dropped to 50 % of the peak value. The time series are normalized by their maximum value to allow for an easy comparison of turbulence development and decay between time scales.

Beginning with the cospectra of the sensible heat flux given in Fig. 4.14 and 4.16,

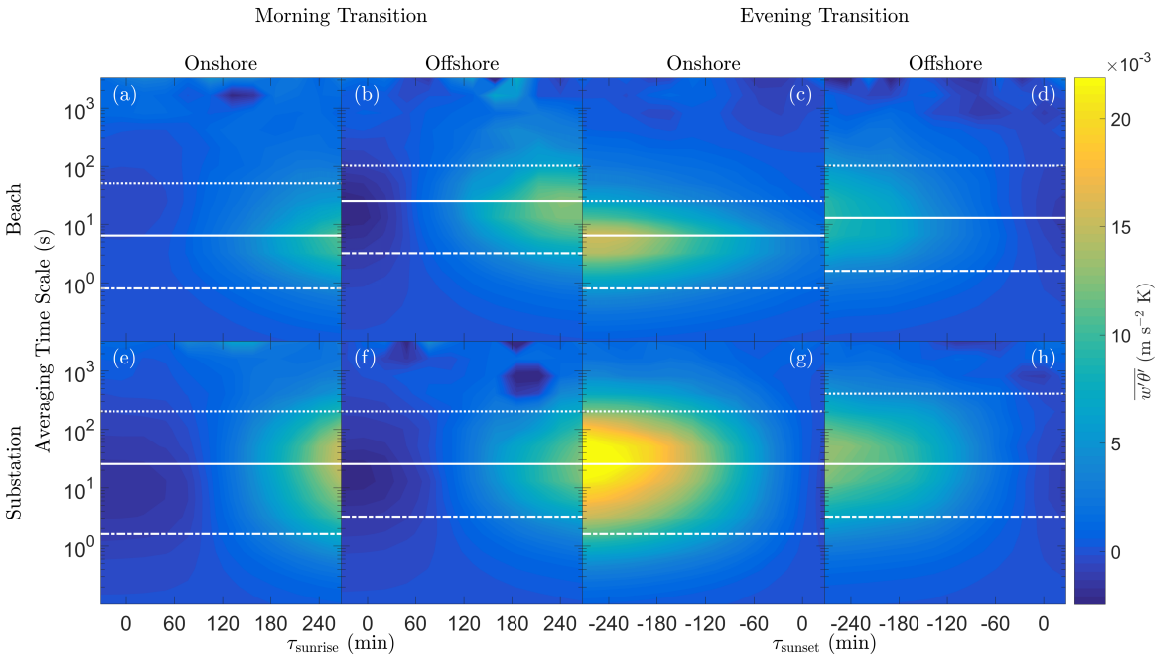

Figure 4.14: MRFD cospectra of the kinematic sensible heat flux at Beach and Substation for the onshore and offshore flow regimes through the MT and ET. The horizontal white lines indicate the large (top line), peak (middle line) and small (bottom line) time scale fluctuations that are shown as time series in Fig. 4.16.

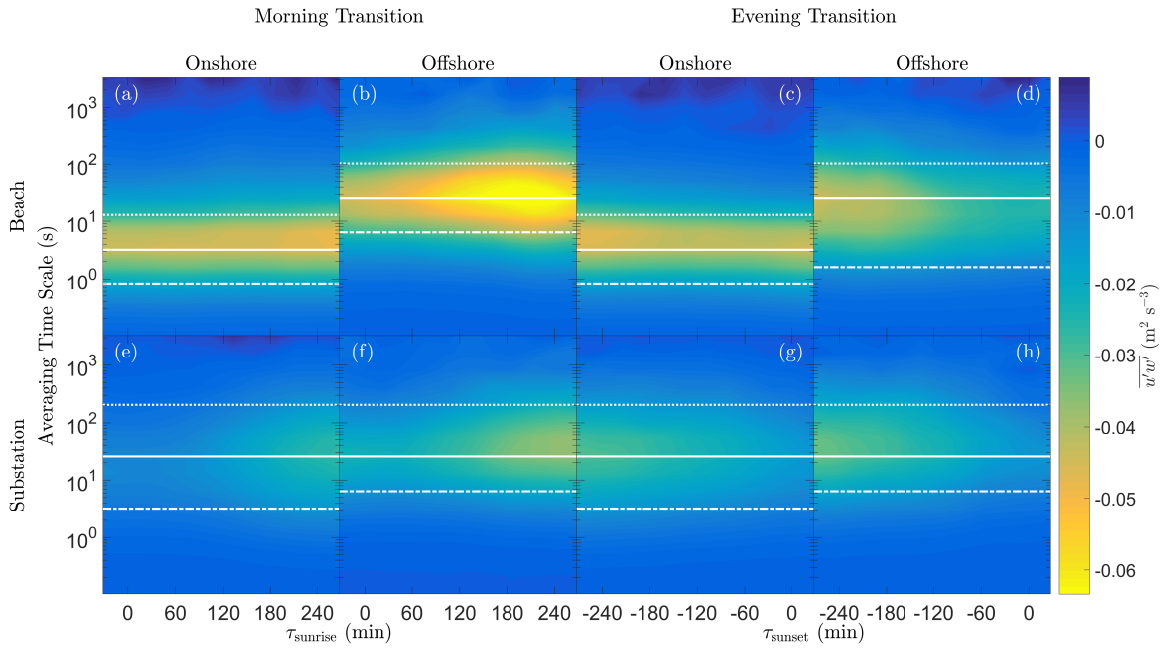

Figure 4.15: Same as Fig. 4.14 but for momentum flux.

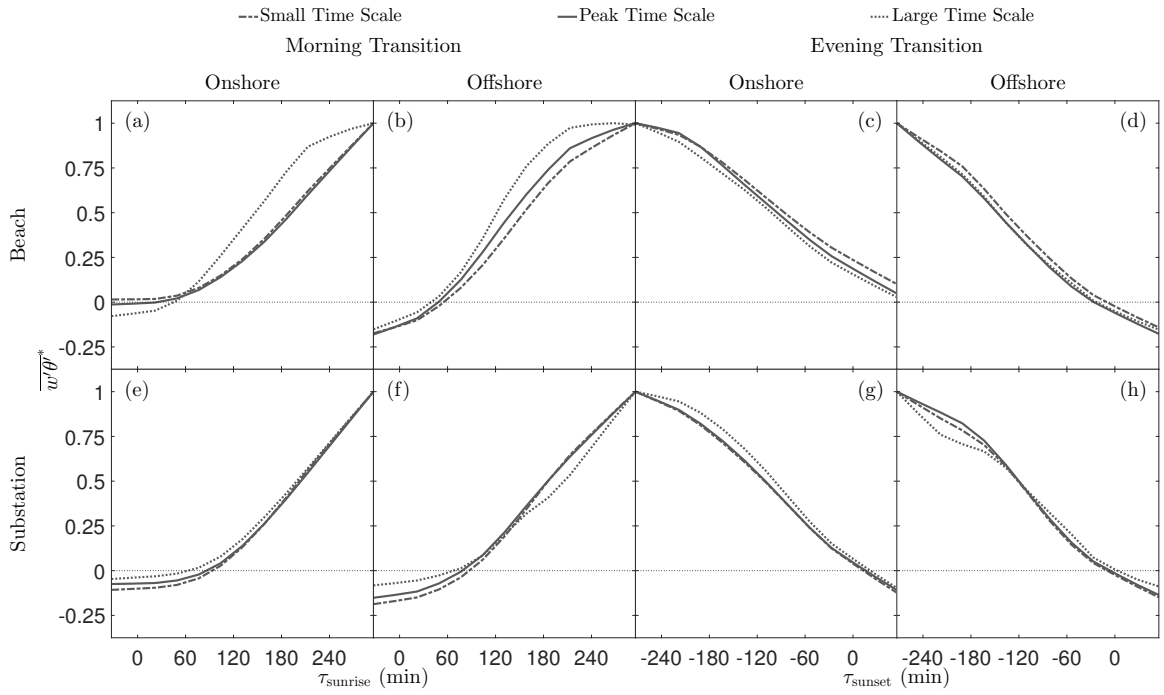

Figure 4.16: Composite time series of the large, peak and small time scales of the MRFD sensible heat flux cospectra (Fig. 4.14). Each time series has been normalized by its maximum value.

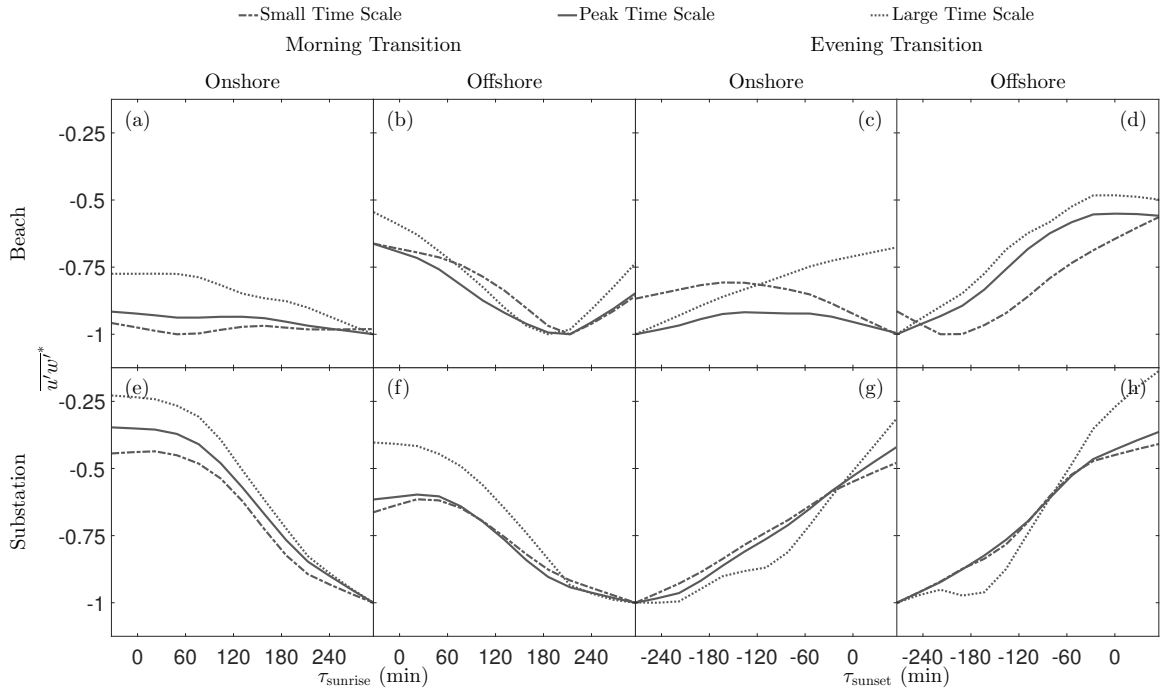

Figure 4.17: Same as Fig. 4.16 but for momentum flux.

we observe a shift in the peak time scales between the onshore and offshore regimes at the Beach site. The peak scale for onshore flow at the Beach occurs at $\approx$ 7 sec and for offshore flow occurs around 12 sec. At the Substation site, the peak scale is constant through the MT and ET for both flow regimes and is $\approx$ 12 sec. The smaller peak time scale for the onshore Beach flow is likely due to the footprint over which the flux is generated. The low surface roughness and shallow mixed layer typical over oceans (Garratt, 1994) is likely responsible for the smaller peak time scale. Once the inland flow has reached the substation site, the reduced peak time scale is no longer evident, indicating that the near-surface atmosphere has come into equilibrium with the land surface.

In general, the offshore regime shows relatively large negative heat fluxes at the beginning of the MT and end of the ET at both sites, for all but the largest scales. Through the MT, the negative heat flux becomes less negative at larger scales and appears to precede that at smaller scales. For scales $\gtrsim 10^{2.5}$ s, contributions to both the negative and positive sensible heat fluxes are minimal for both sites, transitions and regimes, indicating the beginning of the cospectral gap. As discussed in Vickers and Mahrt (2003), identification of the gap is important for appropriate determination of flux averaging times. Scales smaller than the gap are associated with local turbulence and expected to follow similarity theory relationships. Scales greater than the gap are associated with nonstationarity and meso- or synoptic scale motions that do not adhere to similarity theory.

Normalized, representative large, peak and small time scale fluctuations of the sensible heat flux are given in Fig. 4.16. The larger sensible heat flux that occurs during the onshore flow regime is evident at all scales. During the MT, for the offshore Beach regime and both Substation regimes, the crossover of the sensible heat flux occurs at all scales over a period of $\approx$ 30 min. The large scale crosses zero first, followed by the peak and then small scales. Through the ET, the crossover occurs nearly simultaneously at all scales. Finally, as expected, the decay rate of sensible heat flux is observed to be largest at the peak energy scale and smaller at the large and small scales, though the trends are similar. The heat flux begins to slowly decay in the early afternoon, reaches a quasi-linear phase in the late afternoon and then the

decay rate decreases into the evening. We suggest that the trend at all scales could be fit accurately with the complementary error function as described in Nadeau et al. (2011).

Next, the cospectra of the momentum flux are considered (Fig. 4.15). Again, the scale disparity at Beach between onshore and offshore flow is observed. Surprisingly, the largest downward flux of momentum occurs during offshore flow at the Beach site, indicating that the mangrove upstream of the Beach tower effectively transports momentum into the canopy. Though not as pronounced, larger momentum fluxes are also observed for the offshore flow regime at Substation, indicating higher roughness for the Substation offshore fetch as well. Though not shown, this behaviour is clearly evident from the increased velocity gradient observed in the velocity profiles for offshore flow.

For the Beach onshore regime, little diurnal influence is observed, indicating that shear production of turbulence is dominant. This is likely a result of shear induced by the wind break as well as small sensible heat fluxes for the Beach onshore regime. For the other cases, as expected, larger fluctuations over a wider range of scales are observed during daylight hours. As was done for the sensible heat flux cospectra, time series of representative large, peak and small time scales are shown in Fig. 4.15. For the Beach onshore case through the MT and ET, the small and peak scale fluctuations are quasi-constant through the diurnal cycle. Interestingly, for the ET, the peak and small scales increase late in the evening while the large time scale decays. As shown in Fig. 4.8, the increase in momentum flux at the peak and small scales roughly coincides with the increase in observed wind speed. Meanwhile, the decay in the large scale momentum flux shows approximate agreement with the reduction of the sensible heat flux. This leads us to speculate that the mechanical production of turbulence is associated with smaller scales than the buoyant contribution for the onshore flow regime. In the offshore Beach ET case and all Substation cases, the development (MT) and decay (ET) of the momentum flux could be well represented with the complementary error function. For the offshore Beach regime through the MT, the maximum in downward momentum transport occurs very early in the day at $\approx$ 200 min after sunrise.

4.3.4 TKE Budget

In order to understand the mechanisms contributing to the production and decay of turbulence through the MT and ET, the budget of TKE is considered. Due to instrumentation constraints, we must consider the simplified budget of TKE, which assumes horizontal homogeneity and no advection; the simplified budget is given by:

$$\underbrace{\frac{\partial \overline{e}}{\partial t}}_{\text{I}} = \underbrace{-\overline{u'w'}\frac{\partial \overline{u}}{\partial z}}_{\text{II}} + \underbrace{\frac{g}{\overline{\theta}}\overline{w'\theta'_v}}_{\text{III}} \underbrace{-\frac{\partial \overline{w'e'}}{\partial z}}_{\text{IV}} \underbrace{-\frac{\partial \overline{w'P'/\rho_0}}{\partial z}}_{\text{V}} - \underbrace{\epsilon}_{\text{VI}}, \tag{4.3}$$

where P is pressure and ρ_0 is the ambient air density. Term I is the storage or tendency of TKE, II is shear production of TKE, III is buoyancy production of TKE, IV and V are turbulent and pressure transport of TKE, respectively and ϵ is the dissipation of TKE, which always a sink.

Figure 4.18 gives the composite budgets of TKE at Beach and Substation for the MT, ET and both flow regimes. Term I was computed directly from the sonic anemometers; term II was computed from the sonic anemometer with the velocity gradient computed using forward differencing between the #40 cup anemometers at 10 and 20 m; term III was computed from the sonic anemometers and HMP155 T/RH probe; following Nilsson et al. (2016a) and due to insufficient instrumentation, Terms IV and V were computed as residuals and lumped together as a collective transport term, which includes the influence of terms IV and V along with all remaining residual influences including advection, subsidence and instrument uncertainty.

The dissipation was estimated spectrally, following Nilsson et al. (2016a) as

$$\epsilon = \frac{2\pi n}{\overline{u}}\left[\frac{3nS_w(n)}{4\alpha}\right]^{3/2} \tag{4.4}$$

where S_w is the power spectra of the vertical velocity, n is frequency in Hz and $\alpha \approx 0.52$ is the Kolmogorov constant. Eq. 4.4 was estimated by computing a linear fit of the premultiplied spectra over the inertial subrange in loglog space, where the slope is expected to $\approx -2/3$ (Kolmogorov, 1968). The fit was forced to have a slope of $-2/3$ and then used with Eq. 4.4 to estimate the dissipation over 10 min intervals.

As expected from previous work (e.g. Nilsson et al., 2016a), in all cases, the TKE tendency is observed to be insignificant relative to the other terms. At the Beach site,

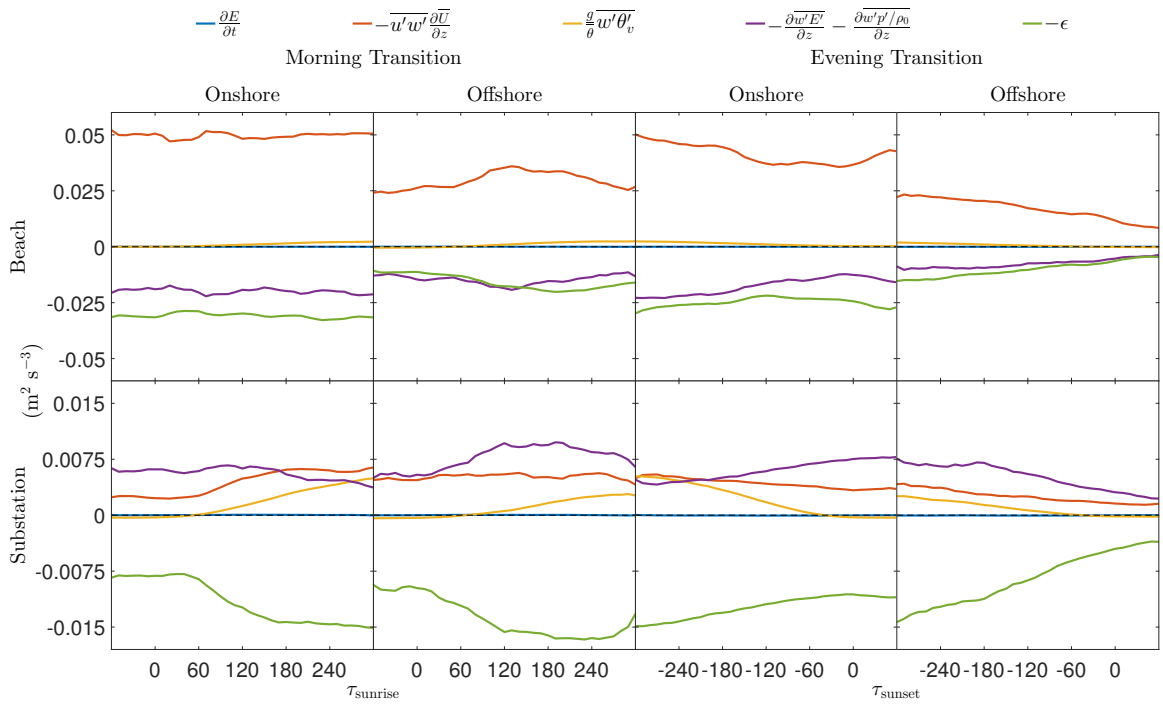

Figure 4.18: Composite time series of the TKE budget terms (Eq. 4.3). Note that the ordinate scale differs between sites. Terms IV and V are lumped together and estimated as the residual of the budget. Terms are plotted such that values above (below) zero are a source (sink) of TKE.

the magnitude of the shear production and dissipation is observed to be much larger than those values observed at Substation, for both flow regimes and transitions (note the differing ordinate scales). Given that the velocity gradient is computed between the 10 and 20-m levels, it is likely that the shear production for the Beach onshore case is overestimated due to the presence of the wind break disproportionately decelerating the 10-m wind speed. Regardless, we speculate with confidence that shear production is the dominant mechanism for turbulence generation in the Beach onshore case.

At the Beach, only the offshore ET case shows the expected decay in mechanical production. As discussed previously, for the onshore ET case, shear production actually increases later into the evening as the wind speed increases. The evening increase in shear production is sufficient to increase the level of TKE through the evening transition (Fig. 4.12). Finally, the turbulent transport, which is computed as a residual, is estimated to be a sink of TKE.

Due to relatively small sensible heat fluxes and the upstream wind break, it was expected that shear production of TKE would be the dominant production term at Beach for the onshore regime, but it is surprising that shear production is also dominant for the offshore regime. This is likely in part due to the large roughness of the mangrove and potential uncertainties in the vertical velocity gradient as a result of the heterogeneous terrain. For example, recirculations may develop on the leeward side of the mangrove forest, ≈ 50 m upstream from the Substation tower. Presumably, the 20-m wind speed is less influenced by such circulations.

At Substation, the production of TKE is much more balanced between buoyant and shear production. Shear production shows some diurnal influence as wind increases through the MT and decreases through the ET. The buoyant production is near-zero or slightly consumptive in the early morning and late evening and becomes nearly equal to shear production late in the MT and early in the ET. Unlike the Beach, the transport terms are estimated to act as a net source of TKE at all times.

4.4 Conclusions

An improved understanding of near-surface atmosphere dynamics through the MT and ET is critical both fundamentally and pragmatically. Here, we have used a 30-month dataset collected over heterogeneous terrain in Belize to study the morning and evening transitions. Unlike most studies, we have made extensive use of composite time series with several hundred days of data to allow for a climatological examination of the ET and MT. The main conclusions are:

- There are two predominant wind regimes over Belize (Fig. 4.5 and 4.6): one directed easterly onshore that typically occurs during the wet season and another directed northwesterly offshore that typically occurs during the dry season. The mean and turbulence characteristics vary dramatically between the two regimes.

- The mean winds speeds are much higher for the onshore regime. The Beach tower observes near-constant wind speeds during the onshore flow regime (Fig. 4.8 and 4.9). The inland wind deficit is approximately 5 % km^{-1} during the onshore flow regime with the inland towers observing a higher winds and less wind direction scatter during daylight hours. We hypothesize that this is due to the superposition of the synoptic easterlies and thermally driven sea-breeze.

- Countergradient heat fluxes are observed to occur for both flow regimes (Fig. 4.10), and both the MT and ET and at both the Beach and Substation sites. During the MT, the sensible heat flux crossover typically precedes the temperature gradient crossover by approximately an hour. For the ET, the temperature gradient crossover precedes the heat flux crossover by approximately an hour, meaning that the duration of the unstable temperature gradient is $\approx$ 2 hour less than the duration of the upward (away from the surface) sensible heat flux. The countergradient fluxes occur when the distance over which the temperature gradient is estimated is inconsistent with the scales of turbulence that are predominantly driving the flow.

- For onshore conditions at the Beach site, conditions are nearly always unstable ($\zeta < 0$) and the sensible heat flux is nearly always positive (directed away

from the surface) with only a very brief period in the early morning where the composite heat flux is very weakly negative (Fig. 4.10 and 4.11). The behaviour is due to the warm Carribean Sea that is able to persistently produce positive heat fluxes throughout the diurnal cycle.

- Multiple decay rates of TKE are observed (Fig. 4.12), including the rare case where TKE strengthens through the ET that was observed during onshore conditions at the Beach site. The behaviour is due to the mechanical production of turbulence that is dominant over buoyant production for the Beach onshore regime. The disparity is due to the relatively weak heat fluxes during onshore flow as well as the near-shore wind break that works to generate a large amount of turbulence.

- Multiresolution flux decomposition (MRFD) was used to study the spatial and temporal scale of turbulence (Fig. 4.14 – 4.17). MRFD revealed a scale disparity between the onshore and offshore regimes at the Beach site. In general, the onshore flow was associated with smaller time scales. The Beach onshore regime showed little influence from the diurnal cycle, indicating that for onshore flow, coastal turbulence is driven predominantly by shear production. The largest momentum fluxes were observed for the offshore flow regime, in spite of the insolation and sensible heat flux being weaker for the offshore flow regime. The increased momentum flux is due to a larger velocity gradient due to the larger roughness elements in the offshore, upstream fetch. Finally through the MT, turbulence was observed to increase first at short time scales and gradually move to larger time scales as the depth of the near-surface mixed layer increased through the MT.

- The TKE budgets were evaluated in Fig. 4.18. The results confirm that shear production is the dominant production term at Beach with buoyant production contributing very little. Further inland, the budget is much more balanced. Both the shear and buoyant production show a diurnal cycle. The buoyant production increases and decreases in consonance with the sensible heat

flux, while the mechanical production decreases during the calm periods that typically occur during the MT and ET.

4.5 References

Acevedo, O. C. and D. R. Fitzjarrald, 2001: The early evening surface-layer transition: Temporal and spatial variability. *J. Atmos. Sci.*, **58**, 2650–2667.

Angevine, W. M., 2008: Transitional, entraining, cloudy, and coastal boundary layers. *Acta Geophys.*, **56**, 2–20.

Angevine, W. M., H. K. Baltink, and F. C. Bosveld, 2001: Observations of the morning transition of the convective boundary layer. *Boundary-Layer Meteorol.*, **101**, 244–253.

Bange, J., T. Spieß, and A. van den Kroonenberg, 2007: Characteristics of the early-morning shallow convective boundary layer from helipod flights during stinho-2. *Theoretical and Applied Climatology*, **90**, 113–126.

Basu, S., J.-F. Vinuesa, A. Swift, S. Basu, J.-F. Vinuesa, and A. Swift, 2008: Dynamic LES modeling of a diurnal cycle. *Journal of Applied Meteorology and Climatology*, **47**, 1156–1174.

Beare, R. J., 2008: The role of shear in the morning transition boundary layer. *Boundary-Layer Meteorology*, **129**, 395–410.

Blay-Carreras, E., E. R. Pardyjak, D. Pino, D. C. Alexander, F. Lohou, and M. Lothon, 2014: Countergradient heat flux observations during the evening transition period. *Atmos. Chem. Phys.*, **14**, 9077–9085.

Brazel, A., H. Fernando, J. Hunt, N. Selover, B. Nedquist, and E. Parkyjak, 2005: Evening transition observations in Phoenix, Arizona, USA. *J. Appl. Meteorol.*, **44**, 99–112.

Cuxart, J., B. Wrenger, J. Reuder, M. O. Jonassen, M. A. Jiménez, and M. Lothon, 2016: Estimation of the advection effects induced by surface heterogeneities in the surface energy budget. *Atmos. Chem. Phys. Discuss.*, 1–18.

Fernando, H., et al., 2015: The materhorn: Unraveling the intricacies of mountain weather. *Bulletin of the American Meteorological Society*, **96 (11)**, 1945–1967.

Garratt, J. R., 1990: The internal boundary layer - A review. *Boundary-Layer Meteorol.*, **50**, 171–203.

Garratt, J. R., 1994: Review: the atmospheric boundary layer. *Earth-Science Reviews*, **37**, 89–134.

Goulart, A. G., B. E. J. Bodmann, M. T. M. B. de Vilhena, P. M. M. Soares, and D. M. Moreira, 2010: On the time evolution of the turbulent kinetic knergy spectrum for decaying turbulence in the convective boundary layer. *Boundary-Layer Meteorol.*, **138**, 61–75.

Graf, A., A. van de Boer, A. Moene, and H. Vereecken, 2014: Intercomparison of methods for the simultaneous estimation of zero-plane displacement and aerodynamic roughness length from single-level eddy-covariance data. *Boundary-Layer Meteorol.*, **151**, 373–387.

Grant, A. L. M., 1997: An observational study of the evening transition boundary-layer. *Q. J. R. Meteorol. Soc.*, **123**, 657–677.

Holtslag, A. A. M., et al., 2013: Stable atmospheric boundary layers and diurnal cycles: Challenges for weather and climate models. *Bull. Am. Meteorol. Soc.*, **94**, 1691–1706.

Howell, J. and L. Mahrt, 1997: Multiresolution flux decomposition. *Boundary-Layer Meteorol.*, **83**, 117–137.

Hsieh, C. I., G. Katul, and T. W. Chi, 2000: An approximate analytical model for footprint estimation of scalar fluxes in thermally stratified atmospheric flows. *Adv. Water Resour.*, **23 (7)**, 765–772.

Jensen, D. D., D. F. Nadeau, S. W. Hoch, and E. R. Pardyjak, 2016: Observations of near-surface heat-flux and temperature profiles through the early evening transition over contrasting surfaces. *Boundary-Layer Meteorol.*, **159**, 567–587.

Katul, G. G. and M. B. Parlange, 1995: The spatial structure of turbulence at production wavenumbers using orthonormal wavelets. *Boundary-Layer Meteorol.*, **75 (1-2)**, 81–108.

Kolmogorov, A., 1968: Local structure of turbulence in an incompressible viscous fluid at very high Reynolds numbers. *Physics-Uspekhi*, **10**, 734–746.

Kumar, V., J. Kleissl, C. Meneveau, and M. B. Parlange, 2006: Large-eddy simulation of a diurnal cycle of the atmospheric boundary layer: Atmospheric stability and scaling issues. *Water Resour. Res.*, **42**, 1–18.

Lampert, A., et al., 2016: A study of local turbulence and anisotropy during the afternoon and evening transition with an unmanned aerial system and mesoscale simulation. *Atmos. Chem. Phys*, **16 (12)**, 8009–8021.

Lapworth, A., 2006: The morning transition of the nocturnal boundary layer. *Boundary-Layer Meteorology*, **119**, 501–526.

Lenschow, D. H., B. B. Stankov, and L. Mahrt, 1979: The Rapid Morning Boundary-Layer Transition. *Journal of the Atmospheric Sciences*, **36 (11)**, 2108–2124.

Lothon, M., et al., 2014: The BLLAST field experiment: Boundary-Layer Late Afternoon and Sunset Turbulence. *Atmos. Chem. Phys.*, **14**, 10 931–10 960.

Manoj, M., P. Devara, and S. Taraphdar, 2013: Lidar investigation of tropical nocturnal boundary layer aerosols and cloud macrophysics. *Atmos. Res.*, **132**, 65–75.

Nadeau, D. F., E. R. Pardyjak, C. W. Higgins, H. J. S. Fernando, and M. B. Parlange, 2011: A simple model for the afternoon and early evening decay of convective turbulence over different land surfaces. *Boundary-Layer Meteorol.*, **141**, 301–324.

National Meteorological Service of Belize, 2016: Climate Summary. URL `http://www.hydromet.gov.bz/climate-summary`, URL `http://www.hydromet.gov.bz/climate-summary`.

Nieuwstadt, F. T. M. and R. A. Brost, 1986: The decay of convective turbulence. *J. Atmos. Sci.*, **43**, 532–546.

Nilsson, E., F. Lohou, M. Lothon, E. Pardyjak, L. Mahrt, and C. Darbieu, 2016a: Turbulence kinetic energy budget during the afternoon transition Part 1: Observed surface TKE budget and boundary layer description for 10 intensive observation period days. *Atmos. Chem. Phys.*, **16**, 8849–8872.

Nilsson, E., M. Lothon, F. Lohou, E. Pardyjak, O. Hartogensis, and C. Darbieu, 2016b: Turbulence Kinetic Energy budget during the afternoon transition – Part 2: A simple TKE model. *Atmos. Chem. Phys. Discuss.*, **15**, 29 807–29 869.

Parameswaran, K., K. Rajeev, and K. S. Gupta, 1997: An observational study of night time aerosol concentrations in the lower atmosphere at a tropical coastal station. *Journal of Atmospheric and Solar-Terrestrial Physics*, **59**, 1727–1737.

Pino, D., H. J. J. Jonker, J. V.-G. D. Arellano, and A. Dosio, 2006: Role of shear and the inversion strength during sunset turbulence over land: Characteristic length scales. *Boundary-Layer Meteorol.*, **121**, 537–556.

Rizza, U., M. Miglietta, G. Degrazia, O. Acevedo, and E. Marques Filho, 2013: Sunset decay of the convective turbulence with Large-Eddy Simulation under realistic conditions. *Physica A*, **392**, 4481–4490.

Robinson, S. M., 1962: Computing wind profile parameters. *J. Atmos. Sci.*, **19**, 189–190.

Sáenz, F. and A. M. Durán-Quesada, 2015: A climatology of low level wind regimes over Central America using a weather type classification approach. *Frontiers in Earth Science*, **3**, 1–18.

Sorbjan, Z., 1997: Decay of convective turbulence revisited. *Boundary-Layer Meteorol.*, **82**, 503–517.

Sorbjan, Z., 2007: A numerical study of daily transitions in the convective boundary layer. *Boundary-Layer Meteorology*, **123**, 365–383.

Steeneveld, G.-J., 2014: Current challenges in understanding and forecasting stable boundary layers over land and ice. *Frontiers in Environmental Science*, **2**, 41.

Stull, R., 1988: *An Introduction to Boundary Layer Meteorology*. Springer Science, 666 pp.

Svensson, G., et al., 2011: Evaluation of the diurnal cycle in the atmospheric boundary layer over land as represented by a variety of single-column models: The second GABLS experiment. *Boundary-Layer Meteorology*, **140**, 177–206.

Vickers, D. and L. Mahrt, 2003: The cospectral gap and turbulent flux calculations. *J. Atmos. Ocean. Technol.*, **20**, 660–672.

Wang, D., J. C. McWilliams, W. G. Large, D. Wang, J. C. McWilliams, and W. G. Large, 1998: Large-eddy simulation of the diurnal cycle of deep equatorial turbulence. *Journal of Physical Oceanography*, **28**, 129–148.

Zhang, D.-L., W.-Z. Zheng, D.-L. Zhang, and W.-Z. Zheng, 2004: Diurnal Cycles of Surface Winds and Temperatures as Simulated by Five Boundary Layer Parameterizations. *Journal of Applied Meteorology*, **43**, 157–169.

CHAPTER 5

CONCLUSIONS AND FUTURE WORK

The focus of this dissertation was to study transitory turbulence in the atmospheric boundary layer, using observational data. The objective was to identify periods and locations where parameterizations utilized in most weather and climate models are expected to perform poorly. The data were then analyzed to gain a greater understanding of transitory turbulence under such conditions. The findings contribute to our fundamental understanding of atmospheric turbulence, may be used as simplistic models, and also lay the ground work for more accurate numerical simulations of the morning and evening transitions over complex terrain.

In Ch. 2, near-surface countergradient heat fluxes that occur through the evening transition were studied. The countergradient fluxes were observed to be both site and height dependent and occurred when the crossover of the sensible heat flux preceded the crossover of the local temperature gradient and vice versa. The crossover of the sensible heat flux was found to show height independence over the 20-m turbulence towers, but showed site dependence between the two experimental sites considered. Conversely, the temperature gradient reversal was observed to show strong height dependence, occurring earlier in the ET at higher tower levels, but had very similar behaviour at both sites. The budgets of potential temperature and sensible heat flux were examined to gain insight into the phenomenon. It was determined that the difference in countergradient behaviour between the two sites was largely due to the differing surface and subsurface characteristics at the two sites. Finally, the ratio of the gradient to buoyant production terms in the sensible heat flux tendency equation, evaluated in the early afternoon, was shown to correlate with the type and duration of the countergradient flux.

Ch. 3 examined the onset and evolution of katabatic flow over an arid, shallow slope through the evening transition. Mean time scales describing the evolution of the katabatic flow were defined. First, just after sunset, the inertialy driven anabatic flow is arrested by friction. Next, there is a calm period with light wind, during which the near surface air mass is stabilizing. Once sufficiently stable, bouyancy begins to drive a downslope flow. The velocity and depth of the flow increases until approximately 120 min after sunset, at which point approximate equilibrium is achieved. The magnitude of these time scales showed a large degree of interdiurnal variability. A simple mechanistic model was developed and shown to capture an appreciable degree of the variability. Finally, using statistical analysis, the valley wind system, shadow front speed and soil moisture were found to be the variables most strongly correlated the interdiurnal variance of the katabatic flow. Using these variables as inputs, a multivariate partial-least squares model was developed and shown to strongly correlate with the observed interdiurnal variation in the katabatic flow.

Finally, in Ch. 4, the morning and evening transitions were studied over a coastal, tropical shrimp farm in Belize, Central America. The dataset, spanning more than two years, was collected as part of a wind resource assessment. Three tall masts, forming an inland transect from the coast to approximately 4 km inland, were used to study the morning and evening transitions. The study utilized the long dataset to generate composite time series of the mean and turbulence variables to gain a climatological understanding of the morning and evening transition periods. It was observed that the wind direction varies seasonally and can be divided into onshore and offshore wind regimes. For the onshore regime, at the mast on the coast, the diurnal cycle was shown to play a minor role through the morning and evening transitions. Mechanical generation of turbulence was found to be the dominant source of turbulence generation and was able to maintain high levels of turbulence through the entire evening transition. For the inland mast, both mechanical and bouyant production of turbulence were found to be significant. Finally, multiresolution flux decomposition was used to study the scale dependence of the turbulence evolution through the morning and evening periods. In the morning, it was observed that the

small-scale turbulence increases prior to the larger scales. This is consistent with the gradual onset of the convective boundary layer that builds from the surface and slowly erodes the overlying stable layer.

The studies presented in Ch. 2–4 make a meaningful contribution to the literature of both the morning and evening transition and flow over complex terrain. The findings add to our fundamental understanding of transitory turbulence in the atmospheric boundary layer and are also of pragmatic importance. The results, such as the countergradient (Ch. 2) and katabatic models (Ch. 3), may be used as stand alone tools, when it is not feasible to run a full simulation, and also in conjunction with numerical simulations. Many of the phenomenon observed in the studies are either not resolved or incorrectly described by most numerical simulations. Going forward, the observational work presented here should be used to improve the performance of numerical tools. The results of the countergradient heat flux study provide a strong foundation for improving similarity relationships through the evening transition. The katabatic flow study should be used to validate LES simulations of katabatic flow. The results of the study may be used to diagnose where simulations under perform. Finally, the study of the morning and evening transition may also be used as validation for simulations that couple the synoptic and microscales over complex terrain.

APPENDIX

SELECTING A FLUX AVERAGING TIME

Many field experiments conducted today employ instrumentation capable of directly observing fluxes of temperature, momentum, moisture and other trace gasses such as carbon dioxide or methane. Such observations are crucial for model evaluation and development. However, selecting the proper period over which to average the turbulent fluctuations is not straightforward. As an example, the vertical flux of temperature ($\overline{w'T'}$) may be estimated with fast-response, sonic-anemometry observations (typically 10 or 20 Hz) of w and T. In order to estimate the flux, w and T must be decomposed into their mean ($\overline{w}$, $\overline{T}$) and turbulent quantities (e.g. $w' = w - \overline{w}$, $T' = T - \overline{T}$). The turbulent fluctuations are then multiplied together and averaged over a given period of time (or space, in the case of aircraft observations), to compute the covariance, which is equal to the vertical, kinematic flux of temperature.

The magnitude of the flux shows sensitivity to both the period over which the signals are decomposed and the period over which they are subsequently averaged. If the selected period is insufficient, the magnitude of the flux is underestimated as a result of effectively high-pass filtering the signal and thus omitting low-frequency contributions to the flux. However, if the selected averaging period is too long, non-turbulent scales associated with the evolving background state and nonstationarity are included in the flux, leading to an overestimation (Lee et al., 2006).

Traditionally, researchers have selected 30-min periods for both the decomposition and covariance calculation (Aubinet et al., 2012). However, this has been shown to not always be sufficient to capture all of the flux (Sakai et al., 2001; Finnigan et al., 2003). A more quantitative method for determining the proper averaging period is the *ogive* test (Berger et al., 2001; Aubinet et al., 2012). The *ogive* test works by cumulatively

integrating the cospectra of w and T, starting with the highest frequencies. The cumulative integral of the cospectra is given by

$$OG(f_0) = \int_{f_{\text{high}}}^{f_0} C(f)\mathrm{d}f, \tag{A.1}$$

where f_{high} is the Nyquist frequency, $C(f)$ is the cospectra at frequency f and $OG(f_0)$ is the integral of the cospectra between the Nyquist frequency and f_0. The frequency at which $OG_{ws}(f_0)$ converges to an approximately constant value gives the appropriate time period for the flux calculation.

Sun et al. (2006) compared the results of the *ogive* test with the "ensemble block-averaging" method. The ensemble block averaging method works by computing the flux with a range of averaging periods and examining the resultant fluxes as a function of averaging time, in order to identify their asymptotic behaviour, indicating the time period at which the flux has converged (e.g. Sakai et al., 2001; Finnigan et al., 2003). Using data from several ChinaFLUX sites, Sun et al. (2006) observed little difference between the two methods and found that 30 min is typically sufficient to adequately resolve the flux of carbon dioxide.

Similarly, Foken et al. (2006) observed that 30 min averaging periods are typically sufficient for the *ogive* functions to converge, with the exclusion of nonstationary conditions, such as the morning or evening. In such transitory cases, the *ogive* tests never showed a clear convergence. This occurs when the so-called cospectral gap (Stull, 1988) between the micro and meso scales is not well defined. In such cases, the appropriate averaging period is selected on the specific aims of the study, with the understanding that the fluxes may not be fully converged or may be contaminated by the non-stationary conditions.

A.1 References

Aubinet, M., T. Vesala, and D. Papale, 2012: *Eddy Covariance - A Practical Guide to Measurement and Data Analysis — Springer*. Springer Netherlands, 438 pp.

Berger, B. W., et al., 2001: Long-Term Carbon Dioxide Fluxes from a Very Tall Tower in a Northern Forest: Flux Measurement Methodology. *J. Atmos. Ocean. Technol.*, **18**, 529–542.

Finnigan, J. J., R. Clement, Y. Malhi, R. Leuning, and H. a. Cleugh, 2003: Re-evaluation of long-term flux measurement techniques. Part I: Averaging and coordinate rotation. *Boundary-Layer Meteorol.*, **107**, 1–48.

Foken, T., F. Wimmer, M. Mauder, C. Thomas, and C. Liebethal, 2006: Some aspects of the energy balance closure problem. *Atmospheric Chemistry and Physics*, **6 (12)**, 4395–4402.

Lee, X., W. Massman, and B. Law, 2006: *Handbook of Micrometeorology: A Guide for Surface Flux Measurement and Analysis*, Vol. 29. Springer Science & Business Media.

Sakai, R. K., D. R. Fitzjarrald, K. E. Moore, R. K. Sakai, D. R. Fitzjarrald, and K. E. Moore, 2001: Importance of Low-Frequency Contributions to Eddy Fluxes Observed over Rough Surfaces. *J. Appl. Meteorol.*, **40**, 2178–2192.

Stull, R., 1988: *An Introduction to Boundary Layer Meteorology*. Springer Science, 666 pp.

Sun, X.-M., Z.-L. Zhu, X.-F. Wen, G.-F. Yuan, and G.-R. Yu, 2006: The impact of averaging period on eddy fluxes observed at ChinaFLUX sites. *Agric. For. Meteorol.*, **137**, 188–193.